Crystal nucleation efficacy of flow-induced formed nuclei and carbon nanotubes in the engineering polymer polyamide 66

Dissertation

Zur Erlangung des
Doktorgrades der Ingenieurwissenschaften (Dr.-Ing.)

der

Naturwissenschaftlichen Fakultät II
- Chemie, Physik und Mathematik

der Martin-Luther-Universität
Halle-Wittenberg,

vorgelegt

von Frau Anne M. Gohn
geb. am 3. October 1991 in Sewickley, Pennsylvania, USA

Public defense:
22 June 2022 at 3 p.m.
Hörsaal 1.04, Von-Seckendorff-Platz 1, 06120 Halle

Doctoral Advisor:
Professor Dr. René Androsch

Doctoral Dissertation Review Committee:
Professor Dr. R. Androsch
Professor Dr. A. Rhoades
Professor Dr. R. Pantani

Doctoral Defense Committee:
Professor Dr. T. Hahn (Chair)
Professor Dr. M. Beiner
Professor Dr. M. Bartke
Professor Dr. J. Kreßler
Professor Dr. J. Ulrich

Abstract

A foundational knowledge of flow-induced crystallization, especially at process-relevant cooling rates, shear rates, and temperatures, is required to understand polymer behaviors during polymer melt flow manufacturing, and to optimize the solidified polymer for subsequent applications. Introducing shear flow to the polymer melt can influence microstructure development because melt flow can affect crystallization kinetics, crystal structure/polymorphism, morphology after solidification, local and bulk properties. The engineering thermoplastic polyamide 66 (PA 66) is of particular interest due to its complex solidification behavior that must be controlled during melt processing. PA 66 is often denoted as a polymer plagued by difficulties related to shrinkage and warpage, factors that are driven by the crystallization process.

The thesis of this work is to discover and describe the behavior of PA 66 as it crystallizes after melt flow. In this dissertation, the quiescent crystallization kinetics of PA 66 are first described as a reference to understand the microstructure development at fast cooling and temperatures spanning from the glass transition to close to melting, or high and low supercooling of the melt, respectively. Then the neat PA 66 was studied using a combined rheological and calorimetric approach to understand the crystallization behavior of the sheared melt under process-relevant crystallization conditions, and it was discovered that a critical shear rate of 0.1 s^{-1} and a critical work of 0.1 MPa is required to produce chain stretching, resulting in reduced crystallization time. Parallel plate rheology was used as a sample preparation tool to produce known shear history prior to calorimetric and morphological analysis. This novel methodology proved that the flow-induced precursors act like heterogeneous nucleation sites, decreasing the half-time of crystallization at the optimal temperature of 170 °C to 0.14 s, while crystallization that occurred at temperatures dominated by homogeneous nucleation was not influenced by the shear history. The thermal stability of flow-induced precursor (FIP) above the observed melting temperature suggests the FIP is a reduced-entropy transition stage between the homogenous melt and crystal. The stretched polymer embedded within flow-induced precursor is a critical factor for the studies of the pre-sheared materials since it induces a faster crystallization.

Carbon nanotubes (CNT) in the PA 66 were used to (1) study the nucleating efficiency of the nucleated system as crystallization from the CNT surface is hypothesized to mimic that from the shish precursor and (2) determine if the CNT nanocomposite provides a synergistic nucleating

effect when subjected to flow. It was found that the nucleating efficiency of the CNT dominated any nucleating effects of flow in the PA 66 system. The onset of crystallization time was found to be a function of CNT content, where higher CNT loading reduced the onset time. When the CNT loading developed a saturating network within the polymer matrix, there were no effects of shear flow on crystallization, leading to the conclusion that there is a saturation point for heterogeneous nucleation regardless of the source. However, if CNT loading is under the saturation limit, shear flow can still accelerate crystallization if over the critical work level.

To summarize, this thesis provides insights into the crystallization kinetics of the engineering thermoplastic PA 66 and its CNT nanocomposite under both quiescent and post-shear flow conditions. It is anticipated that this research helps illuminate the crystallization process and aids in the improvement of melt processing of PA 66.

Acknowledgements

Glory to God

for His countless blessings, grace, and protection.

My journey as an external PhD student at Martin Luther University has been a non-traditional and challenging path, for which I am so grateful for the patience of my advisor, **Dr. René Androsch**. With his guidance, I have been able to deeply explore the world of polymer microstructure these past five years. I will forever be thankful for your technical mentorship, encouragement, and long-distance perseverance. Without your support, I would not have been able to complete this PhD study. I am also sincerely grateful for my local supervisor, **Dr. Alicyn Rhoades**, who has been such an inspiration to my career. Working with her is always an exciting, fast-paced environment with new challenges to overcome. I want to thank you specifically for ensuring the funding for my position at Penn State University and travels for working on my PhD have always been met. The completion of my PhD would not be possible without the faculty and institutional support of both Martin Luther University and Penn State University.

In my time working on my PhD, I have been able to work with such great colleagues and collaborators. I want to thank specifically **Katalee Jariyavidyanont**, who is always so helpful with administrative questions as I navigated the MLU system externally and with technical support as we studied the rheological and calorimetric fields of plastics engineering. In the PSU system, I am deeply grateful to **Dr. Ralph Colby**, **Dr. Xiaoshi Zhang**, and **Dr. Jiho Seo** for their insightful conversations about my experiments and data.

I would like to dedicate this work to my husband, **Nathan**, our baby, **Jonah**, and my parents, **Scott** and **Eileen**. Nathan, you have been my support system, best friend, and most enthusiastic cheerleader through this challenge in my life. I love you so much. Baby Jonah, my biggest wish is that you have a life of love, joy, wonder, and achievement. Your snuggles and smiles helped get me to this point, and I hope you can look at this work someday and know I finished it for you. Mom and Dad, I am so grateful that you always supported me and my career, even though it meant we had to be geographically apart for so many years.

Without all of these people, I would not be the person I am today, and for that, I am so grateful.

Anne Gohn

Table of Contents

List of symbols and abbreviations

HDPE	high density polyethylene
HMWPET	high molecular weight poly(ethylene terephthalate)
h-PBD	hydrogenated polybutadiene
iPB	isotactic poly(1-butene)
iPP	isotactic polypropylene
LLDPE	linear low density polyethylene
PA 11	polyamide 11
PA 66	polyamide 66
PBT	poly(butylene terephthalate)
PE	polyethylene
PEEK	poly(ether ether ketone)
PLA	poly(lactic acid)
PLLA	poly(L-lactic acid)
PP	polypropylene
PPS	polyphenylene sulfide
$\dot{N}_f$	flow-induced nucleation rate
$\dot{\gamma}$	shear rate
AFM	atomic force microscopy
CNT	carbon nanotube
d-spacing	distance between planes of atoms
DSC	differential scanning calorimetry
ERM	entropy reduction model
ETD	electrical temperature device
FIC	flow-induced crystallization
FSC	fast scanning chip calorimetry
$\dot{G}$	linear growth rate of spherulites
h	gap height
k	Boltzmann constant
M_e	entanglement molecular weight

M_n	number-averaged molecular weight
M_w	weight-averaged molecular weight
NHSK	nanohybrid shish-kebab
POM	polarized optical microscopy
r	radius
SAOS	small-amplitude oscillatory shear
T_c	crystallization temperature
TEM	transmission electron microscopy
T_g	glass transition temperature
T_m	melting temperature
T_m^0	equilibrium melting temperature
t_s	shearing time
W	specific work of flow
WAXS	wide-angle X-ray scattering
W_c	critical work level
Wi	Weissenberg number
W_{sat}	saturated work level
γ	shear strain
ΔT	degree of supercooling
ΔG_d	activation energy barrier for diffusion
ΔG_f	activation energy barrier for nucleation
η	viscosity
η^*	complex viscosity
σ	shear stress
τ_e	Rouse time of an entangled strand
τ_R	Rouse time
ω	angular frequency

1. Introduction

Polymer microstructures are highly dependent upon shear flow. Historically these microstructures (spherulites, row-oriented spherulites, shish-kebabs) have been studied under controlled laboratory conditions that do not properly represent the complex conditions present during manufacturing with melt processing techniques, such as polymer extrusion or plastics injection molding. To properly understand the development of solidified polymer properties, which is driven in part by polymer crystalline microstructure, the polymer shear flow inherent in melt processing must be thoroughly understood. The recent development of Fast Scanning Chip Calorimetry (FSC) allows for the investigation of crystallization kinetics at high and low supercooling of the melt, which better mimics the crystallization temperatures and rates observed in processes like injection molding. However, only a few studies have attempted to understand the link between the shear flow during manufacturing and the subsequent crystallization that occurs during the cooling phase of complex polymers such as PA 66. In this work, the flow-induced crystallization (FIC) behavior of polyamide 66 (PA 66) is explored at process-relevant cooling rates and temperatures. Important analytical tools used in this work to probe flow-induced crystallization and characterize PA 66 include calorimetry, melt rheology, and spectroscopic techniques.

The high-temperature stability of the oriented polymer fraction, a driving hypothesis investigated in this work, plays a key role in the development and persistence of experimentally observed FIC. The oriented polymer fraction resulting from the shearing process is unstable in the melt. Specifically of interest is the shish, an extended chain formed when polymer is subject to the flow. To investigate the crystallization kinetics after flow, a desired shear history was imparted on the polymer melt using melt rheology. Then, the sheared disk was further analyzed on FSC. After selective melting to keep FIC, the sheared polymer sample was isothermally crystallized to explore the crystallization kinetics at high rates and high supercooling.

The instability of the oriented polymer chains above the observed melting temperature creates difficulty in determining its influence on the crystallization process. To study FIC without the uncertainty with regard to shish relaxation, it was hypothesized that carbon nanotubes (CNT) could replace shish, providing a geometrically equivalent surface from which the relaxed polymer melt could nucleate. Subsequent crystallization could then be studied without the potential thermal instability of the polymer shish-precursors. The crystallization kinetics of the PA 66 sheared

system was compared to that of the CNT nanocomposite to analyze the nucleation efficiency of a flow-induced vs foreign-heterogeneously nucleated system. The flow-induced behavior of the nanocomposite was then investigated to explore the potential for cumulative effects of nanotubes and shear flow.

This work will contribute to (1) furthering the understanding of structure-property relationships in polymer systems exposed to shear flow and (2) improving material development and selection for advanced engineering applications. By analyzing the flow-induced crystallization in the engineering polymer PA 66, it is expected that the results obtained can enhance the understanding of other polymer systems.

2. Objectives

This work aims to determine the critical parameters that control flow-induced crystallization in PA 66, including the amount of shear work, the longevity of flow-induced structures in the melt, and the potential for the interaction of both nanotube/flow-induced nucleation in a single PA 66 system. In typical plastics manufacturing processes like injection molding, extrusion, blow molding, or thermoforming, a molten polymer material is forced to flow to conform to a desired part shape. Currently, there is little information about the crystallization of engineering polymers after exposed to shear, and the studies that have been conducted were performed at low cooling rates and high temperatures. This thesis aims to combine rheology and fast calorimetry techniques to more closely represent the crystallization at rates and temperatures that reflect the manufacturing process. Since the FIC behavior at high supercooling is not well understood, it is hypothesized that the flow-induced precursors drive heterogeneous nucleation but do not enhance homogeneous nucleation. It is also speculated that particulate additive nucleation of a similar shape factor is more effective because CNT is more persistent in the melt than the precursors, which can relax at temperatures over the equilibrium melting point (T_m^0), the temperature where a crystal of infinite size is melted and therefore all nuclei are destroyed. Above T_m^0, no nuclei can survive, hence the polymer is considered to be a relaxed state.

The engineering thermoplastic polyamide 66 is used as the base resin due to its great industrial importance. A systematic investigation was conducted to analyze the crystallization of the quiescent polymer from the melt, the crystallization of the neat polymer after shear flow, and the crystallization of PA 66/CNT nanocomposites. It is hypothesized that the CNT should mimic the nucleating behavior of the shish in the sheared melt because of the similarity in high aspect ratio, allowing for milder processing to achieve similar nucleating and reinforcing properties. This will allow for further evaluation of heterogeneous nucleation from an oriented fraction that is stable during thermal analysis characterization. A comparison of the kinetics of the flow-induced crystallization (FIC) and the nanocomposite crystallization is performed in order to establish the nucleating efficiency in the PA 66 system. The subsequent crystallization after shear flow in PA 66 both with and without CNTs are discussed.

To understand the quiescent crystallization of the neat resin, fast scanning chip calorimetry (FSC) is employed to evaluate crystallization over a wide range of cooling rates and at various degrees of supercooling. Subsequent analyses of the specimens included using wide-angle X-ray

scattering (WAXS), polarized optical microscopy (POM), and atomic force microscopy (AFM) to further the understanding of microstructure development based on specific crystallization conditions. A thorough understanding of the quiescent crystallization of PA 66 is still lacking in the literature, and this work intends to shed more light on the neat, quiescent system.

Neat PA 66 samples were prepared at known shearing conditions using a parallel plate rheometer, which can induce a specified shear rate for a precise amount of time. Samples were then quenched to the solid state and subsequently analyzed to determine crystallization characteristics under process-relevant heating and cooling conditions. The stability of the flow-induced nuclei at temperatures above the observed melting temperature is critical to the success of these experiments because unstable nuclei cannot be relied upon for a series of calorimetric experiments that repeat cooling/melting series at variable rates or temperatures.

Carbon nanotubes were added to the PA 66 at low loadings in order to analyze the nucleating efficiency of the nanotubes system under quiescent conditions as crystallization from the CNT surface, which may mimic nucleation that occurs that from the surface of a shish precursor. The synergistic nucleating effects of CNT and flow were also evaluated to further the understanding of (1) the role of CNT on PA 66 chain stretching, (2) synergistic effects of CNT and flow on PA 66 crystallization kinetics, and (3) relaxation effects with polymer chain entanglements/mobility restriction with the CNTs.

The resulting crystallization kinetics can be applied as inputs to melt flow simulation, where molten polymer is forced to flow to fit a specified part geometry, followed by fast cooling to a temperature below the glass transition. The crystallization of the heterogeneously nucleated material is determinative for final part properties including chemical resistance, strength, toughness, and dimensional stability. By better understanding the crystallization kinetics at process-relevant conditions (shear history, high cooling rate), engineers can better predict and tailor crystallization for final part properties. In summary, the crystal nucleation efficacy of flow-induced formed nuclei and carbon nanotubes, as well as their combined effect in the engineering polymer polyamide 66 are analyzed, allowing adjustment of optimum processing parameters to tune the development of specific material microstructures.

3. Literature Review

3.1 Quiescent polymer crystallization

3.1.1 Crystallization fundamentals

Thermoplastics are categorized into the subclasses of amorphous or semicrystalline polymers, where the amorphous materials remain disordered and semi-crystalline materials can fold into regions of ordered state. Due to the high molecular weight of the polymer molecules, the chains are entangled and prevent the material from reaching 100% crystallinity [1]. Therefore, polymers are referred to as semi-crystalline if they can crystallize, typically reaching a maximum of about 30-60% crystallinity [2,3]. If the chemical structure is irregular or disrupted such that it does not allow for packing into a more dense crystalline state, or if cooling is fast enough to prevent kinetic reorganization, the system remains amorphous. In quiescent crystallization, the polymer material forms crystals in the absence of shear forces, stresses, or pressure above atmospheric conditions.

When polymers crystallize, they densify into a three-dimensional structure with a certain level of orders to form a more ordered structure. During growth, the structure repeats to form a crystal lamella, of which several lamellae can organize to comprise larger superstructures such as spherulites. Some polymers, including polyamide 66, display polymorphism, defined as the ability to pack into differing unit cell geometries depending on the crystallization conditions. From a thermodynamic point of view, in order to crystallize, the macromolecule needs to rearrange to form a more ordered structure, leading to a volume free energy reduction that is sufficient to overcome the penalty from the entropy change. It should be noted that polymer crystallization is a kinetic process, and the relationship between the nucleation rate and crystallization temperature can be described by the Turnbull-Fisher equation [4]

$$\dot{N}_f = C \exp\left(-\frac{\Delta G_d}{kT_c}\right) \exp\left(-\frac{\Delta G_f}{kT_c}\right) \tag{1}$$

where $\dot{N}_f$ is the nucleation rate and ΔG_d and ΔG_f are the diffusion activation energy and nucleation energy barrier, respectively, and C, k, and T_c are a temperature-independent constant, the Boltzmann constant, and the crystallization temperature, respectively.

Polymer crystallization occurs in two steps: nucleation and growth. Experimentally, crystallization is often studied in the polymer solution or in the polymer melt. Here, we only focus on polymer crystallization from the melt. In the nucleation step of crystallization, a nucleus, or

origination point of crystal growth, develops from the melt. As temperature decreases, the critical nucleus volume to initiate crystallization decreases, therefore reducing the free energy barrier [4]. Alternatively, a foreign particle present in the polymer melt may act to heterogeneously nucleate crystallization. To reach homogeneous nucleation, where nuclei develop from the bulk polymer melt, a high degree of supercooling ($\Delta T = T_m^0 - T_c$) is necessary [5]. Once a stable nucleus is developed, crystal growth can expand from a favored surface.

When crystallized from the melt under quiescent conditions and at high temperatures or relatively low cooling rates, polymer chains first fold and organize into crystalline lamella, which stack and build radially from the center point of nucleation. Crystal growth occurs in three dimensions from the nucleus, and lamellar stacking ultimately forms a sphere-like structure, typically referred to as *spherulites*. A heterogeneous nucleation point initiates the crystallization process, and the lamellae grow radially outward in all directions until impingement takes place. After impingement, secondary crystallization, a space-filling process occurs whereby amorphous regions between the main lamellae subsequently crystallize. In addition, during secondary crystallization, crystal perfection rearrangements can occur that result in measurable lamellar thickening. A schematic representation of the unit cell, the crystal lamellae, and the spherulite superstructure, is provided in Figure 1. Theories regarding crystal growth have been postulated as a fringed micelle model (Hermann) [6], sharp fold model (Keller) [7], switchboard model (Flory) [8], adjacent reentry (Hoffman) [9], intramolecular nucleation (Hu) [10], or a combination of the proposed models. The most common polymer crystallization growth theory has been proposed by Hoffman and Lauritzen (1960), where a linear growth rate ($\dot{G}$) of spherulites is determined as a function of supercooling [11]. In this simplistic model, it assumes the first stem of polymer attaches on the growth surface at a rate of i. After this step, the secondary nucleus spreads out laterally with a rate of $\dot{g}$. The spreading of the secondary nucleus will continue to form a smooth surface for subsequent attachment.
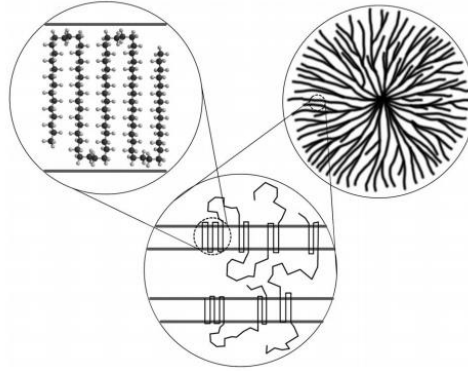
Figure 1: Schematic representing spherulite composition from the bulk melt crystallization, crystal lamella, and polymer-specific unit cell packing. Reprinted from [12] https://doi.org/10.1039/C0SM00070A with permission from The Royal Society of Chemistry.

Regardless of the specifics of chain folding, polymers are unable to crystallize completely due to chain entanglements and imperfections prohibit crystallization, and therefore some fraction of the solidified polymer remains amorphous. Figure 2 depicts amorphous regions between crystal lamellae. Amorphous regions that are covalently linked to the crystals as exiting chains are mobility confined, and comprise the rigid amorphous fraction of the solidified matrix [13,14]. If an amorphous region is disconnected from the crystal regions it has increased mobility, and this phase is known as the mobile amorphous fraction [15]. In polymers, the glass transition temperature (T_g) is the temperature where the free volume in the system is sufficient to allow large-amplitude motion of molecular segments, which causes a transition from glassy to rubbery state on heating. In the amorphous region, tie molecules can connect separate lamellae, meaning a single chain is incorporated into separate lamellae and spans an amorphous region, and thereby confer on polymers their high strength properties.
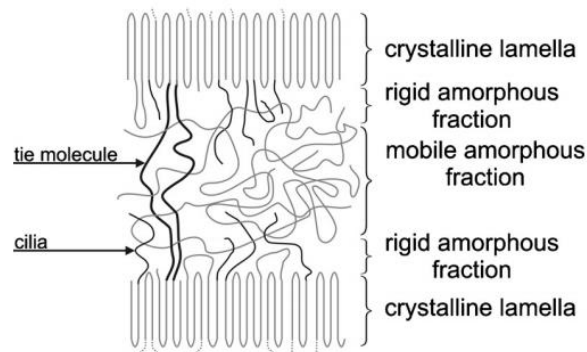

Figure 2: Schematic demonstrating crystal lamellae, and rigid and mobile amorphous fractions. Reprinted from [16] https://doi.org/10.1063/1.3462312 (AIP) with permission from AIP.

Depending on the degree of supercooling, the crystallization process is either nucleation or mobility limited. At high temperatures (low supercooling) the energy barrier to nucleate the system is high. The material is restricted from nucleating crystallites, resulting in an increase in crystallization time and a decrease in growth rate. At low temperatures nearing the T_g, the system is diffusion controlled, where there is low chain mobility, and again, crystallization time increases and growth rate decreases. In the middle region between T_g and T_m, the conflict between mobility and nucleation control is minimal, resulting in the most favorable temperatures for crystallization indicated by a minimum in crystallization time. This behavior is depicted in Figure 3. Additionally, the nucleation density is a function of the degree of supercooling, where an increase in nuclei density, and thus reduction in superstructure size, occurs at lower temperatures [17]. The critical volume to form a nucleus is reduced at lower temperatures [18,19]. A bimodal crystallization time behavior has been observed in many polymers, including isotactic polypropylene (iPP) [20,21], polyamide 66 [22], polyamide 11 (PA 11) [23], and poly(butylene terephthalate) (PBT) [24], where a local minimum in the temperature dependence of the crystallization rate signifies the nucleation mechanism change from heterogenous to homogeneous with decreasing temperature.
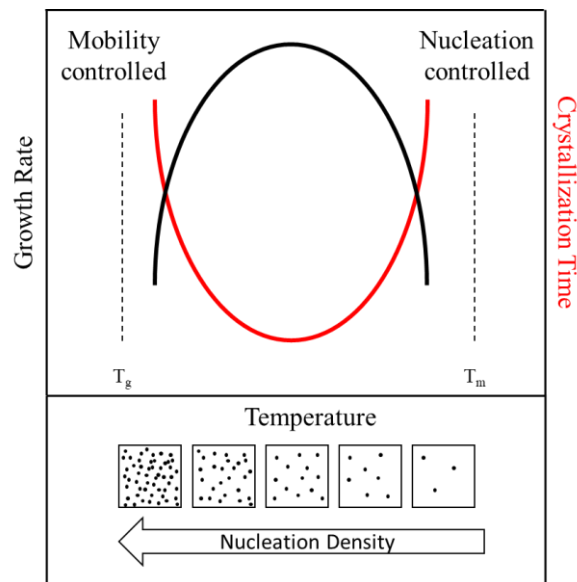

Figure 3: Growth rate, crystallization time, and nucleation density (for a given mechanism) as a function of temperature.

3.1.2 Polyamide 66 quiescent crystallization

Polyamides are engineering thermoplastics linked by amide bonds. The nomenclature for the polyamide materials, PA xy, follows the number of carbon atoms, x and y, in the diamine and

diacid groups, respectively. In this work, polyamide 66 is studied, though the material family can include odd, even, even-even, odd-odd, and odd-even x-y configurations [25]. Even-even polyamides, like PA 66, can form three main polymorphs when crystallized from the melt, depending on the crystallization conditions. The more stable α-form crystal develops on slow cooling or at high crystallization temperatures. In this arrangement, the molecules form into a triclinic unit cell with a planar zigzag conformation. Hydrogen bonding occurs between amide groups of adjacent chains, where the oxygen atom of the amide group from one chain is aligned with the hydrogen atom of the amide group on the neighboring chain [26–32]. The development of the α-form at slow cooling and high temperatures has been linked to the development of spherulites [33–36].

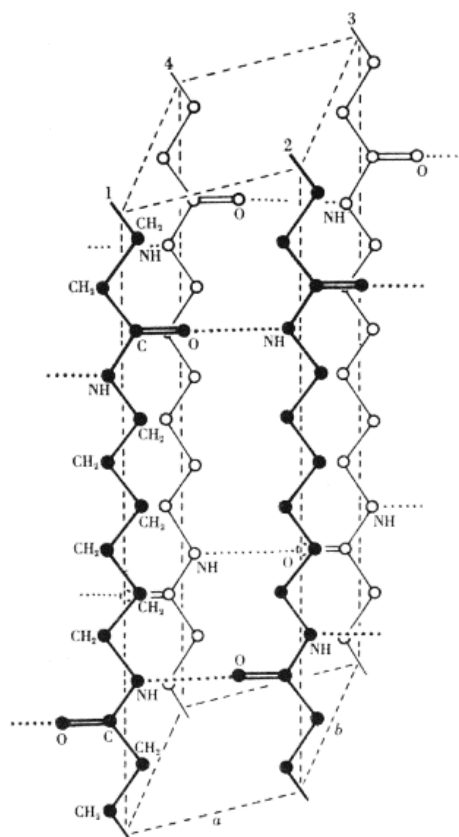*Figure 4: PA 66 α-form unit cell. Reprinted from [26] https://doi.org/10.1098/rspa.1947.0028 with permission of The Royal Society.*

When the α-form is heated above approximately 175 °C, the structure changes from triclinic to pseudohexagonal, producing the α'-modification. This polymorphic switch is known as the Brill transition [37,38]. On cooling from high temperature, the α'-phase converts back to the α-phase

and is not viable at room temperature. In the third crystal form, the γ-mesophase develops when quenched from the melt [27]. In this polymorph, a pseudohexagonal unit cell of non-planar arrangement of hydrogen bonding is present [27]. This polymorph is metastable, and on heating, the γ-mesophase transforms irreversibly into α'/α-crystals [39].

When crystallized isothermally from the melt, PA 66 displays a bimodal distribution of peak time of crystallization, or maximum rate of crystallization, which has been reported for many other polymer systems including iPP [20], PA 6, 11, and 12 [23,40–42], and PBT [43]. The high-temperature and low-temperature relative minima of crystallization time were found to be 165 and 110 °C, respectively, with a local crystallization rate minimum at 130 °C [22]. When the non-isothermal crystallization kinetics were studied using FSC, it was found that crystallization is suppressed at rates over 100 K/s and is completely absent at 500 to 1,000 K/s [22]. Later chapters of this dissertation are dedicated to understanding the crystallization of PA 66 under quiescent conditions to link crystallization temperature and rate to the resulting microstructure and polymorph (Chapter 6.1.1).

3.2 Heterogeneous nucleation in polymer composites

The inclusion of foreign materials is often required to modify specific polymer properties in engineering applications. These foreign materials can be classified as reinforcing agents, nucleating agents, functional additives, fillers, and processing aids depending on their purpose. Engineers can tailor properties such as mechanical strength, electrical or thermal conductivity, UV stability, impact resistance, and wear resistance for desired utilization [44]. Polymer composite systems are designated as multi-phase systems that are combined to alter the properties of the final material. Depending on the size of the reinforcing agent, the material system is designated as a micro- or nano-composite [45]. Common materials used in micro-composite polymer systems include glass, carbon, calcium carbonate, talc, clay, and natural fibers, and the shapes and sizes of these materials can vary depending on material and its preparation [44]. In recent years, the exploration of nano-composite systems has yielded fruitful efforts, where material properties can be dramatically tailored at relatively low loading levels due to the high surface area contact between the polymer matrix and the nano-additive [46]. Specifically, carbon nanotubes have been at the cutting edge of this revolutionary composite development. CNT-polymer composites are

targeted to be used in high-strength composites in the automotive, aerospace, and construction industries, along with applications in fuel cells and energy devices [47].

The reinforcing agent can also affect both nucleation and crystal growth in the polymer. Similar to the flow-induced phenomenon to be discussed in Chapter 3.3, foreign materials included in composite systems can act as a site for heterogeneous nucleation for the polymer melt. By lowering the energy barrier for nucleation, the crystallization induction time can be reduced, and crystallization can initiate at higher temperatures under non-isothermal conditions and more nucleation sites can occur from the surface of the heterogeneity [48]. The size and shape of the nucleating surface can also affect crystal growth, whereby the growth mechanism may change from spherulitic in the neat melt to trans-crystallization from a particle/fiber surface [49–51]. The inclusion of micro- and nano-materials in the polymer matrix has been shown to increase the nucleation density of the polymer matrix, producing smaller, more confined crystal domains [52]. In some cases, nucleation from foreign substrates can also affect polymorphism in polymer materials [53]. Crystallization at high supercooling has been found that the nucleating activity of nanocomposites only affects the heterogeneous nucleation regime [41,42,48,54]. Homogeneous nucleation at high supercooling remains unaffected by the inclusion of nanomaterials and nucleating agents. However, the addition of the nanoparticle can widen the window permitting heterogeneous nucleation, indicated by a reduction in the crossover temperature from heterogeneous to homogeneous nucleation [24,41,42].

In the case of quiescent crystallization, CNT nanocomposites, where the tube's aspect ratio is similar to that of a flow-induced precursor, crystallization behavior resembling the growth of shish-kebab structures has been documented under quiescent conditions in the polymers polyethylene (PE) and PA 66 [55]. As shown in Figure *5*, the CNT provides a nucleation surface for subsequent crystallization, and nanohybrid shish-kebab (NHSK) structures were grown in the absence of shear. PA 66/CNT nanocomposites studied by calorimetry have also displayed ultralow saturation threshold, where the saturation point for peak crystallization temperature on cooling was reached at only 0.04 wt-% CNT as studied by standard differential scanning calorimetry (DSC) [55]. Other PA 66/CNT nanocomposite studies confirm mechanical and thermal property saturation at low loadings, under 1 wt-% [56], and a reduction in spherulite size with addition of CNT as studied by DSC [57,58].
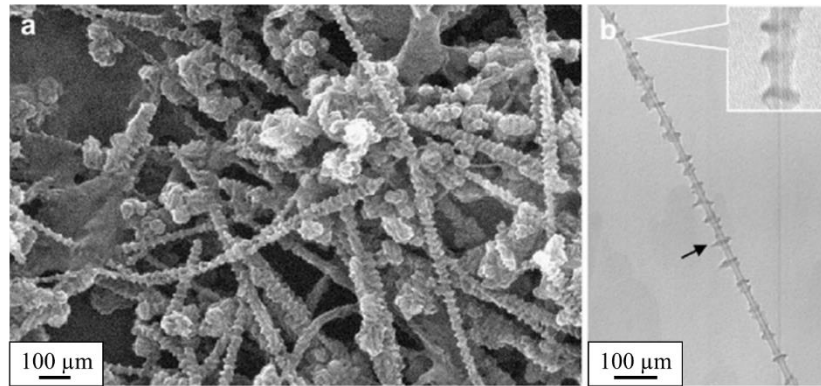
Figure 5: Nucleation of PA 66 crystals from MWCNT at 185 °C in glycerin observed by (a) SEM and (b) TEM. Reprinted from Carbon nanotube induced polymer crystallization: The formation of nanohybrid shish–kebabs, Volume 50, Issue 4, Lingyu Li, Bing Li, Matthew A. Hood, Christopher Y. Li, 958, Copyright (2009), with permission from Elsevier.

3.2.1 Self-seeding nucleation

Self-nucleation, also known as self-seeding, of polymer crystals is associated with the crystal formation from existing nuclei or surfaces from the polymer's own structures. This type of nucleation is achieved by heating to the molten state, but not quite hot enough or for a long enough time to completely melt existing crystal species. Upon subsequent cooling, the molten phase will heterogeneously crystallize from the existing structures/surfaces. Self-seeding behavior has been proven to occur in PA 66 [59], but also PA 6 [60–63] and PA 11 [64]. Research has shown that the self-nucleation causes a reduction in time required for crystallization, where crystallization rates are increased with the additional reduction in maximum temperature [59]. The resulting superstructure is also affected, where an increasing reduction in spherulite size is noticed with decreased maximum temperature [64]. It is important to note that in most cases the self-seeding behavior is present at temperatures higher than the completion of the endothermic melting peak up to the equilibrium melting temperature, where all nuclei are confidently erased [64]. In several experiments this work relies upon self-seeding nuclei, and therefore, maximum temperatures and time in the melt are designed to preserve nuclei within a series of experiments.

3.3 Flow-induced crystallization

3.3.1 Flow-induced crystallization fundamentals

When a semi-crystalline polymer solidifies from the melt after being exposed to a shear field, the crystallization process is affected by the shear history. In the flow field, where the polymer

melt is forced to move at a given speed for a prescribed time, the high molecular weight of the molecules and the frictional forces in the melt cause the molecules to orient in the direction of flow. The high molecular weight fraction is the first to orient in the flow field, and with increased shear history, lower molecular weight chains are able to orient with flow [65,66]. The polymer molecules that are oriented during flow can relax back to the isotropic state. However, this relaxation is dependent on temperature and time, or *relaxation time*. For shearing to affect the subsequent crystallization process, the oriented molecules need to be long enough to exceed the melt's relaxation time. If this rule is met, the oriented molecules stay aligned during solidification, and are then identified as "stretched" molecules.

The transition between regimes where flow-induced crystallization (FIC) is non-existent and FIC is present is demonstrated using the Weissenberg number (*Wi*),

$$Wi = \dot{\gamma}\tau_R \tag{2}$$

where $\dot{\gamma}$ is the shear rate in the system and τ_R is the Rouse time, or stretching relaxation time of the longest chains. It is known that the stretching, and therefore relaxation, of the longest chains in the molecular weight distribution, is the critical factor in the onset of FIC [67]. Chain stretching only takes place when the flow time $\dot{\gamma}^{-1}$ is shorter than the disentanglement time, meaning that values of $W_i < 1$ yield no effect of flow on crystallization and $W_i > 1$ shows an impact on crystallization after flow [68]. With increasing shear rate, shorter chains can also stretch and contribute to FIC. Flow-induced precursors in the polymer melt also exhibit a distinction regarding the effects of orientation and stretching, related to magnitude and stability of the precursor structures [69]. To obtain oriented chains, the shear rate must be greater than the inverse of the reptation time and less than the inverse of the Rouse time ($\dot{\gamma} > 1/\tau_{rep}$ but $\dot{\gamma} < 1/\tau_R$) , and the resulting microstructure yields higher nucleation density, and spherulites can be oriented in the direction of flow. With increasing shear rate, where $\dot{\gamma} > 1/\tau_R$, the high molecular weight molecules reach the stretched state which develops the shish core of the subsequently formed shish-kebab structure. With increasing molecular weight, the relaxation time is also increased, as the high M_w chains have higher temperature stability in the melt than shorter chains.

Extensive work has been done to find the critical flow parameters that induce the oriented/stretched precursors that affect crystallization. Researchers have explored shearing time [70,71], shearing rate [72], and shear strain [73] as the critical parameters, but it is the relationship between these factors that determine the critical flow parameters [74]. This relationship is

calculated as the specific work of flow (*W*), herein referred to only as specific work or shear work, and is designated as

$$W = \sigma\gamma = \eta\dot{\gamma}^2 t_s \tag{3}$$

where σ is the shear stress and γ is the shear strain. Substitutions can be made to extend the equation to incorporate the viscosity as a function of a specific shear rate η and temperature, the shear rate $\dot{\gamma}$, and shearing time t_s [69,74–76], as given in Equation 2. It has been found that, even though the relationship between these factors describes the crystallization acceleration resulting from flow, shear rate and time must meet a minimum threshold to affect the subsequent crystallization [73].
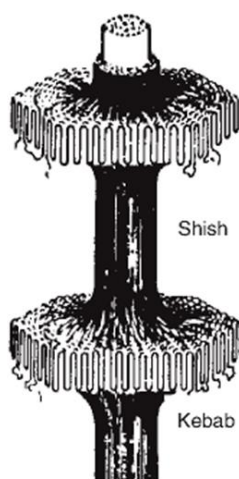
Figure 6: Shish-kebab schematic where the "shish" center core is comprised of stretched molecules, which nucleate trans crystallization of laterally grown lamellae, "kebabs," from their surface. Reprinted from Handbook of Polymer Crystallization, Ewa Piorkowska, Gregory C. Rutledge, 166, Copyright (2013), with permission from Wiley.

The crystal development after flow is described first as a reduction in size of spherulite structures. With increased shear history, spherulites with row-oriented nuclei in the direction of flow are observed. When enough shear work is applied to the system in which oriented molecules are unable to relax, they can nucleate crystal growth from their surface. The bundle of oriented chains, or extended chain crystals, are referred to as the "shish" and the group of crystallites that nucleate from this surface is designated as the "kebab", forming together the well-known "shish-kebab" geometry. This superstructure is also referred to as a cylindrite in the literature [77–80], but for the remainder of this work, it will be referred to as the shish-kebab structure. The extended chain crystal [81] that comprises the shish is developed from the high M_w fraction, where the molecules align to form bundles of stretched fibrils [65,66]. Similar to that in a heterogeneously

nucleated system, the nucleation rate is increased from the sheared polymer in comparison to that of the neat, quiescent melt if critical shearing conditions are met [70,71].

Figure 7 shows Housman's model [82] depicting a schematic representation of how the amount of shear work of flow impacts the subsequent crystallization process. As discussed, there is a minimum value of shear work or critical work level (W_c), that is required to induce the FIC process. Below W_c, there is no effect on crystallization in the system (Regime I). Once the critical level of work has been attained, the crystallization rate is increased and resulting microstructure is affected where first with the development of fine nuclei where spherulite nuclei can be oriented in the direction of flow or spherulite size is reduced, where $\dot{\gamma} > 1/\tau_{rep}$ but $\dot{\gamma} < 1/\tau_R$ (Regime II). Regime III indicates where shearing may be greater than $1/\tau_R$, but chain stretching does not occur to produce shish precursors. Finally, the growth of shish-kebab features (Regime IV), leads to further reduction in crystallization time. This behavior has been tested and verified many times in polyolefins [82–88], but also poly (lactic acid) (PLA) [89,90], isotactic poly(1-butene) (i-PB) [88], polyamides [71,91], and poly (ether ether ketone) (PEEK) [92].
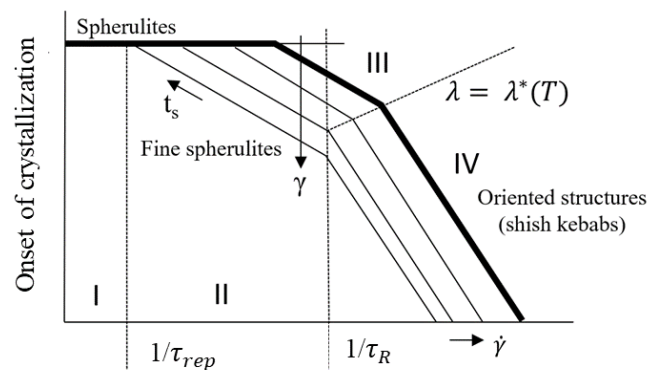

Figure 7: Onset of crystallization as a function of shear rate. Regime I indicates spherulitic growth where the critical work level has not been met. Regime II indicates shear levels over W_c that yield row nuclei or fine spherulites. Regime III indicates where shearing may be greater than $1/\tau_R$, but chain stretching does not occur to produce shish precursors. Regime IV indicates stretched shish are stable in the melt. Adapted from Ref [82], distributed under the terms of the Creative Commons Attribution Noncommercial License.

The formation of the oriented fraction, or flow-induced precursor, nucleates crystallization upon cooling of the melt. The nucleation rate and nucleation energy barrier are both a function of the magnitude and duration of shear flow. This change in nucleation activation energy is represented conceptually in the schematic shown in Figure 8, where the classical free energy

diagram is displayed (a). In this diagram, it is shown that in order to form a crystalline phase, polymer liquid phase (either in solution or melt) needs to overcome a free energy barrier (ΔG). The energy barrier is reduced with flow-induced entropy reduction since the free energy of the liquid phase increases due to orientation and reducing the randomness of the melt [93]. It is proposed that the energy required to surmount the energy barrier in the liquid state is decreased when subjected to flow because the stretched fraction is in a state possessing some degree of molecular order (b).
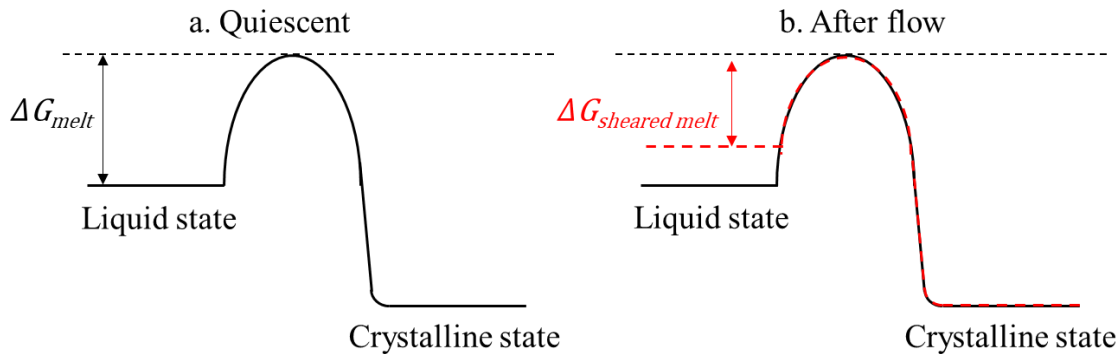

Figure 8: Free energy diagrams showing changes in nucleation activation energy and free energy of the liquid state and resulting crystalline state due to flow [94].

In addition to affecting nucleation rate, shear history has also been shown to increase the crystal growth rate in polymers, where increasing shear rate increases the spherulitic growth rate [71,87,92,95,96], postulated to be due to the increase in equilibrium melting temperature after flow [95]. The crystal growth rate after shearing the melt can either be monitored optically by shearing under polarized light and directly measuring spherulitic growth with time [87,95] or by analyzing the increase in viscosity or modulus with increasing crystalline content in a rotational rheometer [71,92]. When analyzing the effects of shear on crystal nucleation and growth in PLA, it was found that there is similar contribution to both factors, though the effect of growth rate is slightly larger [96].

The common free energy diagram is depicted in Figure 9, where the energy of the quiescent polymer melt (G_{melt}), sheared polymer melt ($G_{sheared\ melt}$), and the energy of the crystalline phase ($G_{crystal}$) are shown as a function of temperature. It can be seen that the $G_{sheared\ melt}$ is at a higher free energy state than the G_{melt}, as the oriented fraction decreases the entropy of the system. The slope of each phase is related to its degree of entropy, where the lowest to highest are depicted as the crystalline state, the sheared melt, and the quiescent melt, respectively. The free energy diagram

is depicted for both (a) if shearing is under the critical level to produce flow-induced precursors, and (b) if the shearing is over the critical work level to affect crystallization. As temperature increases from the solid, crystalline phase, it is shown that the cross-over to the quiescent melt occurs at a lower temperature than that of the sheared melt, indicating a lower melting temperature is necessary for the quiescent material than for the sheared counterpart. This has been proven theoretically by many entropy reduction models and experimentally by in-situ small and wide angle scattering (SAXS and WAXS) measurements using polyethylene, where higher melt temperature was needed to melt the stretched shish fraction relative to the lamellar kebabs [97]. High temperature stability of sheared materials has also been demonstrated in iPP [98] and PEEK [99] materials. By contrast, as temperature is decreased from the melt state, the crystallization on cooling occurs at a higher temperature from the sheared melt than from the quiescent melt.
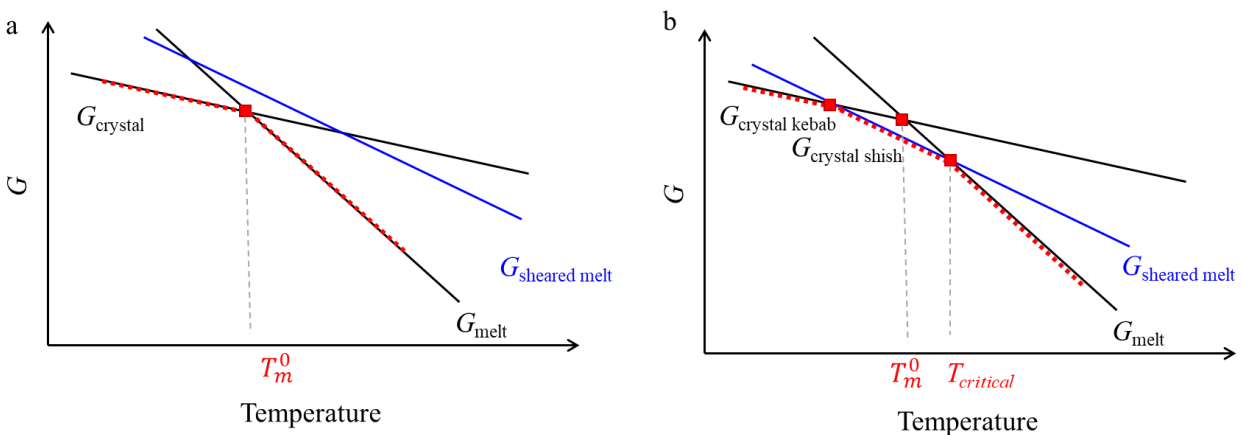

Figure 9: Free energy of the sheared melt, quiescent melt, and crystalline state. The free energy is shown if the sheared melt is under a critical level (a) or if it is over a critical level (b), to affect crystallization. The sheared melt is at a higher free energy state, resulting in an increase in the critical temperature to erase flow-induced nuclei. The red dashed line indicates the lowest energy path.

The onset of FIC is detected using parallel plate rheometry at the divergence in viscosities as measured by oscillatory and steady shear, known as the Cox-Merz rule failure [100]. According to this rule, when comparing the viscosity of the oscillatory sheared sample to that of the steady sheared sample, the onset of orientation results in a decrease in viscosity from that of the oscillatory signal. The behavior in a typical Cox-Merz analysis is displayed in Figure 10, where the divergence of the steady shear and complex viscosities would indicate the critical shear rate to produce oriented molecules. The conformance to the Cox-Merz rule in shear rate experiments

applied to onset of FIC has been proven for polymers such as iPP [101], PA 66 [102], and PEEK [99].
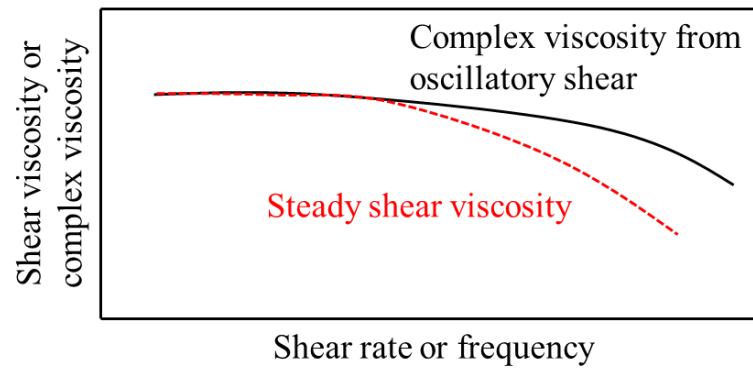

Figure 10: Schematic of the Cox-Merz rule failure to indicate the onset of oriented molecules, known to correlate with the critical shear rate for FIC.

Table 1: Summary of FIC papers highlighting polymer matrix, shear rate, degree of supercooling, and analysis techniques employed.

Polymer	Shear rate (s^{-1})	Cooling rate or Degree of supercooling	Techniques	Year	Citation
HDPE	50		Plunger flow, POM	1973	[103]
HDPE	0.1 – 3	10 K/s	Extensional rheometer, SAXS, WAXD	2016	[104]
HMWPET	0.08 – 0.16	70, 80, 90 K	Parallel plate rheology	2009	[105]
h-PBD	0.27 – 1.07	1 K/min	Linkam shear cell, SAXS, optical birefringence	2008	[74]
iPB	0.1, 1, 10	30 K	Parallel plate rheology, Linkam shear cell, POM	2009	[68]
iPP	10	38 K	Parallel plate rheology, POM, SALS	2001	[106]
iPP	0.7 – 60	48 K	Parallel plate rheology	2009	[67]
iPP		49 K	Injection molding, POM, AFM	2017	[107]
iPP		Ballistic quench, 40 K	Injection molding, POM, AFM	2019	[108]
iPP	110 – 440	41 K	Slit flow, SAXS, WAXD	2017	[109]
iPP	0.52 – 90	46 K	Parallel plate rheology, POM	2015	[69]
iPP	2.51	45 K	Cone and plate rheology, POM, AFM, WAXD	2016	[110]
iPP	10, 57, 102	46 K	Linkam shear cell, SAXS, TEM	2000	[111]
iPP	80 – 560	73 K	Slit flow rheometer, SAXS, WAXD, birefringence	2014	[112]
iPP	20	41 K, 2 K/min	Linkam shear cell, SAXS, WAXD	2011	[113]
iPP	80 – 560	41 K	Slit flow rheometer, SAXS, WAXD, POM	2013	[114]
iPP	0 – 37	36 K, 46 K	Linkam shear cell, POM, WAXD	2020	[115]
LLDPE	1.6 – 70	Up to 1,000 K/s	Parallel plate rheology, blown film extrusion, POM, FSC	2021	[116]
PA 11	0.3 – 10	45 K	Parallel plate rheology, DSC, POM, WAXS	2021	[91]
PA 66	0.01 – 10	30, 35 K	Parallel plate rheology, POM	2018	[71]
PE	125	18.5 K	Linkam shear cell, SAXS, WAXS	2006	[97]
PEEK	1 – 200	52, 55, 58 K	Parallel plate rheology	2020	[92]
PEEK	6 – 25	60 K	Cone and plate rheology, DSC	2016	[76]
PLA	0.2 – 2	56 K	Linkam shear cell, POM	2020	[96]
PLA	30	30 K/min	Linkam shear cell, WAXD, POM	2012	[117]
PLLA	0.01 – 5	41 K	Parallel plate rheology, POM, WAXS	2021	[118]
PP	20 – 50	41 – 96 K	Sandwich rheometer	2003	[75]
PPS	15, 30, 45	41 K	Linkam shear cell, AFM, DSC, POM	2008	[119]

A list of some of the FIC studies most relevant to this research is presented in Table 1. The majority of the studies addressing crystallization after shear flow have been published only in the past 20 years. Among these studies, it was common to apply a known shear history using a rotational rheometer system and monitor crystallization at low cooling rates or high crystallization temperatures. This common protocol leaves unaddressed an important gap between FIC knowledge and real process application, as the associated theories and models are driven by a narrow set of experiments that do not fully represent process shear rates and thermal environments. It is critical for the application of FIC fundamental science to also develop an understanding at high shear rates, high cooling rates, and a high degree of supercooling in addition to the spectrum of studies presented here.

3.3.2 Polyamide 66 flow-induced crystallization

The focus on controlled flow-induced crystallization experiments in the literature has primarily been centered on polyolefin systems [69,95,98,110,120–123] (see Table 1). In recent years, few PA 66 FIC experiments have been performed, while molding studies are more prevalent [71,124–128]. In the works by Seo et al., the authors found that the critical shear rate in PA 66 as determined by the Cox-Merz rule was 0.1 s^{-1}, locating the onset of orientation resulting in shear-thinning in the steady shear viscosity measurement. In further experiments, the PA 66 sample was sheared in the melt at a temperature below T_m^0, and cooled to a crystallization temperature to monitor solidification through a small oscillatory motion. A range of rates were studied at two shearing times, and the increase/onset of viscosity and modulus (G') were monitored as the crystalline phase developed. At low shear rates (<0.5 s^{-1}) the crystallization onset shifted to lower temperatures, but the primary crystallization indicated by viscosity and modulus its increased crystal fraction stayed the same, yielding the growth rate remained consistent. This implies that the nucleation is accelerated, but growth is not affected. At higher shear rates, above the critical shear rate (>0.5 s^{-1}), the samples showed nucleation acceleration as well as different growth slopes for viscosity and modulus, indicating a difference in growth rate as well. The authors determined the Avrami exponents to be ~3 and ~2 below and above the shear rate of ~0.3 s^{-1}, or work level of ~40 kPa. This changing slope indicates the growth mechanism changes from 3-dimensional in the Housman model describing Regimes I and II to 2-dimensional in Regime III [71].

Injection molding studies of PA 66 have shown that the microstructure development is dependent on the shear and cooling rates experienced during manufacturing. Spoerer et al. report that molded tensile bars display a microstructure gradient from a visible skin layer to large, spherulitic superstructures in the core, where the authors predict the cooling rate is $400 - 600$ K/s lower than in the skin. The authors use X-ray analysis to determine that the average crystallinity increased from ~25 % at the skin to ~37 % in the core, while the crystal perfection is also increased from ~53 % to ~91 % from skin to core, respectively [128].

The microstructure developed during the molding process then impacts the mechanical properties in the molded part. In PA 66 moldings, it was found that skin thickness can be manipulated based on molding conditions [125,129]. The mechanical testing of these specimens finds that a thicker skin layer, and thus lower bulk crystallinity, produces a reduction in Young's modulus and yield strength while the elongation at break is increased [129]. With a clearer understanding of microstructure development at process-relevant conditions, final part properties can be tailored for specific applications.

Though PA 66 is regarded as a difficult polymer to process due to shrinkage and warpage issues, there is little literature on the FIC behavior in this material. The controlled rheology and calorimetry experiments available in the literature have only been performed under slow cooling or at high temperatures, which does not mimic typical manufacturing processes. It is proposed that a more in-depth analysis of crystallization at high rates and high supercooling will shed additional light on the FIC kinetics that will illuminate polymer behaviors as related to plastics manufacturing.

3.4 Industrial importance of flow-induced crystallization at high supercooling and rates

Typical manufacturing processes used to produce plastic parts impose a flow to the molten polymer followed by a quench to the solid state. Injection molding is the most common manufacturing process applied to polymer materials [130]. In this process, a plasticizing unit is responsible for melting, mixing, and injecting the molten form of plastic into a mold to create designed part geometries. In this process, the mold closes, and the screw from the injection unit moves forward to inject the polymer melt into the mold. Once the mold cavity is filled, pressure is maintained by the screw, which is acting as a plunger, on the molten polymer pathway into the

cavity until the polymer solidifies. This allows for the additional molten polymer to be added to the mold cavity as the polymer shrinks during solidification, resulting in the most densely-packed part possible. While the part in the mold continues to cool, the screw is rotated back to prepare the dosage for the next shot of material. At this stage, the mold opens, and the ejection unit pushes the molded part out of the cavity [130]. Often parts are cooled as quickly as possible, ignoring the resulting microstructure, in order to maximize output, and therefore, profit. However, if repeatable and optimized physical properties are important to application, then it is critical to understand the crystal development under these process-relevant shearing and cooling conditions to tailor manufacturing efforts to optimize part performance.
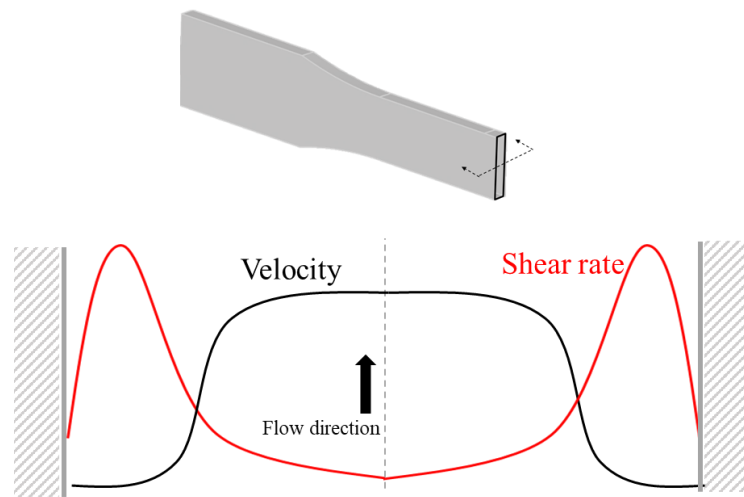
Figure 11: Velocity and shear rate profiles of the melt in an injection molded part. The schematic is representative of any channel including runner, gate, and part in an injection molded specimen. A cross section of an injection molded tensile bar is depicted to show an example of the described channel. The arrow indicates the direction of flow between two walls.

A schematic showing typical velocity and shear rate profiles within the channels of a mold are show in Figure 11. Plastics flow laminarly, where the liquid polymer flows in layers with little mixing. In the "fountain flow" effect the laminarly flowing polymer flow front moves outward to meet the channel wall. Due to the fountain flow behavior of the polymer melt, a frozen layer develops at the stationary surface. Because this frozen layer is no longer moving, the frictional forces between the frozen layer and the flowing melt causes a spike in the shear rate at the layer just inside the frozen layer. The shear rate through the cross section then reduces to a lower value in the center of the flow channel. Shearing of the polymer melt also causes shear heating up to 70 K higher than the set melt temperature depending on pressure/shear rates [131], developing local temperature distributions within a molded part and localized regions with quenched oriented

molecules. Understanding the distribution of shear and temperature within the molded part and their implications on the subsequent crystallization process is critical to the evolution of the scientific underpinnings of plastic engineering.
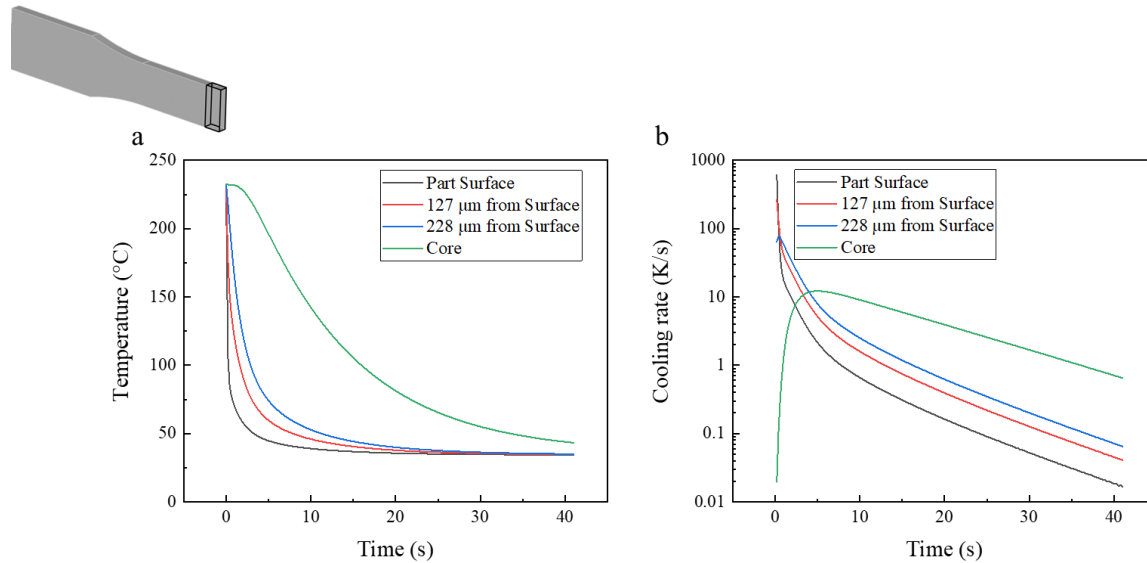

Figure 12: Temperature as a function of time in a molded tensile bar at differing distances from the skin (a) and the resulting cooling rate for the same locations (b). Example depicts cooling conditions of an ASTM D638 standard tensile specimen molded at 246 °C melt and 30 °C mold temperatures injected at 38.1 mm/s. Images adapted from [132] with permission from Wiley.

An injection molding simulation of an iPP tensile specimen revealed that typical cooling rates through the cross section of a part can reach as much as 700 K/s at the skin where the molten polymer meets the cooled mold wall [50]. The temperature distribution during cooling can be found in Figure 12a, and the resulting cooling rate as a function of time can be seen in Figure 12b at differing distances from the mold wall. The cooling rates just inside the frozen layer can be as high as 300 K/s, while the core of the part is only subjected to a maximum cooling rate of 10 K/s. The investigation of crystallization from the quiescent melt at high supercooling and high cooling rates has significantly expanded in the past 10 years, largely due to the development of the fast scanning chip calorimetry (FSC) characterization technique, where samples can be analyzed under process-relevant cooling conditions [134]. Compared to the relative enthalpy of crystallization as a function of cooling rate as shown in Figure 13, it can be expected that the quench at the mold wall will only produce 5% relative crystallinity (i.e., crystallinity normalized by the maximum observed value), while just inside the frozen layer cooling rates are expected to yield ~50% relative crystallinity, and the low cooling rates in the core of the part can produce ~90 % relative

crystallinity. However, shear rates up to 400 s^{-1} in the high shear zone of the part [132] and over 10,000 s^{-1} in the gate [130] can be expected in injection molding scenarios, though implications of shear have not yet been tested at high supercooling or high rates.
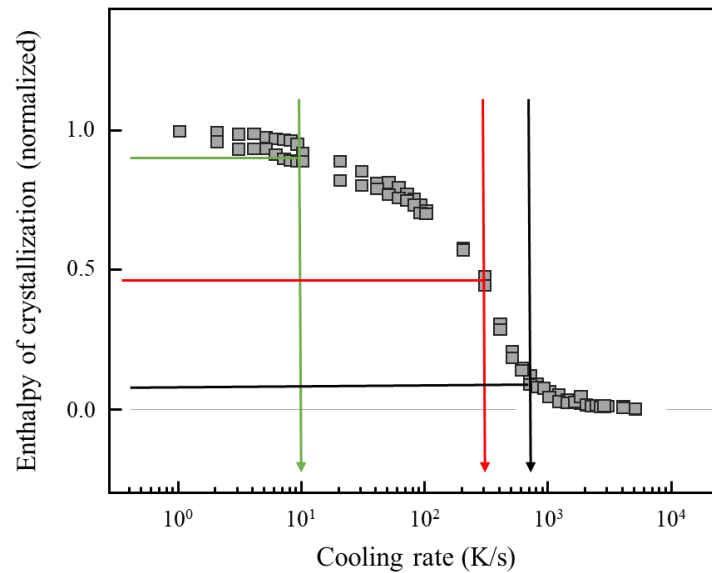

Figure 13: iPP normalized enthalpy of crystallization as a function of cooling rate. The maximum cooling rates determined from the mold filling simulation are overlayed to indicate expected crystallinity assuming linear cooling. Image adapted from [135] *with permission from Elsevier.*

Meister and Drummer [129] recently examined microstructure and mechanical properties resulting from PA 66 specimens that were molded with intentional differences in cooling profiles. Tensile specimens of differing sizes were used to manipulate the cooling rate through the part, and it was found that a smaller part thickness yielded higher skin thickness and higher nucleation density due to higher cooling rates. Resulting mechanical properties show that the larger skin thickness and higher nucleation density resulted in a lower modulus, lower yield strength, and higher elongation at break compared to that of the small skin thickness and low nucleation density [129]. This is due to the flexibility of the tie-molecules and amorphous fraction between spherulite domains. The spherulites are very rigid, and with increasing size, there is little amorphous fraction and reduced tie chains to accept the load. These results show that the molding conditions and microstructure development in the manufacturing process is critical to the mechanical performance of the molded parts. If empowered to tailor mechanical properties based on manufacturing settings, scientists can better engineer parts for specific applications. To make this effort a reality,

the implications of microstructure development at fast cooling and under shear conditions must be better understood.

4. Motivation and tasks

The crystallization of engineering polymers at process-relevant conditions (at fast cooling and under shear loading) is of the utmost importance for the next generation of advanced manufacturing crystallization prediction [136–140]. The ability to predict and tailor the microstructure of engineering thermoplastics will empower engineers and scientists to better control final part properties for sophisticated applications. In this thesis a systematic evaluation of PA 66 crystallization, focusing on process-relevant conditions including both temperature and shear, is performed.

In **Chapter 6.1**, the quiescent crystallization kinetics of PA 66 is investigated. By using the FSC as a sample preparation technique, the resultant microstructures were studied by WAXS, POM, and AFM. The crystallization kinetics at high and low supercooling and high and low cooling rates were analyzed as relevant to the injection molding process. The controlled development of sheared samples was then employed in order to evaluate flow-induced nucleation in the neat PA 66. The crystallization kinetics and resulting microstructure and morphology were analyzed. It was found that the flow-induced nuclei act in a manner similar to heterogeneous nucleators, accelerating the high-temperature crystallization regime and extending heterogeneous nucleation to lower temperatures.

In **Chapter 6.2**, a carbon nanotube (CNT) nanocomposite was created and analyzed using similar quiescent characterization techniques as described in Chapter 5.1. It is hypothesized that the nanotube, with long thread-like structure, plays a similar role as the flow-induced nuclei in accelerating crystallization. The use of CNTs has a similar impact on the crystallization kinetics displayed by sheared PA 66 materials, but their nucleating efficiency is much greater at low loading due to normal surface conformation, allowing for a more favorable nucleating surface.

Chapter 6.3 presents a comparison of the self-nucleation of the sheared samples to that of the heterogeneously nucleated nanocomposites. The nucleating efficiency is compared at similar loading levels (% of stretched chain vs wt% CNT) to further reveal relative nucleating performance. It is shown that the nucleating effect of the CNT, even at low loading, supersedes

any flow-induced crystallization effects on the polymer melt, even though orientation can be introduced at lower shear rates.

The conclusions and recommendations for future work are discussed in **Chapter 7**.

5. Experimental

5.1 Materials

The material used in this thesis was Zytel 101 from DuPont (USA). It is an un-lubricated and unmodified general-purpose molding-viscosity PA 66 grade. The number-average molar mass of this polymer is around 17 – 18 kDa [141]. The material was delivered in the form of dry pellets. The pelletized material was used for subsequent sample preparation, through parallel plate sample solidification or injection molding. Prior to melt processing, the material was dried overnight at 80 °C in a vacuum oven to minimize moisture effects.

The CNT material was sourced as a pre-compounded masterbatch with Zytel 101 (15 wt-%) from Hyperion Catalysis (MB4620-00). The CNTs provided from Hyperion Catalysis were reported to have a diameter, length, and surface area of 10 nm, 10 µm, and 200 m^2/g, respectively [142]. In order to obtain lower loading levels for the crystallization studies, the CNT masterbatch was dried (80 °C, 12 hrs), mixed with neat PA 66 pellets at the appropriate let-down ratio, and re-extruded on a Haake Rheodrive 4 twin-screw extruder equipped with a 16 mm diameter screw and a 25:1 L/D. The target loading levels for crystallization studies include 0.25, 0.5, and 1 wt-% nanoparticle. In order to have an appropriate baseline for comparison, the neat PA 66 was extruded under the same conditions as the compounded nanocomposites thereby imposing a similar temperature and shear history.

5.2 Instrumentation

Differential Scanning Calorimetry (DSC)

DSC testing was performed on a Mettler-Toledo DSC 1 with a nitrogen flow rate of 30 mL/min. All samples were prepared to approximately 5 mg mass. To accommodate controlled cooling, a Huber intracooler EK90/MT was used with the calorimeter. All measurements were taken using a 40 µL aluminum pan with a pierced lid. The equipment was calibrated by melting an Indium standard calibration pellet from Mettler-Toledo.

Fast Scanning chip Calorimetry (FSC)

FSC was used to obtain information on the time- and temperature-dependence of crystallization of PA 66. Measurements of the crystallization kinetics were made using a Flash

DSC 1 device from Mettler-Toledo. The instrument was operated in conjunction with a Huber TC100 intracooler, and the sensor/sample environment was purged with nitrogen gas using a flow rate of 35 or 60 mL/min to prevent sample degradation and icing of the equipment (flow rate was increased over time per updated equipment supplier recommendations). According to the recommendation of the instrument provider, the FSC sensors were conditioned and temperature-corrected before loading of a sample. For sample preparation, the PA 66 samples were microtomed to a 12 µm thickness using a rotary microtome with a tungsten carbide blade. These slices were then sectioned laterally to approximately a 100 µm × 100 µm square. For calorimetry analyses, typically a silicone oil (Wacker AK 60,000 [143]) was painted as a fine layer between the sensor membrane and the sample to improve thermal contact and prevent adhesion of the sample to the membrane. The FSC was also used for thermal preconditioning of samples for subsequent characterization including X-ray scattering, polarized-light optical microscopy, and atomic force microscopy. In the case of X-ray scattering and atomic force microscopy analysis, no oil was used as a barrier layer between the sensor membrane and the sample.

Isothermal crystallization analyses were conducted by heating the sample to 275 °C and holding for 0.5 s. A 2,000 K/s quench from the melt to the desired crystallization temperature was used to ensure crystallization did not occur during the cooling phase [22]. The sample was held at the crystallization temperature, T_c, for up to 15 s to allow for complete crystallization. A quench, again at 2,000 K/s, to -60 °C was used to allow for analysis in a subsequent heating scan that would provide T_g and T_m information. For samples that required subsequent analysis after specific temperature crystallization, the sample was removed from the FSC prior to the heating scan, and subjected to XRD, AFM, or POM analysis. A schematic of this isothermal crystallization method is displayed in Figure 14a. For non-isothermal crystallization experiments, the sample was taken to 275 °C and held for 0.5 s, followed by a designated linear cooling profile to -60 °C at rates ranging from 1 to 5,000 K/s. The sample was held at -60 °C for 0.5 s, after which it was subjected to a heating scan at 500 K/s. For determination of enthalpy of crystallization as a function of cooling rate, the subsequent melting enthalpy minus any enthalpy of cold crystallization on heating was used to calculate the crystal fraction developed in the previous cooling segment. It has been reported that integration of the subsequent melting endotherm is more precise than integration of the broad exothermic crystallization peak on cooling [22].
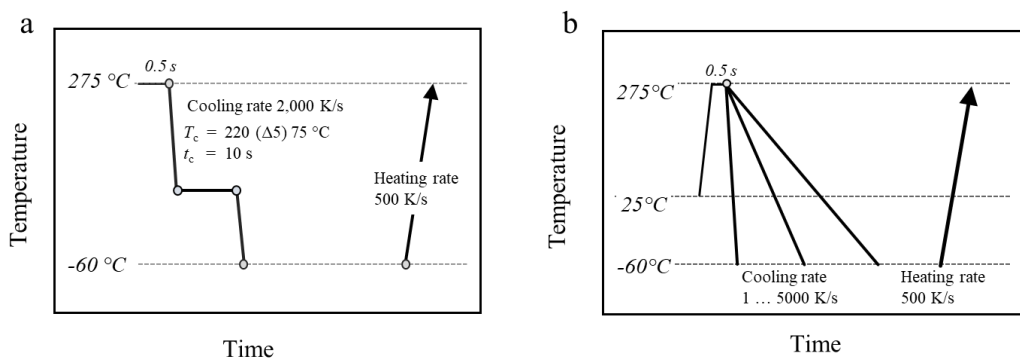
Figure 14: FSC isothermal crystallization experiment (a) and non-isothermal crystallization experiment (b) methods.

Wide Angle X-ray Scattering (WAXS)

WAXS measurements of the preconditioned FSC samples were performed using either a Rigaku DMAX-Rapid II or XENOCS Xeuss 2.0 diffractometer equipped with a 0.154 nm Cu X-ray tube and a graphite monochromator. Analyses were completed in transmission mode, and the scattered X-rays were recorded using a curved image plate coated with photo-stimulable phosphor $(BaF(Br,I):Eu^{2+})$. The beam diameter and exposure time were 300 µm and 600 s, respectively. The 2D diffractograms were azimuthally integrated to yield the intensity distribution as a function of the scattering angle 2θ, followed by subtraction of an XRD curve obtained on an empty FSC chip. Data were analyzed using Jade 2010 software.

Polarized Optical Microscopy (POM)

Samples were imaged using POM employing a Leica MD750P microscope and DMC2900 camera. Prior to FSC analysis of sheared samples, the microtomed cross sections of the disc were inspected using POM in transmission mode for flow-induced structures. Careful cutting of the samples under polarized light allowed for the selection of samples with known shish-kebab content. The thin section was then transferred to the FSC chip for calorimetric analysis. Between FSC analyses for specific experiments, the sensor containing the sample was moved to the microscope for microstructure evaluation. Samples studied using POM on the FSC chip were imaged in reflection mode between crossed polarizers.

Atomic Force Microscopy (AFM)

AFM measurements were performed using a Bruker Dimension Icon. In these experiments, samples were fused to the FSC membrane and crystallized isothermally at 70 and 200 °C on

separate chips. For the AFM probe to contact the sample, it was necessary to remove the sensor membrane containing the sample from the ceramic chip due to geometric constraints. To do this, double sided tape was placed on an AFM stub and the sensor membrane was adhered to the adhesive. A pin was then used to fracture the membrane from the ceramic chip so that the chip could be removed, and the sample/membrane was left on the AFM stub. PeakForce tapping imaging mode was used with a ScanAsyst Air Probe (0.4 N/m spring constant). Image analysis was done using Nanoscope Analysis software.

Rotational rheology

Parallel plate rheology was used to evaluate the viscosity as a function of angular frequency in the neat PA 66 at differing temperatures. For this experiment, 25 mm cone and plate fixtures at 1 mm gap on an Anton Paar MCR 702 MultiDrive rheometer using an electrical temperature device (ETD 400) oven and nitrogen purge were employed. Measurements were performed from high to low angular frequencies ranging from 100 to 0.1 rad/s and temperatures from 265 to 310 °C. Cone and plate fixtures with a 25 mm diameter were also used to analyze the Cox-Merz behavior of both the neat and CNT nanocomposite systems. In these experiments, the dried (80 °C, overnight) pelletized samples were loaded at 270 °C, where a pre-shear was applied to aggregate the pellets and remove any air bubbles. The temperature was then increased to 300 °C for 1 min to erase any thermal or shear history. The sample was cooled to 270 °C at 10 K/min, where the Cox-Merz analysis was initiated. In this experiment, the sample was first analyzed under oscillatory shear from high to low angular frequencies (100 to 0.1 rad/s) followed by a steady shear experiment from low to high shear rates (0.01 to 100 s^{-1}). The point where the steady shear viscosity diverges from the oscillatory shear viscosity indicates the point at which steady shear can develop orientation in the polymer matrix.

For all rheology experiments using cone and plate and parallel plate fixtures, the nitrogen flow rate was held constant at 100 L/hr. The gap size between upper and lower tool fixtures was selected based on the ISO 6721-10 standard, where a ratio of $2r/h$ between 10 and 50, r being the radius and h being the gap height, is recommended [144].

Flow-induced crystallization kinetics

The Anton Paar MCR702 MultiDrive rheometer was also used to measure crystal development in the neat and CNT nanocomposite samples. For these experiments, sample discs were prepared to load onto the 8 mm cone and plate fixtures to reduce variation caused by loading pellets. Pellets were dried overnight at 80 °C and pressed to a 1 mm film using a Carver hot press at 280 °C. The films were then removed from the press and quenched in a water bath. A 6 mm hole cutter was used to drill circular discs from the films. The discs were then dried at 80 °C overnight and stored in a heat-sealed aluminum foil bag to prevent moisture uptake. For the crystallization experiments, the discs were loaded onto the 8 mm cone and plate fixture at 270 °C and pressed to 0.7 mm sample height. By pre-cutting the disc to known dimensions, the hood did not need to be lifted to trim the sample and this is believed to reduce degradation from oxygen exposure. The samples were then heated to 300 °C for 1 min to erase thermal and shear history, then cooled at 10 K/min to 270 °C for pre-determined shear profiling. Shear rates and times were altered to obtain a range of work levels. After shearing, the sample was cooled at 10 K/min to the crystallization temperature of 250 °C, where crystallization was monitored by a small-amplitude oscillatory shear (SAOS) step of 1 rad/s and a strain amplitude of 5 %.

Sample preparation to obtain solidified discs of known shear history

A parallel plate rheometer was then used to create solidified samples with controlled shear history. Fabrication employed an ARES-G2 rheometer (TA instruments) equipped with 25 mm diameter stainless steel parallel plate fixtures. Before loading the PA 66 pellets on the parallel plate, polyimide Kapton tape (DuPont, 25 μm thickness) was attached on both top and bottom plates to facilitate easy removal of the sheared disc after solidification for subsequent microscopic and calorimetric analysis. Repeat measurements with and without the use of Kapton tape showed the tape presented no effect on the shearing step in these experiments. The geometry held a 1.2 mm gap during the entire fabrication.

A time-temperature protocol that employed both rotational and oscillatory shear was developed for the sheared-disc fabrication as depicted in Figure 15. First, PA 66 pellets, after being dried at 80 °C in a vacuum oven overnight, were melted on 25 mm parallel plate fixtures at 270 ℃ for 1 minute. A constant shear rate of 0.5 s^{-1} was then applied to the molten pellets for 5 minutes to aggregate the pellets without air bubbles. To erase the thermal history, the temperature of the

polymer melt was increased to 300 ºC for 1 min. After this annealing step, the melt was cooled (10 K/min) to the shearing temperature of 270 ºC, and a designated shear rate at the perimeter (100 s^{-1}) and shearing time (0.81, 6.5, and 25.9 s, for the three different discs, respectively) were imposed on the melt to achieve the three levels of specific work of interest. After shearing, the melt was cooled at 10 K/min to 200 ºC and held for 5 min, which is sufficient time to ensure complete crystallization. The sample was then cooled (10 K/min) to room temperature and the solidified discs removed from the parallel plate fixture for successive studies. A fourth "zero shear" sample was prepared using an identical protocol, but instead of shearing at 270 °C the material was simply held in the melt for 25.9 s at 270 °C, and then solidified under conditions identical to the corresponding sheared samples.
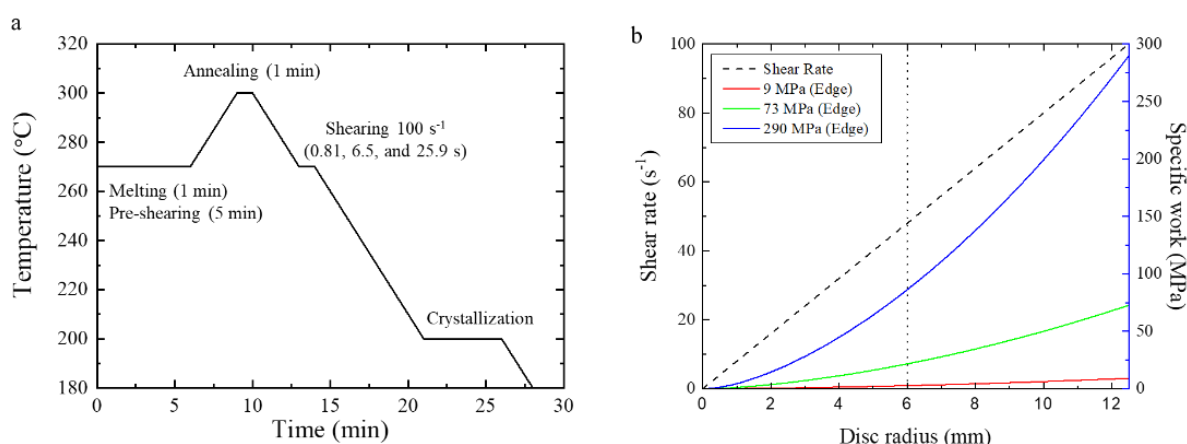
Figure 15: Parallel plate rheology sample preparation method displaying the temperature profile (a) and the shear rate and specific work of flow as a function of disc radius (b). It is shown that all discs were created at the same temperature profile. The shear rate at the edge of the disc was also set constant at 100 s^{-1}. The three sample discs were created using differing shearing time, which alters the final specific work. Reprinted [145] with permission from https://doi.org/10.1021/acs.macromol.8b00195. Copyright 2018 American Chemical Society.

For each disc prepared, there is a distribution of the shear rate and specific work across the radius of the parallel plate disc as shown in Figure 15b. The shear rate is determined by the velocity of the rotation and the distance between the plates, resulting in a linear increase in shear rate from the radius to the edge. Theoretically, the shear rate at the center of the disc is zero. However, POM of this center location consistently reveals a modicum of orientation influencing material solidification, perhaps due to a drag force present in the melt, likely modifying the crystallization process relative to a truly unsheared sample. The specific work for each of the discs is also plotted in Figure 15b as a function of radius from the center of the disc, spanning the cross section. The

specific work is dependent on the shear stress per equation 2, using a steady state shear viscosity measurement of 1400 Pa·s obtained via cone and plate rheology measurements. A model of the formation of the flow-induced structures in the parallel plate sample is displayed in Figure 16. It is shown in the leftmost image that the initial material, or material flowing under a low shear, displays no orientation (a). If there is enough shearing and time available, the molecules can orient (b). As previously discussed, the shearing rate and specific work in the parallel plate specimen is a function of the distance from the center of the disc, demonstrated by non-oriented molecules in the center of the disc and orientation developed outside of a critical radius (c). After the cessation of flow (d), some weak oriented molecules can relax and return to the isotropic state, while some of the molecules which were exposed to high work remain elongated through solidification, unable to return to an isotropic melt [74].
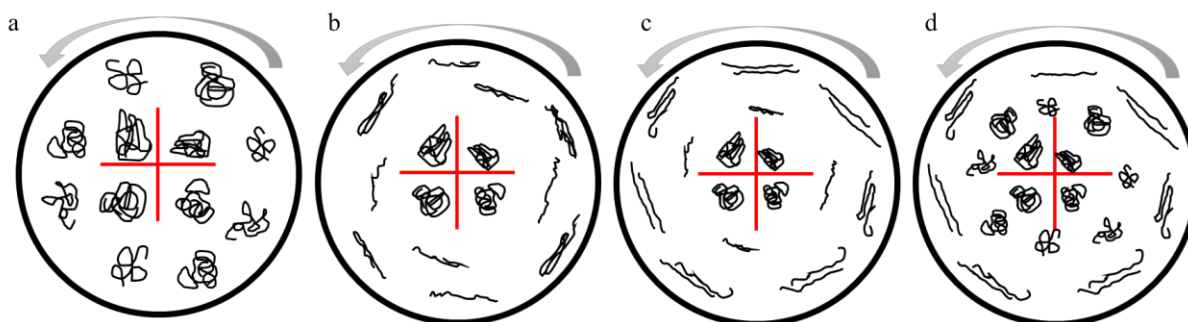
Figure 16: Proposed model of formation of flow-induced structures in parallel plate samples during shear. If the model depicts shearing at a constant rate over time, as the experiments here, the model depicts initial stage or weak shear (a), intermediate before precursors form (b), final stage (c), and after shearing where some polymer chains relax (d). After these samples have been created in the rheometer, they were cooled and salvaged for subsequent analysis.

Transmission Electron Microscopy (TEM)

TEM was used to analyze the CNT dispersion after the masterbatch was diluted. Imaging was performed on a FEI Talos at 200 kV. Prior to imaging, pelletized samples were ultra microtomed to 100 nm thickness using a Leica EM UC6 ultramicrotome and adhered to carbon support.

Size Exclusion Chromatography (SEC)

Molecular weight distribution was analyzed by a Shimadzu LC-20AD SEC. 100 mg of PA 66 was dissolved overnight in 1 mL of solution containing 1,1,1,3,3,3-hexafluoro-2-propanol (HFIP)

and 5 mM sodium trifluoroacetate (NaTFA). 20 mL of solution was injected using a Millex syringe with a 0.45 μm filter at a flow rate of 0.2 mL/min at 40 °C. The molecular weight distribution was determined relative to the poly (methyl methacrylate) (PMMA) standard. Molar mass was calculated using $K_{PMMA} = 0.115 \times 10^{-3}$, $a_{PMMA} = 0.746$, $K_{PA\ 66} = 1.236 \times 10^{-3}$, and $a_{PA\ 66} = 0.673$, $M_w = 22,700$ g/mol, and $M_n = 11,300$ g/mol per Mark-Houwink parameters [146].

6. Results and Discussion

6.1 Polyamide 66 crystallization

6.1.1 Quiescent crystallization

Quiescent crystallization kinetics of the neat PA 66 was first studied to obtain baseline and foundational information about crystallization of this engineering polymer. In isothermal crystallization experiments, the sample was heated to 300 °C, briefly held at this temperature and then quenched at 2000 K/s to the desired crystallization temperature. The sample was held at the crystallization temperature for up to 15 s, after which it was quenched to a temperature below T_g. The same sample was then cycled back to the melt, to repeat the analysis at temperatures ranging from near the melting temperature (220 °C) to near T_g (75 °C). At the end of the temperature cycle, a repeat of the first measurement was conducted to confirm repeatability of the measurement and to ensure that no polymer degradation had occurred. Figure 17 displays the raw heat flow data collected at each crystallization temperature between 220 °C (front) and 75 °C (back). The exothermal peak indicates crystallization over time. Because the crystallization exothermic peak show noticeable symmetry, the peak time of crystallization was analyzed here, selected as the peak of the curve. The crystallization half time of Zytel 101 (PA 66) displays a bimodal temperature dependence, which is in agreement with a different neat PA 66 grade studied previously [22]. Without the use of FSC, isothermal crystallization of PA 66 could only be studied at high temperatures by melt crystallization, or low temperatures after a quench to the amorphous state; the mid-temperature region could not be analyzed [58,147]. Similar to other polymers, this grade shows a characteristic increased crystallization halftime, or decrease in crystallization rate, at temperatures close to the T_g and T_m with a decrease in crystallization time in the mid-temperature region. There are local minima in crystallization time at 160 and 115 °C, and a local minimum in crystallization rate at 130 °C. Bimodal peak time of crystallization behavior has also been shown to occur in other polymers as the nucleation mechanism transitions from heterogeneous at low supercooling to homogeneous at high supercooling [5,134,148].
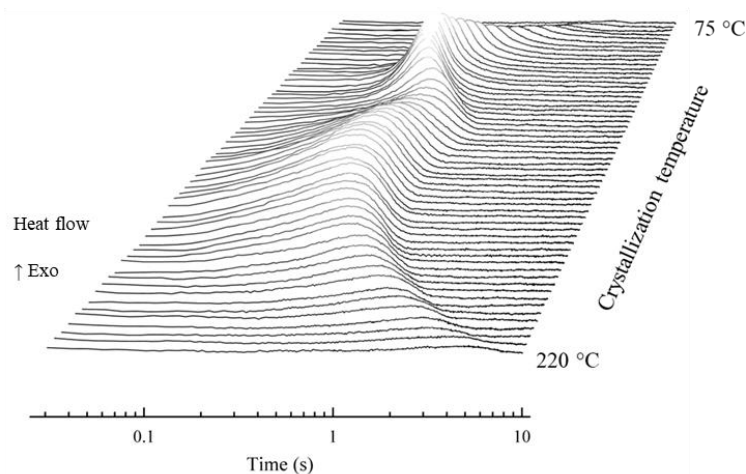
Figure 17: Heat flow as a function of time during isothermal crystallization of neat PA 66. Temperatures ranging between 220 °C (front) and 75 °C (back) with each curve representing a 2.5 K temperature decrement. Image adapted from [149] with permission from Elsevier.

From these exothermic traces, the peak time of crystallization was evaluated, and resultant data are plotted as a function of temperature in Figure 18. Multiple samples were tested by varying sample size and FSC instrument (white fill vs gray fill) to analyze the effect of sample mass and instrument variation. Good agreement is evident with samples tested on differing instruments and at sample weights ranging from 50 ng to 1 µg. The bimodal crystallization behavior is expected to be a result of a switch in nucleation mechanism from heterogeneous at high temperature to homogeneous at low temperature. The heterogeneous and homogeneous crystallization regimes show local maxima in crystallization rate at 160 °C and 115 °C, respectively, where peak time of crystallization reaches minima of 0.3 s in both regimes. The transition from heterogeneous to homogeneous nucleation occurs at the local crystallization rate minimum of 130 °C, which is in agreement with additional isothermal crystallization studies of PA 66 grades with differing molar mass [150]. While it is speculated that the bi-modal temperature dependence of crystallization is due to a change in nucleation mechanism demonstrated in other polymer systems [5,23,148,151–154], this has yet to be proven for PA 66. For this reason, FSC was used as a sample preparation tool to further evaluate the structure development by XRD, POM, and AFM.
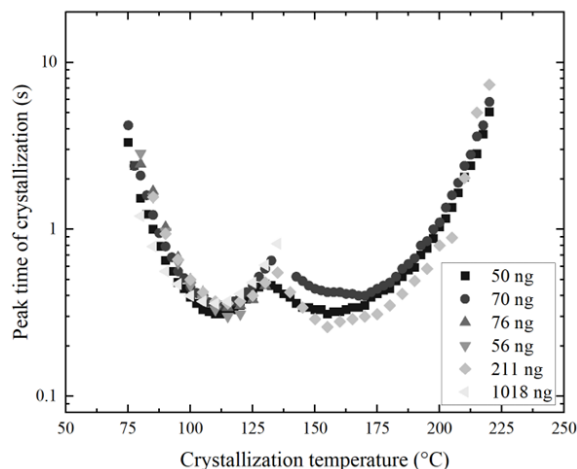
Figure 18: Peak-time of crystallization of PA 66 as a function of the crystallization temperature spanning T_g to T_m. Sample sizes of 50 ng to 1 µg and two FSC instruments (open/filled symbols) were studied to analyze reproducibility of the measurements. Image adapted from [149]*, with permission from Elsevier.*

Crystal polymorphism as a function of crystallization temperature was studied using FSC as a sample preparation tool to obtain samples with controlled crystallization at high supercooling. To achieve strong WAXS peaks with high signal-to-noise ratio, samples with slightly larger mass than typically used in FSC measurements were prepared (200 µm × 200 µm × 20 µm). To accommodate the larger sample mass, samples were cooled from the 300 ℃ melt at a rate of 800 K/s (instead of the previously applied 2,000 K/s) to the desired crystallization temperature. Crystallization temperatures ranging from 70 to 230 °C were analyzed at 10 K intervals, and the sample was held at each temperature for 200 s to ensure complete crystallization. After the crystallization at the desired temperature was complete, the sample was quenched to -60 °C, the instrument was brought to room temperature, the FSC sensor was removed and placed into WAXS beam line, and the WAXS measurement was performed. After WAXS collection was complete, the same sample/chip was placed back into the FSC for re-conditioning at the next crystallization temperature. A WAXS measurement on an amorphous sample was performed by heating the sample to 300 °C and quenching from the melt to -60 °C at 2,000 K/s. A baseline subtraction was also performed by scanning an empty FSC sensor.
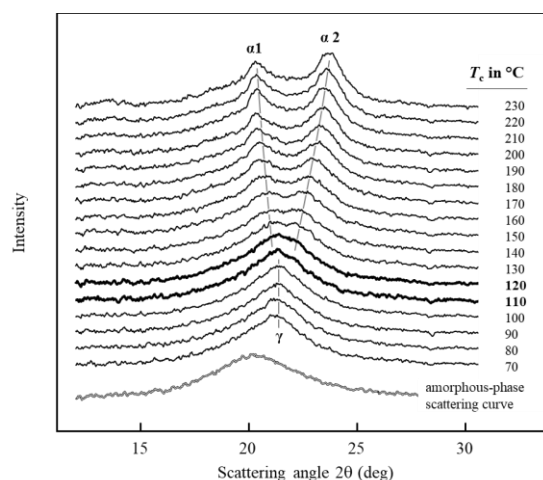
Figure 19: WAXS patterns of amorphous (bottom) and isothermally crystallized PA 66 (Zytel 101) at temperatures between 70 and 230 °C. Image adapted from [149]*, with permission from Elsevier.*

WAXS patterns for the isothermal crystallization experiment are displayed in Figure 19. At high temperatures, or low supercooling, two peaks developed at 20.3° and 23.7° scattering angle 2θ and are labeled $\alpha1$ and $\alpha2$. These peaks are associated with the (100) and (010)/(110) lattice planes of the α-structure's triclinic unit cell [26,155]. With decreasing crystallization temperature, the $\alpha1$ and $\alpha2$ peaks converge to a single peak, indicating similar d-spacing [156]. The change in crystal dimensions is gradual with decreasing temperature, suggesting the unit cell of PA 66 undergoes a continuous modification with decreasing temperature. At temperatures lower than 120 °C, only the pseudohexagonal γ-mesophase is observed, indicated by the 100 peak at about 21.4 ° [27]. The WAXS analysis of the amorphous sample shows an amorphous halo at 20.2°. This differentiation from the signals obtained between 70 and 110 °C confirms the formation of a second crystal phase.

To evaluate the superstructure development as a function of temperature, FSC was again used as a sample preparation tool for both POM and AFM analyses. Similar to the studies conducted for XRD, the sample was prepared in the FSC by crystallizing under specific conditions, and then the chip was removed for subsequent analysis. For POM imaging, the samples were conditioned isothermally at specific crystallization temperatures, ranging from 70 to 200 °C in 10 K increments. The chip was then removed from the FSC and imaged by optical microscopy in reflection mode with low transmission lighting. Figure 20 displays the POM images for all of the temperatures studied here with larger representative images provided at 70 °C and 160 °C to highlight the differences in superstructure development. It is shown in the full spectrum of

crystallization temperatures that when crystallized between 120 and 200 °C, the well-documented Maltese cross pattern is observed. In samples crystallized at temperatures over 130 °C, individual spherulites can be identified. With decreasing crystallization temperature, the nucleation density is increased, and below 130 °C, individual spherulites cannot be identified, but birefringence on spatially resolved entities still suggests scattering of the light from spherulitic structures. However, at temperatures lower than 120 °C, no birefringence is observed, indicating the size of crystal superstructures are less than the maximum resolution of the microscope.
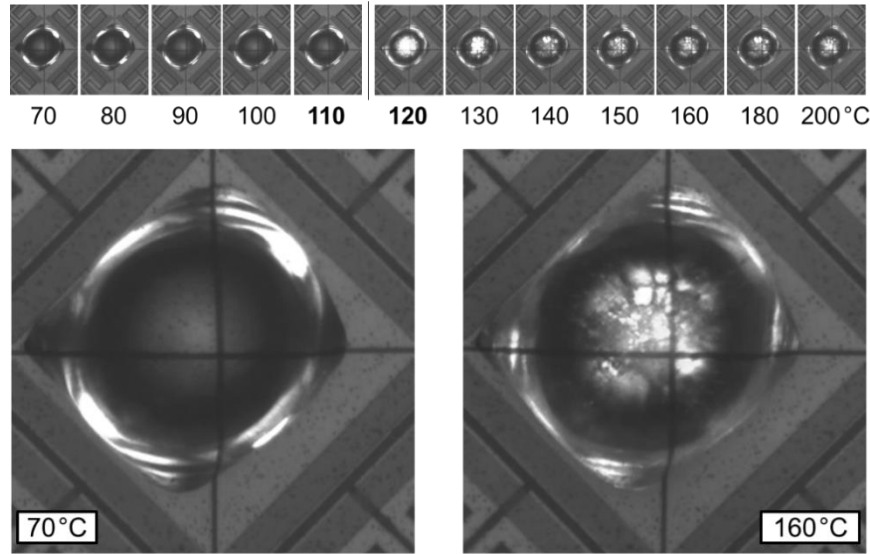
Figure 20: POM images of PA 66 isothermally melt-crystallized at temperatures spanning 70 to 200 °C in an FSC (top row). The large images highlight samples crystallized at 70 (left) and 160 °C (right). Image adapted from [149] with permission from Elsevier.

The microstructure development of isothermally crystallized PA 66 samples was then studied using AFM. In these experiments, samples were fused to the FSC membrane and crystallized isothermally at 70 and 200 °C on separate chips. AFM images in height- (top) and error-mode (bottom) of the PA 66 samples crystallized at 70 (left) and 200 °C (right) are shown in Figure 21. Inset images at 200 °C are included to show lower magnification of the surface. Multiple samples were prepared to validate this technique. At 200 °C, spherulitic growth with low nucleation density is observed. Radial growth of lamellae from a center point can be identified, which corroborates the hypothesis of the occurrence of heterogeneous nucleation at low supercooling. At high supercooling, as studied by crystallization at 70 °C, very high nucleation density is observed, which restricts crystal growth. Particle-like domains on the scale of only $10 - 20$ nm are identified, and the nodules display independent growth while not forming a superstructure. The resolution for viewing structures under white light by optical microscopy requires a minimum artifact size of approximately 1 μm [3], which agrees with the findings of the POM analysis where structures were not visible at high levels of supercooling. The spherulitic structures formed at high temperature are related to the PA 66 α-structure, while the nodular growth at high supercooling is related to the γ-mesophase. This optical microscopy analysis is in agreement with the many PA 66 injection molding studies showing superstructure size gradient as a function of distance from the skin,

always concluded to be related to changes in cooling rate, and therefore, crystallization temperature [125,128,129].
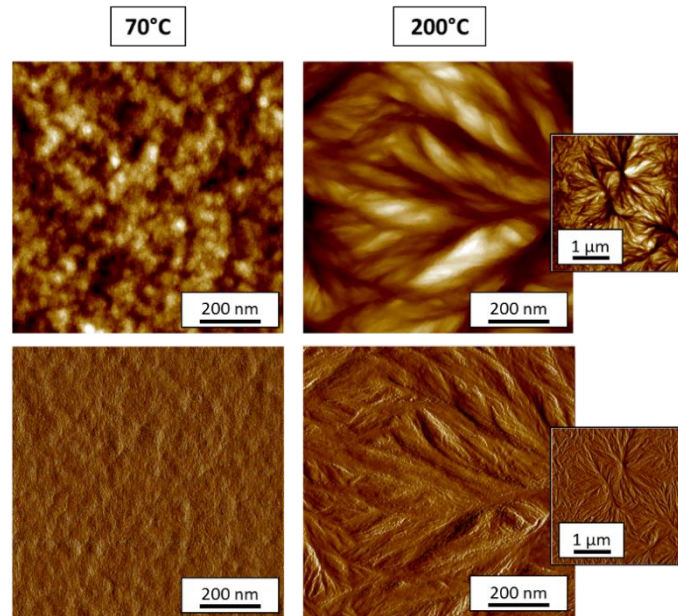

Figure 21: AFM images of PA 66 crystallized at 70 °C (left) and 200 °C (right) by FSC. Top row images were collected in height-mode and bottom row images were collected in height error mode by AFM. Insert images at 200 °C are included to show the larger, spherulitic structures at lower magnification. Image adapted from [149] with permission from Elsevier.

Non-isothermal crystallization analysis of the PA 66 was also completed to establish an understanding of the effects of cooling considerations on microstructure development. In non-isothermal crystallization experiments, an FSC sample was heated to the melt (300 °C), where it was then cooled at a constant rate to -60 °C. This thermal cycle was repeated until all desired cooling rates were analyzed, ranging from 1 to 4,000 K/s. The subsequent heating curves, showing heat flow as a function of temperature are displayed in Figure 22. In the analysis heating scan, a constant heating rate of 500 K/s was used to analyze the crystal fraction developed during prior cooling. The crystallization signal in the neat PA 66 is very weak and can be difficult to distinguish, so crystallization was analyzed by subtracting the enthalpy of cold crystallization from that of the melting peak. The heating scans after 1 K/s (red) and 4,000 K/s (blue) cooling are highlighted in Figure 22. It is evident that at high cooling rates, where crystal development is not possible during the cooling cycle, a large cold crystallization peak is observed that equals the energy of the subsequent melting step. When cold crystallization is equal to that of the melting peak, it indicates that no crystal fraction was developed during the cooling step. As the cooling rate is decreased, the cold crystallization peak area decreases, indicating a larger crystallization

49

fraction was formed during cooling. At the slowest cooling rate studied by FSC (1 K/s) highlighted by the red curve, no cold crystallization is observed, indicating that the sample fully crystallized during the cooling scan.
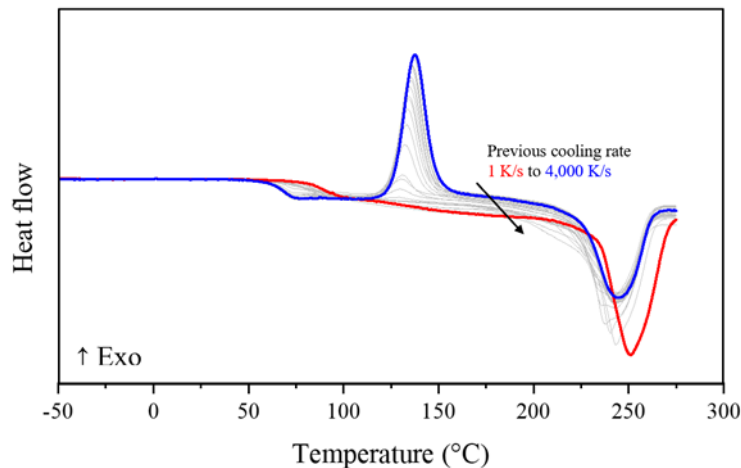

Figure 22: Heating curves at 500 K/s after cooling at rates ranging from 1 to 4,000 K/s. Red line indicates heating after slowest cooling rate (1 K/s) and blue line indicates heating trace after fastest cooling rate (4,000 K/s).

The normalized area as a function of cooling rate is displayed in Figure 23. It is shown that at low cooling rates up to approximately 100 K/s, there is a slight decrease in relative crystallinity with increasing cooling rate. Between 100 K/s and 1,000 K/s, there is a sharp decline in crystal fraction developed during cooling, and at rates over 1,000 K/s, the sample is fully vitrified, forming an amorphous material. The non-isothermal findings are in agreement with those reported for PA 66 grade Zytel 101L [22], which is the same polymer as the Zytel 101 used for these studies, (17,000 g/mol molar mass) but with lubricant added to aid processing. Studies were carried out to assess the impact of the lubricant additive, which was shown not to affect the crystallization process compared to the Zytel 101 studied here. In PA 66 with ultra-low viscosity (8,000 g/mol molar mass), non-isothermal studies at these process-relevant cooling rates showed that the critical cooling rate needed to suppress crystallization completely was increased to 5,000 K/s [150]. In comparing this experimental data to other PA 66 grades in the literature, it is apparent that additive packages and molecular weight distributions are critical factors in affecting the crystallization kinetics of PA 66.
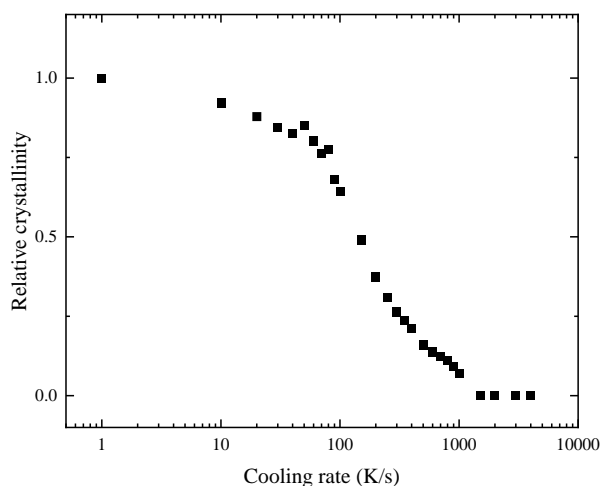
Figure 23: Relative crystallinity as a function of cooling rate for neat PA 66.

These experimental results shed new light on the crystal and superstructure development as a function of rate and temperature in neat PA 66. Critical calorimetric information providing crystallization time and fraction as a function of temperature and rate, respectively, gives new insights to engineering process control that will allow scientists to more precisely tune the specific part-forming process to yield an intentional polymorph, superstructure, and crystalline content. Pairing FSC as a sample preparation tool with other analytical techniques of WAXD, POM, and AFM, the crystal polymorphism and microstructure development were more precisely identified for PA 66 in a broader temperature spectrum than previously reported [149].

6.1.2 Flow-induced crystallization

To further understand the crystallization kinetics of the neat system, the onset time of crystallization as a function of shear rate and time was evaluated. The evolution of complex viscosity with increasing crystal fraction at differing shear rates and time intervals is plotted in Figure 24. The onset of crystallization was determined by selecting the time step where 10% conversion to crystallization is complete, where the specific conversion parameter was selected to assure that crystallization has unambiguously initiated. The shear work of flow for each analysis was calculated using equation 2, where the viscosity from the steady shear step was used along with the input shear rate and time. It can be seen that with increasing shear work of flow, the onset time of crystallization is reduced. If the onset of crystallization is plotted as a function of the specific work of flow, as in Figure 25, it can be seen that the threshold to initiate FIC, or the critical work level, is approximately 0.1 MPa in the neat PA 66 system.
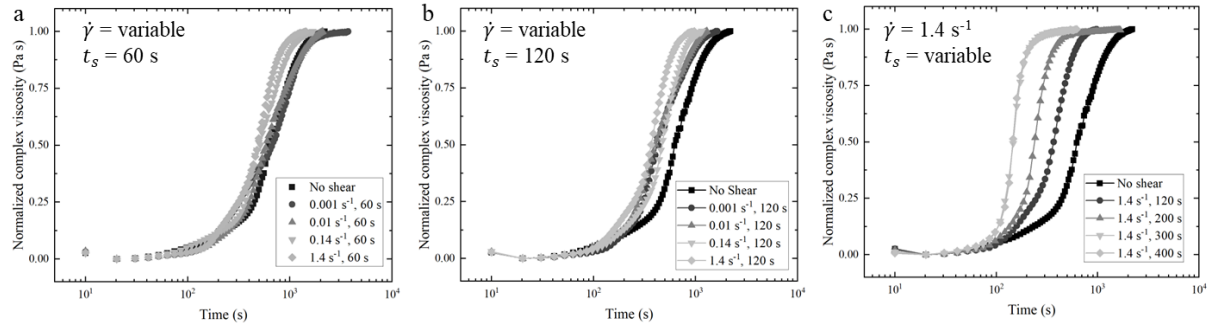
Figure 24: Neat PA 66 crystallization kinetics from cone and plate rheometer after known shearing conditions. Graph (a)shows change in shear rate with consistent shear time of 60 s. Graph (b) shows change in shear rate with consistent shear time of 60 s. Graph (c) shows consistent shear rate with changing shearing time. Reprinted [157] with permission from https://doi.org/10.1002/marc.202200418. Copyright 2022 from Wiley.

This finding agrees with results from that found in the neat PA 66 system of Ascend Vydyne 21SPC studied recently by Seo (2018) [71], where the W_c was found to be 0.04 MPa. The Vydyne 21SPC has similar M_n (11,100 g/mol), M_w (22,300 g/mol), and polydispersity index (2.0) [71] to the Zytel 101 used in this thesis.
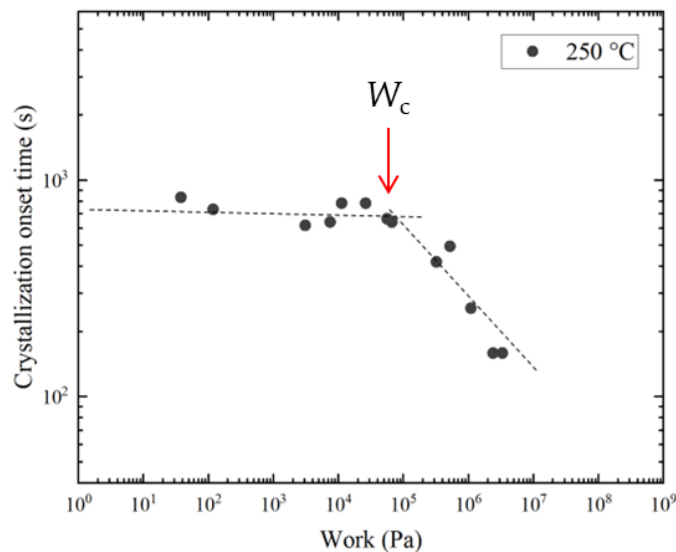

Figure 25: Crystallization onset time as a function of specific work in neat PA 66 using 8 mm cone and plate fixtures.

To investigate the crystallization in the neat PA 66 system after flow was imposed, rotational rheology was applied as a sample preparation tool. The melt was subjected to specific amounts of shear and time, as displayed in Figure 15b. In these experiments, the shear rate was held constant at 100 s^{-1} at the disc edge, and shearing time was increased to alter the total amount of shear work

applied. Shear times of 0.81, 6.5, and 25.9 s yielded specific work levels of 9, 73, and 290 MPa at the disc edge. Samples were taken for subsequent analysis at the measured location of 6 mm from the center of the disc in order to avoid using material that may have experienced edge fracture. The work level associated with this distance is 3, 22, and 86 MPa for each disc, respectively. A disc fabricated with the same thermal history but without any shear was also created to use as a baseline with a work level of 0. The disc was sectioned to produce a wedge so that samples could be taken at a specific distance from the disc center, as shown in Figure 26.
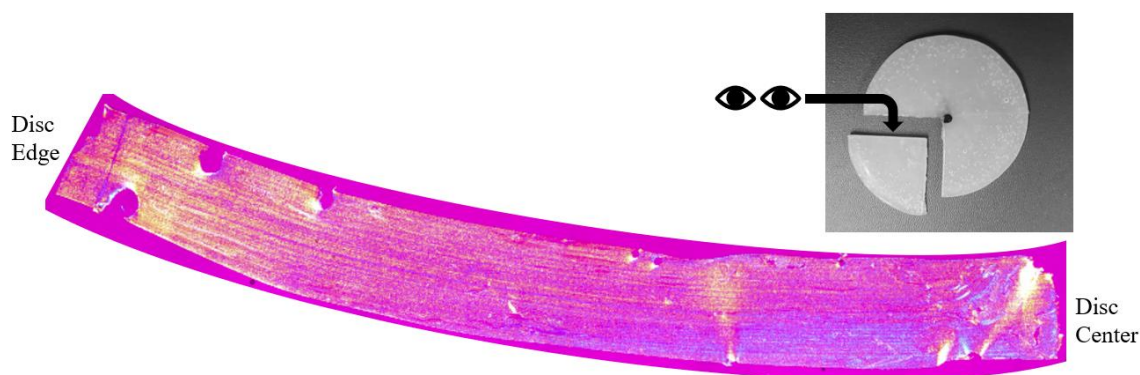
Figure 26: Example of microtomed section from solidified disc from center to edge. The dimensions of this section are 12.5 mm in length and 1 mm in thickness. "Lines" displayed at low magnification as shown here may either be drag marks from the microtome blade or shish-kebab structures. Higher magnification and inspection are necessary to identify FIC structures.

POM images taken from the disc at mid-range of flow (6 mm from disc center) and the disc edge are shown in Figure 27 for the sample sheared at 290 MPa at disc edge. It is evident that the edge fracture region produces many shish-kebab structures that appear to be flexible, in that they are not completely linear and can appear both parallel and perpendicular to the flow direction. It is presumed that a perturbance to the flow can cause the shish structures to mis-align relative to the shear field [158,159], but their stability in the melt still allows for nucleation and crystal growth after the cessation of shear. However, where the flow is more constrained in the mid-region of the disc, the shish-kebabs maintain a more linear structure, as shown in the image taken from approximately 6 mm from the center of the disc. The shish-kebabs at the disc edge are more random and unpredictable than expected, so samples selected for subsequent FSC experiments were harvested intentionally closer to the center of the disc, where there is more confinement and edge fracture is not an issue. The geometry of the shish-kebabs resulting from this shear step is also notable, as some shish are qualitatively thicker than others, indicating differences in the size of the stretched bundles of molecules that produce the shish. The location of the shish also affects

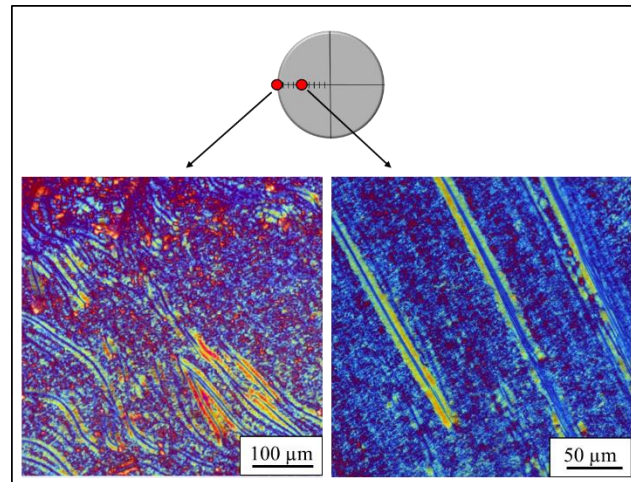the growth of the kebab structure, as in areas of shish-rich regions, impingement of kebab growth is observed.

Figure 27: Shish-kebab at edge and center of disc radius (~6 mm) in 290 MPa sample.

The resulting superstructure as a function of disc radius observed in these experiments, and also confirmed in other polymer systems including PLA [90] and iPP [67,84,160] is summarized in a schematic displayed in Figure 28. With the addition of shear, if the level is under the W_c to induce flow-induced precursors, subsequent crystallization is not affected, developing only spheruliticalyy arranged crystals (a). When enough shear is present, the formation of row nuclei, and even shish-kebabs can be observed depending on the amount of work, as displayed in (b) and (c). Because the shear rate increases linearly as a function of radius when using parallel plate fixtures, more shear work is applied as a function of the radius also. For this reason, different microstructures can develop across the radius of the sheared disc.
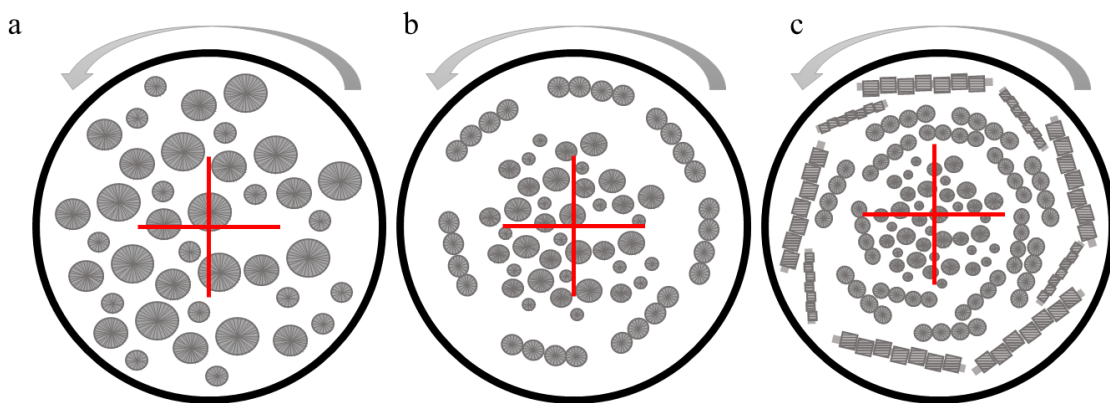

Figure 28: Schematic of resulting microstructure after intentional flow in rotational rheometer at (a) $W<W_c$ (Regime 1), (b) $W>W_c$ (Regime II), and (c) $W>W_c$ (Regime III).

54

Figure 29 shows the POM images of samples cut 6 mm from the center of each disc with differing shear time. Shish-kebab structures are clearly visible in the sheared samples, and are absent in the unsheared disc. It is notable that the shish structures are observed in both the flow direction (e) and perpendicular to flow (a-b). Observation of shish morphology perpendicular to the flow direction has been reported in other polymers, and is attributed to perturbations to the flow introducing a rotation to the shish direction, a behavior coined "log-rolling" [159,161,162]. The inset images show how samples were sectioned for subsequent FSC experiments. Samples were cut under polarized light in order to capture an area known to contain at least one shish-kebab structure for the FSC experiment. Stretched core structures identified through POM ranged from 0.05 to 5 µm in diameter depending on the size of the visibly oriented bundles. For reference, true UHMWPE shish were identified by SEM and measured to be 10 to few tens of nm in diameter and longer than 10 µm in length, while kebab diameter averaged approximately 300 – 400 nm [163,164]. The length of the PA 66 shish identified by POM ranged from 8.85 µm to 1.3 mm in the shortest to longest shish, respectively. In comparison of the structures identified here to those reported in the literature, it is concluded the shish and kebab comprise the central core region visible by optical microscopy and further transcrystallization is visualized off its surface.
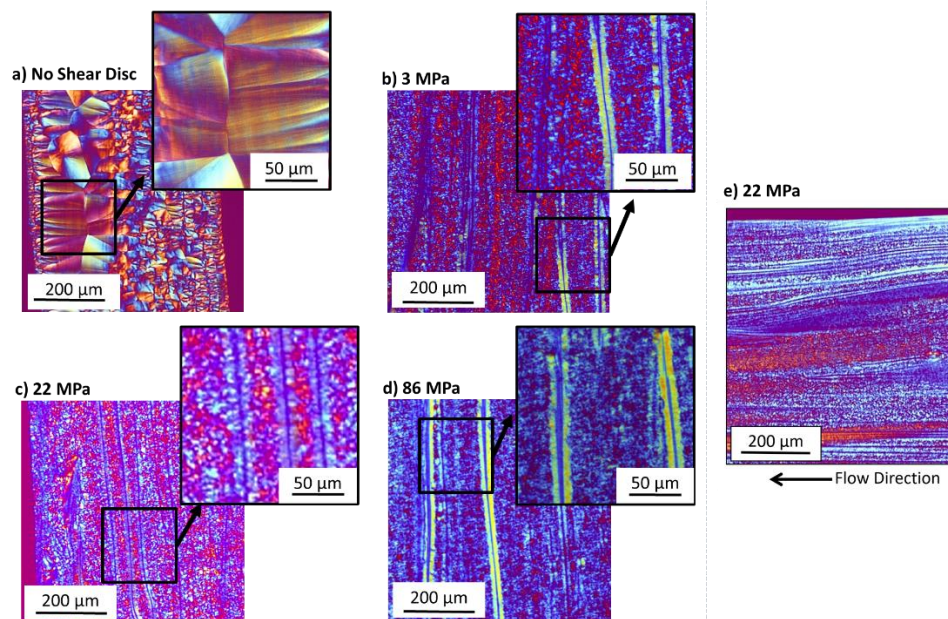
Figure 29: POM images of sheared PA 66 samples. For all samples, the cut is taken 6 mm from the center of the disc, corresponding to a shear rate of 48 s^{-1}. The work levels associated with each image are 0 MPa (a), 3 MPa (b), 22 MPa (c), 86 MPa (d), and 22 MPa (e). Images a-d are shown cut perpendicular to the flow direction, and image e is cut at a secant in the direction of flow. Reprinted [145] with permission from https://doi.org/10.1021/acs.macromol.8b00195. Copyright 2018 American Chemical Society.

A series of experiments to evaluate the stability of nuclei in the shish-kebab structures was first performed in order to confirm high-temperature nuclei stability of the structures. In these experiments, the sample was taken to a temperature high enough to melt the lamellae, but below the equilibrium melting temperature in order to preserve the flow-induced nuclei. The T_m^0 for PA 66 is 277 °C as found by the Hoffman-Weeks method [165]. In this series of experiments, the sample was heated to a maximum temperature of either 275 or 280 °C. It was held for just 1 s, before being quenched to the isothermal crystallization temperature of 200 °C, a temperature known to produce large, spherulitic structures, as shown in Section 3.1.1 [149]. Once quenched to a temperature below T_g, the FSC chip was removed from the instrument and placed under polarized light to analyze the resulting microstructure. The sample on the chip was then returned to the FSC for additional analysis, adding to the cumulative time in the melt. The optical microscopy and calorimetry associated with this analysis is displayed in Figure 30.
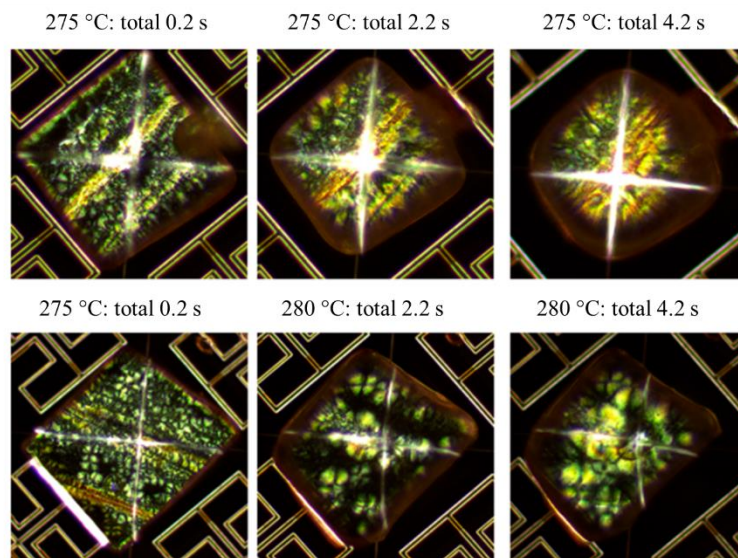
56

Figure 30: Optical evidence of high-temperature nuclei stability of flow-induced structures. POM analysis of the flow-induced structures as a function of time in the melt after the isothermal crystallization at 200 °C after a maximum temperature exposure of 275 °C and 280 °C. Reprinted [145] with permission from https://doi.org/10.1021/acs.macromol.8b00195. Copyright 2018 American Chemical Society.
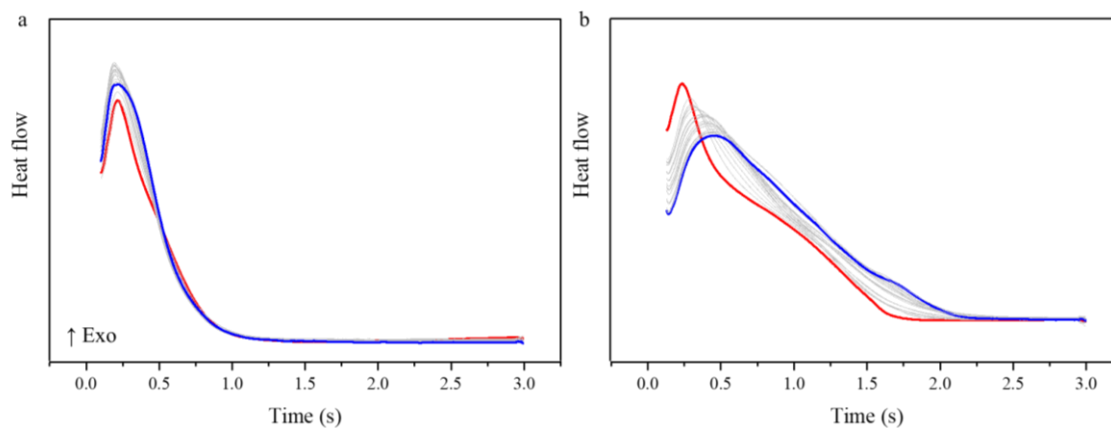

Figure 31: Calorimetric evidence of high-temperature nuclei stability of flow-induced structures. Isothermal crystallization kinetics at 200 °C after exposure at 275 °C (a) and 280 °C (b) for cumulative 20 s isothermal crystallization after 1 s at the annealing temperature in the melt. Red curve is the first crystallization cycle, and each gray curve is an additional 1 s in the melt at the respective melt temperature, and the blue curve indicates a cumulative 20 s in the melt. Reprinted [145] with permission from https://doi.org/10.1021/acs.macromol.8b00195. Copyright 2018 American Chemical Society.

Per figure 31, when the sample is kept below T_m^0, the peak time of crystallization is stable, displaying a consistent peak time of crystallization of approximately 0.24 s even after a cumulative time of 20 s in the melt. The POM analysis displayed in Figure 30a (top row) also shows that the shish is preserved over time, and the kebabs are re-grown after each excursion into the melt phase.

However, when the maximum temperature is taken above T_m^0 to 280 °C, the peak time of crystallization increases to that of the PA 66 under static conditions. It is shown in Figure 31b that after 13 s cumulative time in the melt, the peak time of crystallization remains consistent at ~0.5 s. The optical microscopy shows that over time, the shish structures relax to row-oriented point nuclei, and then finally to isotropic spherulites of larger diameter. The kinetics indicate that after only 2 s in the melt at 280 °C, the peak time of crystallization starts increasing, indicating the destruction/relaxation of the nucleation points from the flow-induced precursors. POM micrographs suggest that after 4 s, there does not appear to be any visible orientation remaining in the sample, but the crystallization kinetics, as shown in Figure 31, indicate that nucleation is still occurring. From this analysis, it is concluded that crystallization kinetics associated with flow-induced precursors and shish-kebab microstructures are preserved at temperatures below the equilibrium melting point, and crystallization kinetics can be studied in the sheared samples at a maximum temperature of 275 °C.

To investigate the isothermal crystallization kinetics of the sheared materials, samples were sectioned utilizing polarized light microscopy at differing work levels to capture at least one shish-kebab structure per FSC sample. The samples were then analyzed in a manner similar to that applied in the quiescent experiments discussed in Chapter 5.1.1, except that the maximum temperature was kept at 275 °C to preserve the flow-induced nuclei. The crystallization half-time as a function of temperature is displayed in Figure 32. It is shown that in the high temperature regime, which has previously been found to indicate heterogeneous nucleation, the shear history decreases the crystallization time, indicating an increase in nucleation efficiency. The nucleation effect increases with increasing work level. At the shear work levels studied here, up to 86 MPa, the system has not yet reached its saturation point regarding nucleating effect, indicating that further increases in work levels should continue to decrease the crystallization time. In the low-temperature regime, corresponding to the homogeneous nucleation mechanism, the crystallization kinetics of the sheared material revert to those associated with the quiescent conditions, confirming that the flow-induced nuclei act in a manner similar to heterogeneous nucleation sites. This crystallization behavior at high supercooling is in agreement with other polymer systems nucleated with heterogeneous impurities, confirming that the flow-induced nuclei affect only the heterogeneous crystallization regime [42,48,166–169].
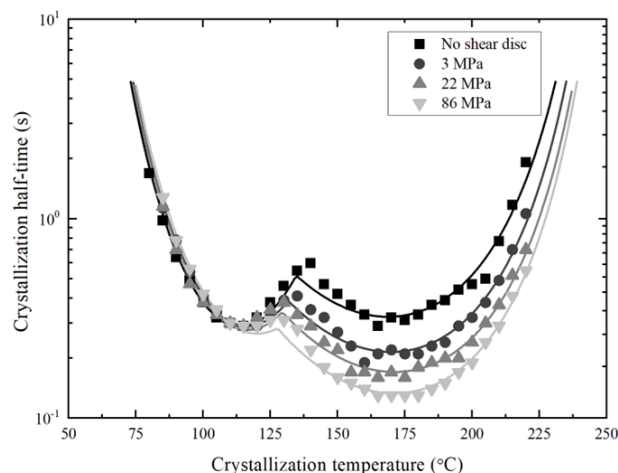
Figure 32: Peak-time of crystallization for PA 66 at increasing work levels. The lines are provided as a visual guide only and do not represent a model or data fit. Reprinted [145] *with permission from https://doi.org/10.1021/acs.macromol.8b00195. Copyright 2018 American Chemical Society.*

It was also found that with increasing shear work, the temperature at which heterogeneous/homogeneous nucleation mechanisms switch, designated by the local maxima in crystallization time, is reduced to lower temperatures. A POM analysis was performed at high and low degrees of supercooling from the melt with an unsheared and sheared sample. These images are displayed in Figure 33, and confirm large, spherulitic crystal growth at high temperature (200 °C), with the appearance of shish-kebab structures developed. The microstructure development at low temperature shows agreement between the sheared and unsheared material, as the features are too small to be seen in POM. Though the flow-induced nuclei are still present, as studied in subsequent experiments, it does not nucleate macro-structures detectable in POM at low temperature.
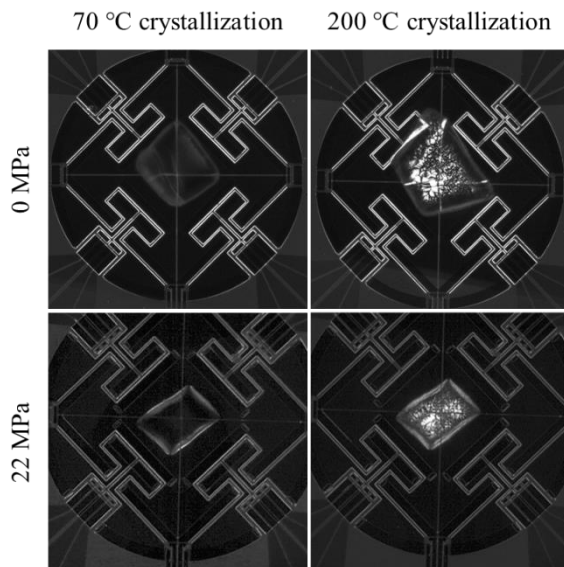
Figure 33: POM images depicting the resulting microstructure melt crystallized at 70 °C (left) and 200 °C (right) of unsheared (top) and sheared (bottom) samples. Reprinted [145] *with permission from https://doi.org/10.1021/acs.macromol.8b00195. Copyright 2018 American Chemical Society.*

A non-isothermal crystallization analysis was then performed to determine the effect of shear history on crystallization from the melt at differing cooling rates. The relative crystallinity as a function of cooling rate is depicted in Figure 34. The cooling analysis technique maintains a maximum temperature of 275 °C to preserve the flow-induced nuclei, and the same specimen is cycled at decreasing cooling rates from 5000 to 10 K/s. A consistent heating rate to the melt of 500 K/s is used to determine the crystallinity formed during the previous cooling cycle [22]. The sheared samples display an early onset of crystallization compared to that of the zero shear disc sample. The critical cooling rate to produce a fully amorphous sample increases from 500 K/s in the unsheared disc to about 2,000 K/s in the sheared materials. This extension of crystal development to higher rates is similar in behavior to heterogeneously nucleated systems [48,170]. The cooling rate required to suppress crystallization is also extended to higher temperatures in the sheared materials, where an increase in shear provides an increase in cooling rate required to suppress crystallization. In the no shear disc, crystallinity is relatively consistent up to rates of approximately 30 K/s, where there is a drastic decrease in crystalline content with increasing cooling rate. The cooling rate required to cause significant reduction in crystalline content is increased with increasing cooling rate to approximately 200 K/s at 86 MPa of shear work history. The ability of the system to crystallize at higher cooling rates after subject to work is expected to

be an immediate benefit to the injection molding community, where cumulative shear history can prove to be an effective tool to increase crystallinity in fast-cooling applications.
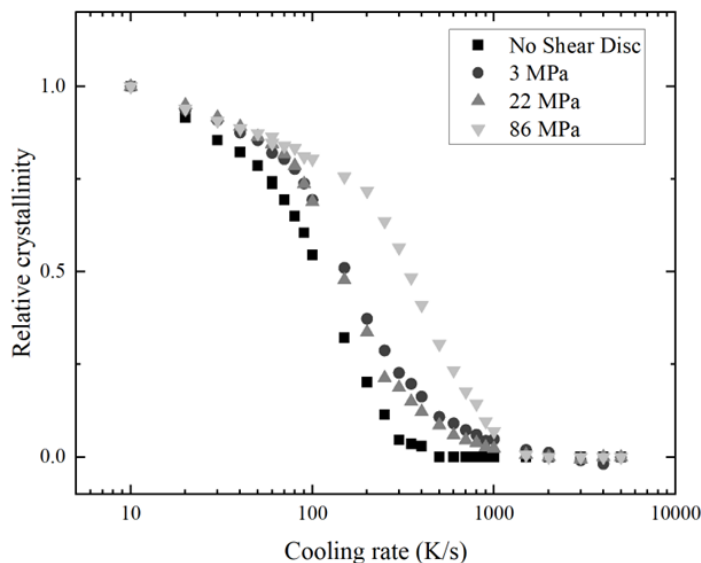

Figure 34: Cooling rate dependence of crystallinity of unsheared and sheared PA 66 (Zytel 101). Reprinted [145] with permission from https://doi.org/10.1021/acs.macromol.8b00195. Copyright 2018 American Chemical Society.

Further flow-induced crystallization experiments were performed to analyze the effects of crystallization temperature with consistent shearing temperature. Figure 35 displays the crystallization onset time as a function of work after shearing at 270 °C and quenching to the crystallization temperatures of 248, 250, and 252 °C. It is shown that with increasing crystallization temperature, the crystallization onset time is increased below the critical work level. For each crystallization temperature, the critical work level required to reduce the onset time of crystallization is approximately the same. This proves that regardless of subsequent crystallization conditions, the same initial entropy change from flow is required to influence flow-induced crystallization, so W_c is consistent.
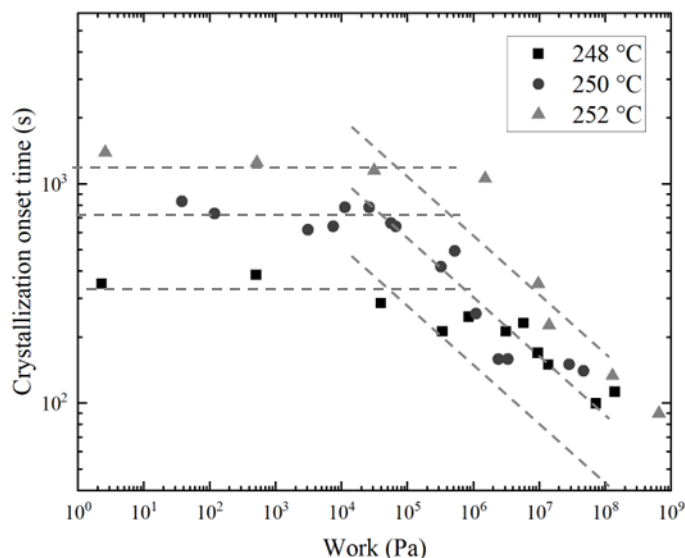
Figure 35:Crystallization onset time as a function of specific work in neat PA 66 using 8 mm cone and plate fixtures. Shearing was performed at 270 °C and the sample was quenched to 248 °C , 250 °C, or 252 °C to monitor crystallization. Reprinted [157] with permission from https://doi.org/10.1002/marc.202200418. Copyright 2022 from Wiley.

6.2 Use of polymer nanocomposites to investigate heterogeneous nucleation

The long, thread-like shish that develop during flow have similar geometric attributes to that of a carbon nanotube (CNT), and so CNT nanocomposites were used for a heterogeneous nucleation comparison. It has been documented that UHMWPE polymer shish diameter are approximately 10 nm and length can reach over 10 μm [163,164], while the CNT used in this masterbatch are of 10 nm diameter and 10 μm length [142]. It is hypothesized that the nucleating efficiency of flow-induced precursors and the efficiency of the heterogeneously nucleated system resulting from the incorporation of CNT may therefore be similar, if the nucleation is primarily derived from the shape-factor of the nucleating entity. CNT nanocomposite samples were prepared at low loading of 0.01, 0.1, and 1 wt-%. After the masterbatch was diluted to the desired CNT content, TEM analysis was performed to confirm minimal agglomeration. Micrographs of increasing magnification from TEM are displayed in Figure 36.
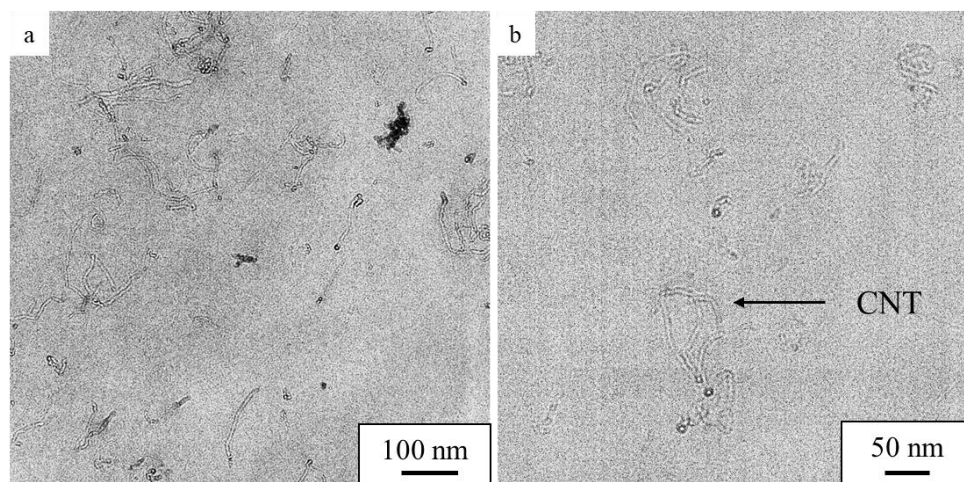
Figure 36: TEM images of PA 66 + 1% CNT. Imaging confirms minimal agglomerations after dilutions were compounded on a twin-screw extruder. Reprinted [157] with permission from https://doi.org/10.1002/marc.202200418. Copyright 2022 from Wiley.

As discussed later, the additive of CNT can greatly accelerate the crystallization of PA 66 nanocomposites. It is important to confirm the formation of the same polymorph in the temperature region where crystallization temperature of PA 66 nanocomposite can be controlled. To confirm the crystal polymorph formed in the presence of the nanotubes, neat PA 66 and 1 % CNT nanocomposite were prepared in the DSC at 10 K/min cooling and subsequently analyzed using WAXS. Figure 37 displays the WAXS pattern of these materials, and the signals display peaks at approximately 20.3 and 23.7 degrees. These peaks relate to the (100) and (010)/(110) lattice planes of the triclinic unit cell indicative of the PA 66 α-form [26].
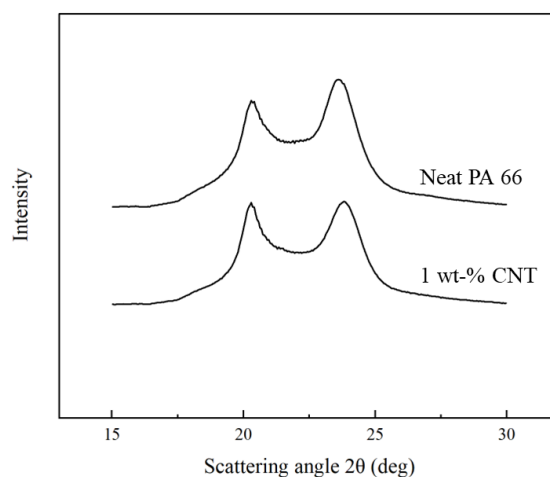

Figure 37: WAXS patterns of neat PA 66 and PA66 + 1% CNT. Samples were crystallized in the DSC at 10 K/min cooling from the melt. Reprinted [157] with permission from https://doi.org/10.1002/marc.202200418. Copyright 2022 from Wiley.

A non-isothermal crystallization analysis was performed at rates ranging from 1 to 4,000 K/s, and the subsequent melting peak (500 K/s heating rate) was analyzed to determine the crystallinity developed during cooling. Representative cooling curves and subsequent heating curves for the neat and 1% CNT nanocomposite samples are shown in Figure 38 and Figure 39, respectively. The lowest cooling rate used (1 K/s) is highlighted in red and the highest cooling rate (4,000 K/s) is highlighted blue, with the range of cooling rates between being displayed in gray. At low cooling rates, there is high signal-to-noise in the peaks that is reduced as the cooling rate increases. Crystallization is observed during higher cooling rates with a stronger exothermic signal in the nanocomposite sample compared to neat PA 66. The peak crystallization temperature as a function of the cooling rate for the neat PA 66 and the PA66/CNT nanocomposites is displayed in Figure 40a. In the CNT nanocomposites, the crystallization temperature is increased approximately 25 – 35 K from that of the neat PA 66. This behavior indicates heterogeneous nucleation by CNT on cooling. The difference in peak crystallization temperature at the different CNT loading levels is difficult to distinguish and is within the margin of error from measurement-to-measurement due to slight differences in sample size and potential fluctuations in CNT content contained in each sample.
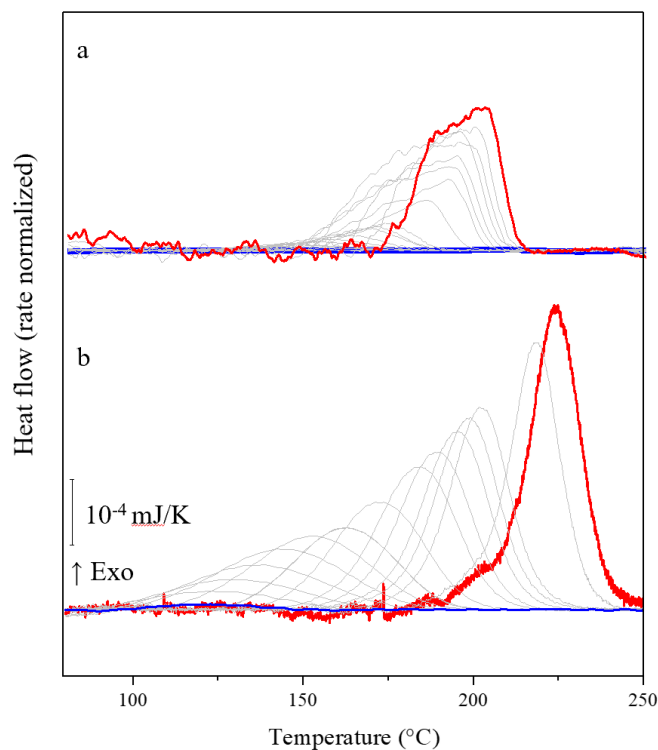
Figure 38: Cooling curves from 4,000 K/s (blue) to 50 K/s (red) for (a) neat PA 66 and (b) PA 66 + 1% CNT. Reprinted [157] with permission from https://doi.org/10.1002/marc.202200418. Copyright 2022 from Wiley.
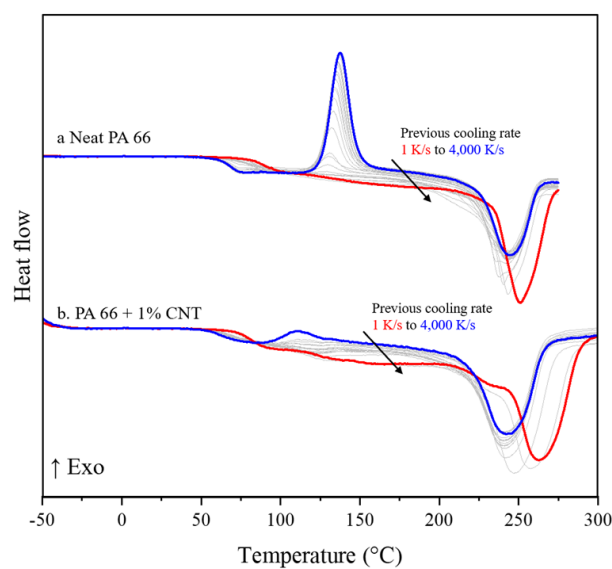

Figure 39: Heating curves at 500 K/s after non-isothermal cooling analysis for (a) neat PA 66 and (b) PA 66 + 1% CNT. Red line indicates heating after lowest cooling rate (1 K/s) and blue line indicates heating trace after fastest cooling rate (4,000 K/s). Reprinted [157] with permission from https://doi.org/10.1002/marc.202200418. Copyright 2022 from Wiley.

The heating curves were collected after each cooling cycle and then used to analyze the crystalline fraction developed during the previous cooling step. The heating curves for the neat PA 66 and PA 66/CNT nanocomposites are shown in Figure 39, where the red and blue curves indicate heating after the lowest cooling rate (1 K/s) and the highest cooling rate (4,000 K/s), respectively. The gray curves indicate the mid-range heating scans completed between these extremes. In this analysis, any exothermic response associated with cold crystallization on heating was subtracted from the melting peak. The relative crystallinity as a function of cooling rate is presented in Figure 40b, which were calculated based on subsequent heating scans where any reorganization from cold crystallization was subtracted from the melting enthalpy, as shown in Figure 39. The data from Figure 39 shows the neat PA 66 has a much more distinct cold crystallization peak than the 1% CNT nanocomposite. In the summarized data plotted in Figure 40b, it is evident that the neat PA 66 sample displays a slow decrease in crystallinity as cooling rate increases from 1 to 80 K/s. At cooling rates greater than 80 K/s, crystallinity decreases as a function of increasing cooling rate until a fully vitrified sample is produced at rates greater than 1,000 K/s. By comparison, the CNT samples exhibit only a slight decrease in crystallinity at cooling rates up to approximately 2,000 K/s, where the sharp decline is initiated. The cooling rates available using FSC (up to 4,000 K/s) cannot outpace crystallization on cooling for these nanocomposite systems, so the critical cooling rate required to produce a fully amorphous sample cannot be detected by the techniques employed here.
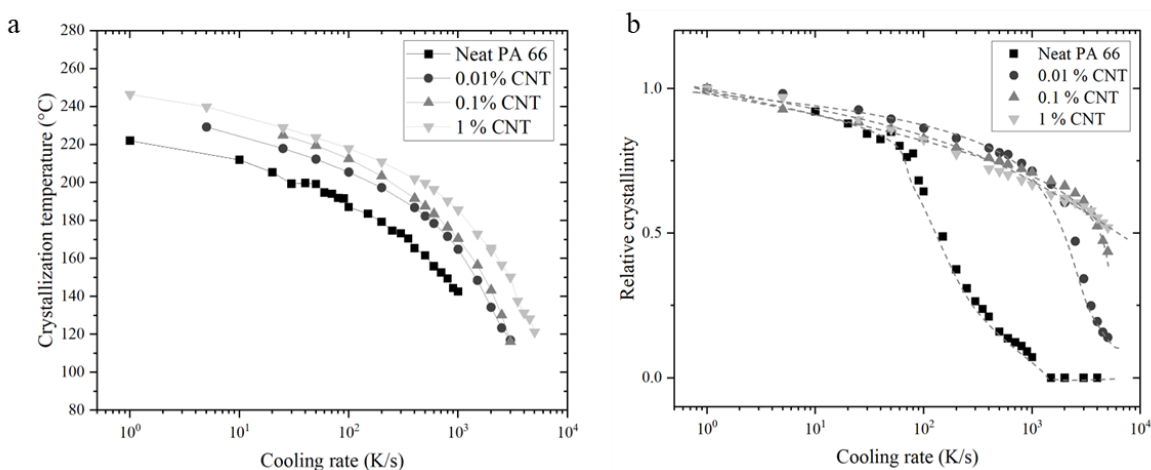

Figure 40: Non-isothermal crystallization of PA 66 (Zytel 101) and its CNT nanocomposites at 0.01, 0.1, and 1 wt-% loading. The peak crystallization temperature on cooling (a) and subsequent melting enthalpy studied at 500 K/s heating (b) are displayed. Reprinted [157] with permission from https://doi.org/10.1002/marc.202200418. Copyright 2022 from Wiley.

An isothermal crystallization experiment was performed on the PA 66/CNT nanocomposites at low loadings. Results indicate that, even at loadings less than 1% CNT, heterogeneous nucleation was so dominant that crystallization could only be studied in the high-temperature regime. The significant nucleating efficiency of the CNT nanocomposites is evident from data presented in Figure 41. Because the onset of crystallization on cooling was increased to higher temperatures, isothermal crystallization signals could not be obtained below 220 °C. From the non-isothermal analysis, the crystallization onset for the CNT nanocomposite systems cooled at 1,000 K/s occurs at approximately 220 °C, and so an accurate peak time of crystallization in the isothermal analysis could not be analyzed at temperatures below 220 °C.
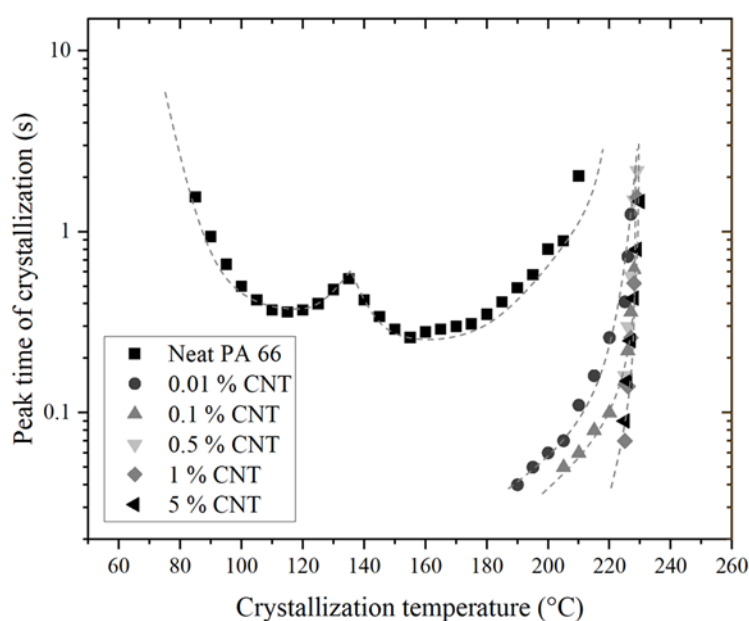

Figure 41: Isothermal crystallization of PA 66 CNT nanocomposites at 0.01, 0.1, and 1% loading as studied by FSC. Reprinted [157] with permission from https://doi.org/10.1002/marc.202200418. Copyright 2022 from Wiley.

The microstructure of the neat PA 66 and corresponding nanocomposites were analyzed by melt crystallizion on an FSC chip at 200 °C for 5 min. The sample adhered to the membrane was then shattered away from the ceramic FSC chip and placed on double sided adhesive on an AFM sample stub for imaging. The AFM images of the material formulations are presented in Figure 42. It is shown with increasing CNT content (left to right), the spherulite size is first reduced and then above a critical level, the spherulites turn to a nodular structure (levels > 0.5% CNT). It has been shown in CNT nanocomposites of poly(butylene succinate) (PBS) that once the CNT level exceeded the saturation limit for nucleating properties, the microstructure changed from spherulitic

below the saturation limit to such a high level of nucleation where spherulite boundaries were not discernable by POM [171]. For reference, the PBS material also formed a continuous network exceeding saturation threshold for rheological, electrical conductivity, and crystallization properties between 0.1 and 0.3% CNT [171].
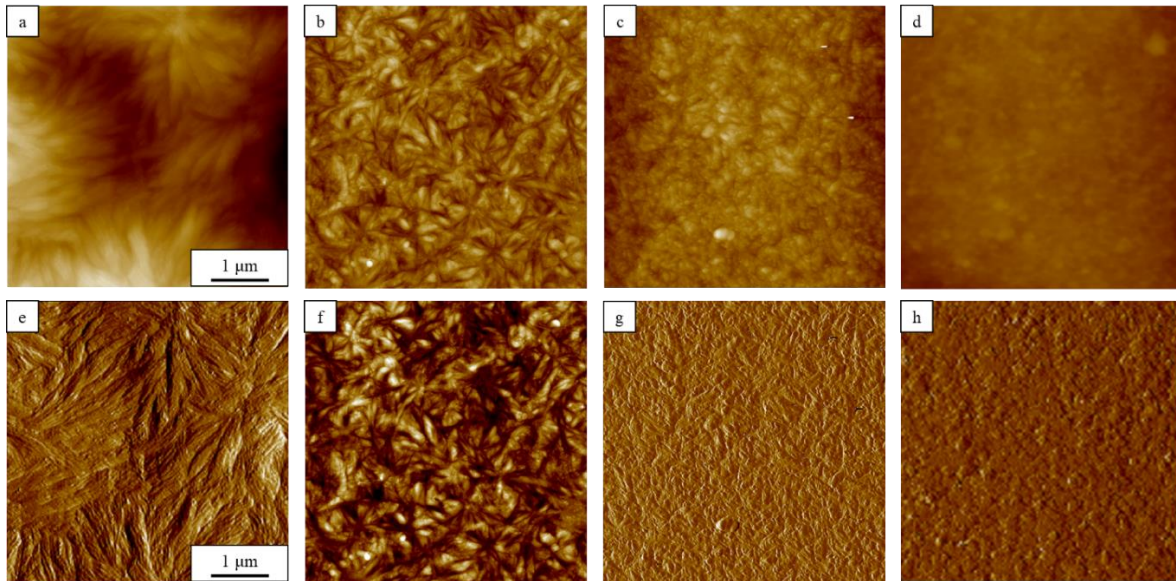

Figure 42: AFM images of PA 66 and its CNT composite melt crystallized at 200 °C. Top row and bottom row images depict height mode collection and peak force error mode collection, respectively. Images arranged from left to right indicate increasing CNT content with neat PA 66 (a, e), PA 66 + 0.01% CNT (b, f), PA 66 + 0.1% CNT (c, g), and PA 66 + 1% CNT (d, h). Reprinted [157] with permission from https://doi.org/10.1002/marc.202200418. Copyright 2022 from Wiley.

Considering the strong influence of all CNT loading levels studied on the crystallization kinetics of the PA 66 matrix, it is hypothesized that even at the lowest loading levels, the CNT provides more nucleating surface availability than is required for maximizing crystallization efficiency in PA 66. One may consider the systems under study here in light of the commonly described saturation threshold known to facilitate a 3-dimensional network of CNT through a matrix. Implications of saturation threshold of reinforcing agents on polymer crystallization are not widely understood, but in all blends studied the CNT forms a continuous network, indicating the polymer has a very short diffusion pathway to either a nucleation surface or a lamellar growth front. The ultra-low saturation threshold measured here by FSC was confirmed in melt-mixed PA 66/CNT systems using standard DSC, where a saturation threshold of 0.04 wt-% was found for electrical conductivity and crystallization temperature on cooling [172]. In the work by Krause [172], it was proposed that the shear applied during the melt-mixing process helps to enable

elongation of the CNT fibers and aid with dispersion, both of which are hypothesized as critical factors to enhancing the nucleation efficiency from the CNT surface.

6.3 Nucleating efficiency of flow-induced nuclei and heterogeneous nucleators

It is hypothesized that the nucleating efficiency of flow-induced precursors and the efficiency of the heterogeneously nucleated system resulting from the incorporation of CNT may therefore be similar, if the nucleation is primarily derived from the shape-factor of the nucleating entity. Figure 43 displays the idealized geometries for the shish (a) and the CNT (b), where the diameter and length are 10 nm and 10 μm, respectively. The shish is comprised of chain-extended crystals [81] that stretch in a flow field and do not relax because shear flow exceeds Rouse time. There are chain entanglements that allow for growth in the length of the stretched segment as the polymer flows [163], as depicted in Figure 43a. The shish can also have an irregular surface, as individual chains can be excluded from the shish, as cilia. In contrast, the CNT does not have any entanglement or surface conformation disorder, making it a perfect surface modification agent, though it can be manipulated using surface modification as is sometimes done to improve the interfacial adhesion to a specific polymer [173]. To compare nucleation effectiveness of the shish and the CNT, sheared samples of neat PA 66 were created to obtain the same fraction of shish as the CNT nanocomposites.
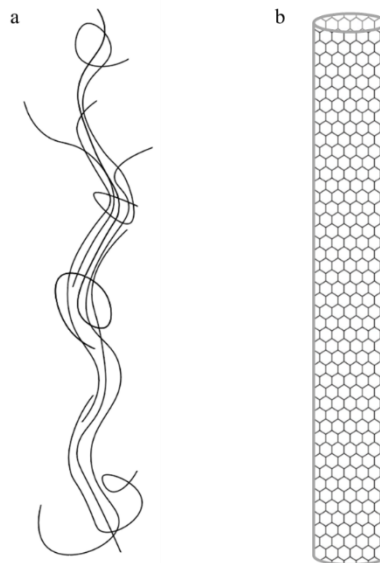

Figure 43: Shish geometry (a) compared to CNT geometry (b), where it is known diameters are similar at 10 nm and lengths are similar, reaching up to 10 μm.

When a polymer melt is subjected to shear, the longest chains are stretched and are unable to relax back to the isotropic state in a shear field before crystallization. This mechanism is the driving factor behind the development of flow-induced precursors that nucleate a polymer system subjected to flow. The number of stretched chains is dependent on both the molecular weight distribution of the polymer system and the level of shear imposed on the melt. The Rouse time (τ_R), or relaxation time of the longest chains, is a determining factor for the temporal stability of stretched long chains in the melt. In the case of linear polymers like PA 66, the Rouse time of the system is given by

$$\tau_R = \left(\frac{M}{M_e}\right)^2 \tau_e$$

where M is a specific molecular weight in the system, M_e is the molecular entanglement weight, and τ_e is the Rouse time of an entangled strand. The molecular weight distribution for the neat Zytel 101 is displayed in Figure 44.
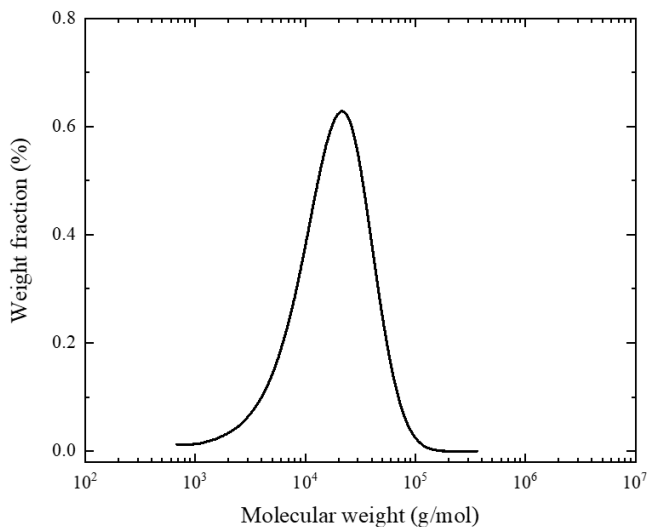
Figure 44: Molecular weight distribution of PA 66 (Zytel 101). Mn = 11,300 g/mol, Mw = 22,700 g/mol, and Mw/Mn = 2.0 calculated using the Mark-Houwink parameters [145].

Given the equation above, the amount of stretched chains at any given shear rate can be calculated based on the proportion $(M_2/M_1)^2 = (\tau_{R2}/\tau_{R1})$ [102]. In the case of PA 66, the critical shear rate to induce chain deformation from orientation/stretching is approximately 0.1 s^{-1} according to the Cox-Merz rule failure, as shown in Figure 45. For this analysis, the neat PA 66 was sheared at oscillatory frequencies ranging from 0.1 to 100 rad/s and steady shear rates from 0.01 to 100 s^{-1}. Where the viscosity (steady shear) diverges from the complex viscosity (oscillatory

shear), the molecules have become stretched and are showing a shear-thinning viscosity response. This point is the critical shear rate to induce stretching under steady shear conditions. The Rouse time for the longest chain can then be calculated as the reciprocal of the critical shear rate (0.1 s^{-1}), yielding a relaxation time of 10 s.

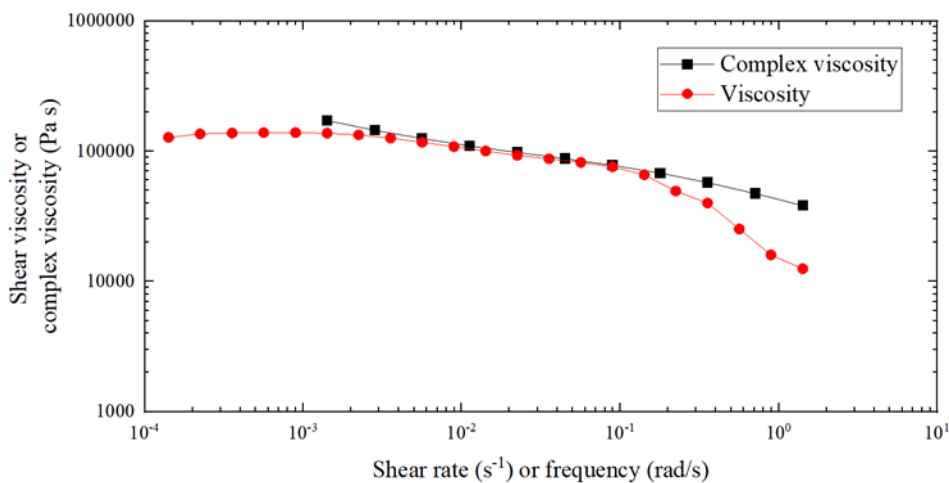*Figure 45: Cox-Merz analysis to find the onset of orientation in steady shear flow for neat PA 66. Reprinted* [157] *with permission from https://doi.org/10.1002/marc.202200418. Copyright 2022 from Wiley.*

In this system, where M is the molecular weight of the longest chains $\sim 2 \times 10^5$ g/mol, and 0.1 s^{-1} is the shear rate to induce orientation, the fraction of stretched chains as a function of shear rate is plotted in Figure 46. It is noted that since 0.1 s^{-1} is the critical shear rate to induce orientation, zero stretched fraction would be expected at shear rates below 0.1 s^{-1}. From this calculation, a specific fraction of stretched chains can be compared to a similar weight fraction of CNT to compare nucleation efficiency. Since the long, needle-like geometry of the shish is similar to the geometry of a CNT, the self-nucleation of the flow-induced system can be compared to that of a heterogeneously nucleated nanocomposite. It is expected that the stretched chains comprised of the high molecular weight fraction will constitute the shish of the oriented structures and the shorter chains will remain isotropic and may form the kebabs and spherulitic structures when further crystallized [69].
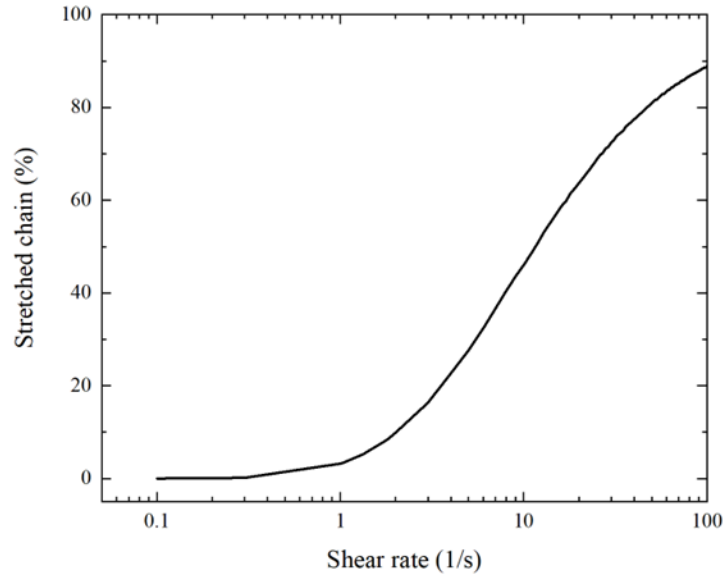
Figure 46: Amount of stretched chains as a function of shear rate in PA 66.

For the proportion calculation to describe fraction of stretched chains as a function of shear rate $(M_2/M_1)^2 = (\tau_{R2}/\tau_{R1})$, an example calculation is presented for the target shear rate of 0.6 s^{-1}.

$$\left(\frac{2 \times 10^5 \ g/mol}{X \ g/mol}\right)^2 = \frac{0.1 \ s^{-1}}{0.6 \ s^{-1}}$$

This calculation yields a critical molecular weight of 81,650 g/mol at 0.6 s^{-1}. To find the fraction of stretched chains at this shear rate, the M_w fraction above this critical molecular weight value are calculated to be a total fraction of 1%. As summarized in Table 2, shear rates of 0.16, 0.27, and 0.60 s^{-1} correspond to 0.01, 0.1, and 1 % stretched chains. These levels can be compared to CNT loadings to analyze nucleating efficiency of the shear rates and nanocomposite loading studied here.

Table 2: Shear rate required to produce a specific fraction of stretched chains relevant to CNT loading

Shear rate (s^{-1})	Stretched chains (%)
0.16	0.01
0.27	0.1
0.60	1

The nucleating efficiency of the sheared PA 66 is compared to that of the CNTs at the same stretching fraction by inducing a specified amount of stretched chains using the shear rate calculation summarized in Table 2. Stretching fractions of 0.01, 0.1, and 1% were targeted by shearing at 0.16, 0.27, and 0.6 s^{-1}, respectively, for 60 s. This was compared to the quiescent crystallization of PA 66/CNT nanocomposites at 0.01, 0.1, and 1 % at 258 °C. The crystallization onset time as a function of stretched fraction is shown in Figure 47, where it can be clearly demonstrated that the CNT has a much higher nucleating effect than the flow-induced precursors. With the same stretched fraction, the time required to crystallize the sheared neat PA 66 is at least five times greater than what is required to crystallize the nanocomposites. The highly ordered surface of the CNT is more regular and has perfect conformation as it is rod-like graphite, making it a better surface to nucleate crystallization. Though the flow-induced precursors can accelerate crystallization compared to the quiescent matrix, the surface of the shish is not an ideal surface for nucleation.
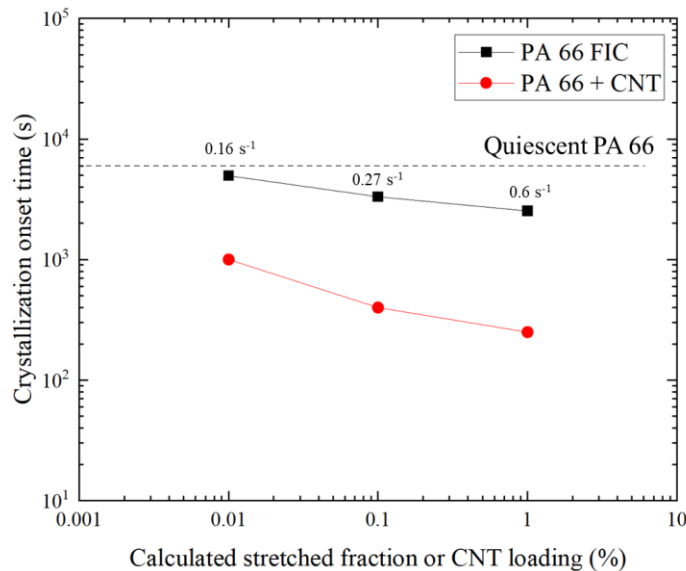
Figure 47: Crystallization onset time as a function of stretched fraction comprised of shish or CNT. Crystallization takes place at 258 °C.

The complex viscosity as a function of oscillatory frequency for the neat PA 66 and its nanocomposites are displayed in Figure 48. It can be seen that with increasing CNT content, the complex viscosity at 270 °C is increased, which is confirmed in other polymer systems including PC [174] and PA 11 [175]. The 1 % CNT loading also displays more shear sensitivity, as a shear-thinning effect is more pronounced than in the low CNT loaded samples and neat PA 66. It has

been discussed that shear forces can easily align the CNT, which will subsequently destruct the chain entanglements in the flow field, producing a larger shear-thinning effect [175]. The viscosity differences of the materials are also more distinct at low frequencies, as shear thinning results in approximately the same viscosity at high frequencies.

Figure 48: Complex viscosity of PA 66 and its CNT nanocomposites at 270 °C as a function of frequency. Reprinted [157] with permission from https://doi.org/10.1002/marc.202200418. Copyright 2022 from Wiley.

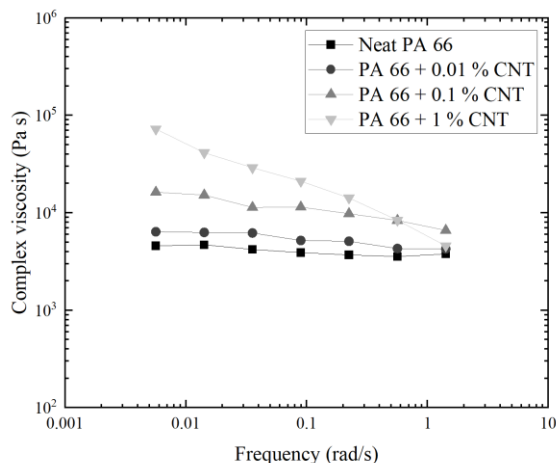To compare the flow-induced crystallization kinetics of the neat system to that of the unsheared CNT nanocomposite, the 1% CNT composite was used as a reference material. A series of shear rates ranging from 0 to 100 s^{-1} at 60 s shearing time were studied, and it was found that shear had no effect on crystallization in the CNT nanocomposite system in the analyzed range of parameters, as shown in Figure 49. It appears that the high nucleating efficiency of the CNT exceeds any crystallization acceleration from flow. This system showed no synergistic effects of CNT and flow, as the nucleating effects of the CNT enabled an apparent minimum crystallization time in the PA 66 material. When the onset of crystallization (10% conversion) as a function of shear work in the nanocomposite system was compared to that of the neat PA 66, plotted in Figure 50, the onset of crystallization is constant at approximately 100 s, where no critical work level was shown to reduce the onset time of crystallization. It is expected that under practical conditions encountered in typical melt processing at industrial scale, the CNT nucleation would provide for a more homogenous crystal development, where the distribution in shear work across the part geometry would not be a critical factor.
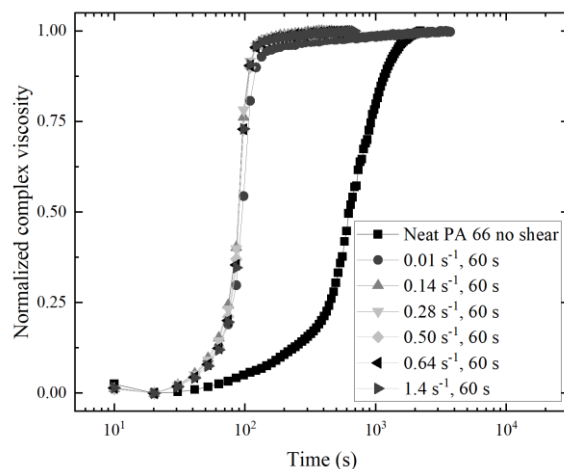
Figure 49: Complex viscosity as a function of time for PA 66 + 1% CNT at differing shear rates at constant shear time (60 s) crystallizing at 250 °C. Reprinted [157] with permission from https://doi.org/10.1002/marc.202200418. Copyright 2022 from Wiley.

The neat PA 66 shear history was extended to higher work levels to explore if the sheared neat PA 66 could reach faster crystallization onset than sheared PA 66/CNT nanocomposite at a crystallization temperature of 250 °C. It was found that there is an upper threshold for saturation in the neat PA 66 sample, where the crystallization onset time reaches a minimum, the addition of increased shearing rate and time does not further reduce onset time of crystallization. This onset time of crystallization is equal to that of the PA 66/CNT nanocomposite at 100 s, indicating there is either (1) a minimum time for crystallization in the PA 66 sample at 250 °C regardless of increased heterogeneous nucleation sites, whether they are from foreign particles or stretched PA 66 fraction or (2) the minimum time to measure crystal development using this technique is 100 s, and crystallization faster than 100 s cannot be detected fast enough due to cooling limitations.

Figure 50: Onset time of crystallization for PA 66 + 1% CNT in comparison to neat PA 66 at 250 °C. Reprinted [157] *with permission from https://doi.org/10.1002/marc.202200418. Copyright 2022 from Wiley.*
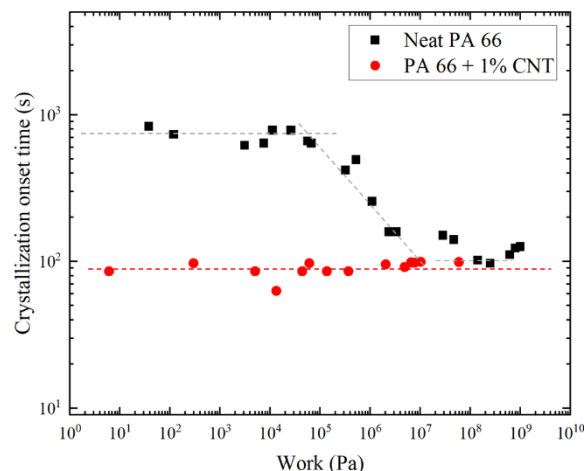
The flow-induced crystallization of 1 % CNT nanocomposites was further studied at a range of crystallization temperatures to better understand if the saturation behavior depicted in Figure 50 is a function of a maximum level of nucleation in PA 66 or a limitation of the crystallinity measurement using the rotational rheometer. Similar to the method used above, the PA 66 + 1 % CNT nanocomposite was heated to 290 °C to erase the thermal/shear history, cooled to 270 °C to perform the steady shear step at a specific rate and time, and cooled to crystallization temperatures of 250, 255, 258, or 260 °C to monitor crystallization using SAOS. The crystallization onset time as a function of specific work calculation is plotted in Figure 51. It can be seen that the crystallization onset time for the 1 % CNT nanocomposite is approximately 100 s for crystallization at both 250 and 255 °C, indicating the equipment cannot measure a crystallization onset time less than 100 s, confirming this behavior is a limitation of this technique/equipment as a reduction in crystallization temperature should yield a reduction in crystallization time. However, the crystallization behavior at 258 and 260 °C show the onset time for crystallization is consistent through the full specific work range studied here. In the neat PA 66 sample, flow-induced crystallization initiated at 0.1 MPa. The characteristic FIC indicator of a reduced crystallization onset time does not occur in the PA 66 + 1 % CNT, indicating that this material has reached its saturation threshold and cannot be further nucleated with the addition of shear beyond the critical work threshold to initiate FIC.

Figure 51: Onset time of crystallization for PA 66 + 1% CNT at crystallization temperature of 250, 255, 258, and 260 °C. Reprinted [157] with permission from https://doi.org/10.1002/marc.202200418. Copyright 2022 from Wiley.

The crystallization onset time of PA 66 + 1 % CNT at 258 °C is approximately 300 s, which is above the minimum threshold collection for this experiment, as observed when crystallizing at 250 °C and 255 °C. PA 66 with 0.01 % and 0.1 % CNT were also tested for FIC properties by shearing at 270 °C and crystallizing at 258 °C, as shown in Figure 52. Both 0.01 and 0.1 % CNT nanocomposites show decreasing onset of crystallization time at work levels greater than the critical work level, suggesting that if the CNT content is below the saturation threshold, there is capacity for increased nucleation activity and shear flow can further nucleate the PA 66.
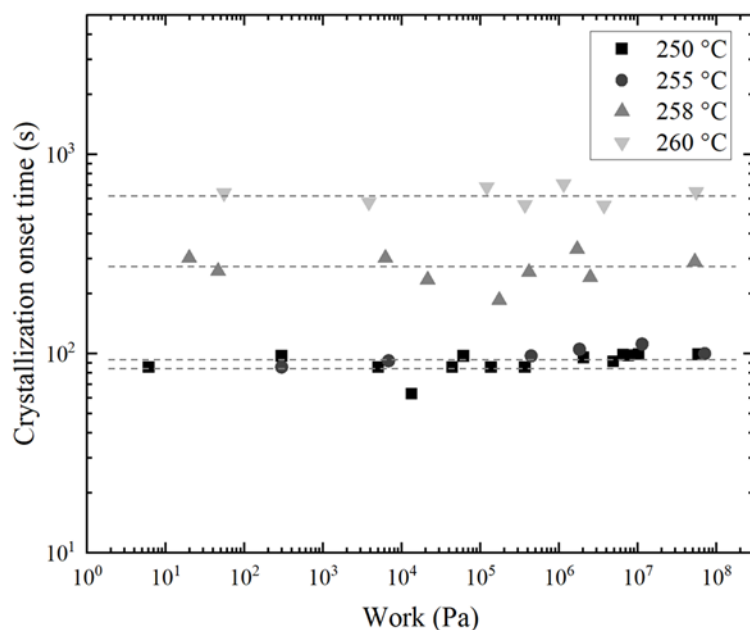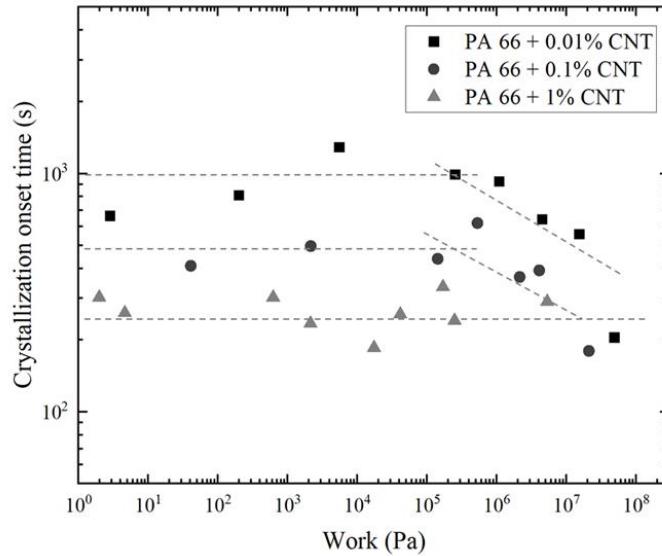
Figure 52: Onset time of crystallization for PA 66 + 0.01, 0.1, and 1% CNT at crystallization temperature of 258 °C. Reprinted [157] with permission from https://doi.org/10.1002/marc.202200418. Copyright 2022 from Wiley.

To properly reflect on this experimental evidence, the PA 66 experimental data is applied to the commonly referenced Housman model. The model is proposed in Figure 53, where the x-axis has been modified to indicate shear work, instead of the previously used shear rate, to account for critical factors of shearing time and viscosity which have been confirmed.
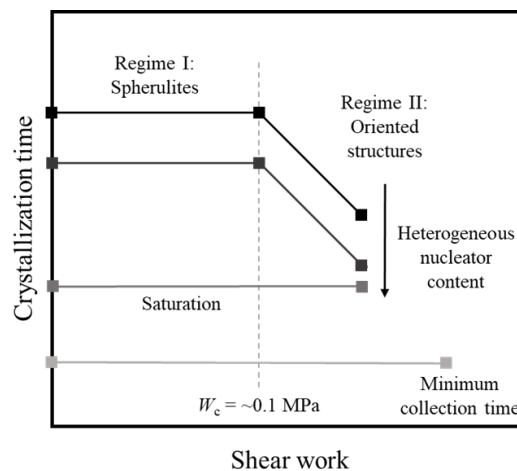
Figure 53: Proposed model of shear work's influence on crystallization time for PA 66. The model has been updated from the original Housman model [82]. Reprinted [157] with permission from https://doi.org/10.1002/marc.202200418. Copyright 2022 from Wiley.

Flow-induced crystallization effects in polymer nanocomposites have recently been studied, and it was found that while the nanotubes can act as a heterogeneous nucleation site under quiescent crystallization, the addition of shear flow had synergistic effects on subsequent

78

crystallization [53,105,113,117,176]. In comparison to the PA 66 studied here, it appears that a minimum crystallization time has already been met simply by the addition of the melt compounded CNT at only 1 % loading. Shear had no additional effects on the crystallization in the nanocomposite system when the nanotube content is over the saturation threshold, noting that the PA 66 has a minimum time of crystallization at a specific temperature regardless of the heterogeneous nucleation mechanism (self- vs foreign-nucleated). However, if the nucleation content is lower than the saturation limit, shear flow can further nucleate the crystallization process. In summary, the critical parameters that influence CNT nanocomposite flow-induced crystallization are (1) the large surface area to volume ratio of the CNT (2) the dispersion of the CNTs in the polymer matrix, and (3) the crystallization kinetics of the polymer. Compared to crystallization of sheared samples subjected to flow that have the same stretched/shish fraction, it was determined the regular surface of the CNT is a more favorable nucleating surface than the shish.

7. Summary and Conclusions

This dissertation details the quiescent and flow-induced crystallization kinetics of neat PA 66. The crystallization kinetics and microstructure formed at high rates and degrees of supercooling, which had not yet been studied in a sheared polymer under controlled shearing rate, time, and thermal conditions, were investigated. After using calorimetry and rheometry as accurate and informative sample preparation tools, the subsequent microstructure was analyzed. PA 66/CNT nanocomposites with differing loading levels were then studied as a surrogate to the shish precursor that was shown to nucleate PA 66 material. It was hypothesized that the nucleating efficiency of flow-induced precursors and the efficiency of the heterogeneously nucleated system resulting from the incorporation of CNT may therefore be similar, if the nucleation is primarily derived from the shape-factor of the nucleating entity. The goal of this work was that the polymer science fields of thermal analysis and rheology be combined to bridge a fundamental knowledge gap to improve the science of plastic manufacturing.

First, neat PA 66 was studied both isothermally and non-isothermally using fast scanning calorimetry. The bimodal peak time of crystallization for PA 66 was shown to be attributable to the nucleation mechanism change from heterogeneous at high temperature (>130 °C) to homogeneous at low temperature (<130 °C). Using FSC as a sample preparation tool for polarized optical microscopy and atomic force microscopy, analyses showed crystal superstructures formed in the heterogeneous and homogeneous regimes produced large, spherulitic structures and nodular domains, respectively. A polymorphic transition was also found to occur in the range of approximately 110 – 120 °C, where the α-structure was developed at low supercooling and the γ-form was produced at high supercooling. Under non-isothermal cooling conditions, rates over 100 K/s the PA 66 were found to significantly suppress crystallization in PA 66 and produce a completely amorphous sample at rates over cooling rates exceeding 1,000 K/s.

The crystallization of neat PA 66 was then studied after imposition of precise shearing conditions, where an emphasis was placed on the shearing time, shearing rate, and viscosity of the melt; factors are combined to yield a shear work value. The flow-induced crystallization kinetics were first studied by monitoring the increase in viscosity as the crystal fraction developed over time. Plotting the onset of crystallization as a function of work yielded a critical shear rate of 0.1 s^{-1} and a critical work level of approximately 0.1 MPa required to induce the development of the stretched polymer chain entity known as the shish. Once a critical work level was established,

samples were preconditioned under controlled shearing conditions, solidified, removed from the rheometer, and subsequently sectioned and analyzed using fast scanning calorimetry. Precursor structures visible in polarized optical microscopy allowed for the precise sample selection where at least one shish was sectioned and analyzed in each calorimetric analysis. The high-temperature stability below the equilibrium melting temperature was a critical factor in this analysis, as the stretched fraction remained stable in the melt and could be subjected to many cycles of thermal analysis per sample without destroying the flow-induced precursors. It was found that under isothermal conditions, shearing only affected crystallization in the heterogenous regime, and even extended heterogeneous nucleation to lower temperatures than those associated with nucleation in the quiescent samples. Under non-isothermal cooling conditions, the sheared samples were shown to start crystallizing at higher cooling rates than that of the unsheared sample.

PA 66/CNT nanocomposites at low loadings (0.01 – 1 wt%) were then analyzed at quiescent conditions. At isothermal conditions, even 0.01 % CNT was able to reduce crystallization time by an order of magnitude. With increasing CNT content, time for crystallization was reduced and even outpaced cooling rates obtainable by FSC analysis. In non-isothermal experiments, the crystallization temperature on cooling could be increased 20 K higher with the addition of CNT, and rates needed to suppress crystallization on cooling exceeded the capacity of the FSC unit (> 4,000 K/s). AFM imaging of the topography of samples crystallized at 200 °C showed large spherulites in the neat PA 66 specimen, decreased spherulite size at 0.01 % CNT, and nodular crystal growth at 0.1 and 1 % CNT, though X-ray characterization showed high temperature crystallization would still produce the α-phase, as is true in the neat PA 66 sample.

Crystallization after flow in the CNT nanocomposites at 1 % loading showed no effect from shear, indicating that the CNTs have already saturated the heterogeneous crystallization potential in the nanocomposite, and shearing provided no additional contribution to acceleration of crystallization time. At 0.01 and 0.1 % CNT, which calorimetry showed were not above the saturation limit for nucleating crystallization, the addition of a flow field could further nucleate the system if sheared above the critical work level. The content of CNTs did not affect the critical work level for precursor development. The CNTs proved to be more efficient in nucleating the PA 66 than flow at the same volume content, as calculated using the molecular weight distribution of the polymer material. This is concluded to be due to the high-temperature stability in the melt.

It is expected that these results will help scientists and process engineers determine the relationship between part processing under typical manufacturing conditions and final microstructure development. Since the resulting microstructure has been shown to influence the shrinkage/warpage of molded parts and final part properties, the predication of crystalline content, superstructure, and polymorph, is critical for the next stage of advanced manufacturing. It is desired that the process-relevant cooling conditions studied here under quiescent conditions, after shear flow, and in the presence of nanoparticles can help clarify the crystallization mechanisms in processed PA 66.

7.1 Recommendations for further study

The work described in this dissertation reflects the crystal nucleation in PA 66 and its CNT nanocomposites in the quiescent state and after subjected to a flow field. It is expected that other polymer material families will nucleate with similar characteristics to the PA 66, but further work is needed to confirm the nucleating behavior is universal. Crystal nucleation studies showed saturation with CNT loadings of only 1 wt-% CNT, but preliminary studies in PEEK show the threshold for saturation is approximately 5 wt-% CNT [170], indicating that the nucleating efficiency is different for individual polymers. Other polymer families including iPP, PLA, and PA 6 are thought to be good candidates for initial next steps in studying a variety of chain mobility and chemistries.

The nucleating efficiency of the CNT in PA 66 is extremely effective, even greater than self-nucleation of stretched shish when calculated to be at the same surface area as CNT. It would be beneficial to further understand why the CNT is such an efficient nucleant in PA 66 compared to other materials. A variety of lengths and diameters of CNTs could be studied to understand the role of surface area impact on crystal nucleation. In addition, surface modification could be performed to the surface of the CNT to understand the implications of the conformationally perfect surface of the unmodified CNT. The trade-off between crystal nucleation and interphase development for mechanical properties can be better understood.

The analysis of flow-induced crystallization in PA 66 using other reinforcing agents, additives, and fillers, is also thought to be a valuable endeavor. The high surface area and aspect ratio of the CNT proved to be an extremely effective nucleating medium. However, other materials like talc, carbon fiber, glass fiber, and calcium carbonate are all common fillers and reinforcing agents used in PA 66. Their contribution to crystal nucleation and flow-induced crystallization would prove to be beneficial for industry melt processing and a fundamental science regarding polymer crystallization.

References

[1]   G.W. Ehrenstein, Polymeric materials : structure, properties, applications, Hanser Gardner Publications, Inc., Cincinatti, OH, 2001.

[2]   L. Mandelkern, Crystallization of Polymers: Volume 2: Kinetics and Mechanisms, 2 ed, Cambridge University Press, Cambridge, UK, 2004.

[3]   E. Piorkowska, G.C. Rutledge, Handbook of polymer crystallization, John Wiley & Sons, 2013.

[4]   D. Turnbull, J.C. Fisher, Rate of nucleation in condensed systems, *J. Chem. Phys.* 17 (1949) 71–73. https://doi.org/10.1063/1.1747055.

[5]   C. Schick, R. Androsch, J.W.P. Schmelzer, Homogeneous crystal nucleation in polymers, *J. Phys. Condens. Matter* 29 (2017). https://doi.org/10.1088/1361-648X/aa7fe0.

[6]   K. Herrmann, O. Gerngross, W. Abitz, Zur röntgenographischen Strukturerforschung des Gelatinemicells, *Zeitschrift für Phys. Chemie* 10B (1930) 371–394.

[7]   A. Keller, A. O'Conner, Large periods in polyethylene: the origin of low-angle X-ray scattering, *Nature* 180 (1957) 1289–1290.

[8]   P.J. Flory, On the Morphology of the Crystalline State in Polymers, *J. Am. Chem. Soc.* 84 (1962) 2857–2867. https://doi.org/10.1021/ja00874a004.

[9]   J.D. Hoffman, C.M. Guttman, E.A. DiMarzio, On the problem of crystallization of polymers from the melt with chain folding, *Faraday Discuss. Chem. Soc.* 68 (1979) 177–197. https://doi.org/10.1039/DC9796800177.

[10] W. Hu, D. Frenkel, V.B.F. Mathot, Intramolecular Nucleation Model for Polymer Crystallization, *Macromolecules* 36 (2003) 8178–8183. https://doi.org/10.1021/ma0344285.

[11] J.I. Lauritzen, J.D. Hoffman, Formation of polymer crystals with folded chains from dilute solution, *J. Chem. Phys.* 31 (1959) 1680–1681. https://doi.org/10.1063/1.1730678.

[12] S.T. Milner, Polymer crystal-melt interfaces and nucleation in polyethylene, *Soft Matter* 7 (2011) 2909–2917. https://doi.org/10.1039/c0sm00070a.

[13] M.L. Di Lorenzo, M.C. Righetti, Crystallization-induced formation of rigid amorphous fraction, *Polym. Cryst.* 1 (2018) 1–14. https://doi.org/10.1002/pcr2.10023.

[14] B. Wunderlich, Reversible crystallization and the rigid-amorphous phase in semicrystalline macromolecules, *Prog. Polym. Sci.* 28 (2003) 383–450. https://doi.org/10.1016/S0079-6700(02)00085-0.

[15] H. Suzuki, J. Grebowicz, B. Wunderlich, Transition of Poly(oxymethylene), *Br. Polym. J.* 17 (1984) 1984–1986.

[16] S. Wietzke, C. Jansen, M. Reuter, T. Jung, J. Hehl, D. Kraft, S. Chatterjee, A. Greiner, M. Koch, Thermomorphological study of the terahertz lattice modes in polyvinylidene fluoride and high-density polyethylene, *Appl. Phys. Lett.* 97 (2010). https://doi.org/10.1063/1.3462312.

[17] J.H. Reinshagen, R.W. Dunlap, The effects of melt history, crystallization pressure, and crystallization temperature on the crystallization and resultant structure of bulk isotactic polypropylene, *J. Appl. Polym. Sci.* 19 (1975) 1037–1060. https://doi.org/10.1002/app.1975.070190413.

[18] H. Yokota, T. Kawakatsu, Nucleation theory of polymer crystallization with conformation entropy, *Polymer* 186 (2020) 121975. https://doi.org/10.1016/j.polymer.2019.121975.

[19] J. Xu, G. Reiter, R.G. Alamo, Concepts of nucleation in polymer crystallization, *Crystals*

11 (2021) 1–19. https://doi.org/10.3390/cryst11030304.

[20] F. De Santis, S. Adamovsky, G. Titomanlio, C. Schick, Isothermal nanocalorimetry of isotactic polypropylene, *Macromolecules* 40 (2007) 9026–9031. https://doi.org/10.1021/ma071491b.

[21] C. Silvestre, S. Cimmino, D. Duraccio, C. Schick, Isothermal Crystallization of Isotactic Poly (propylene) Studied by Superfast Calorimetry, *Macromol. Rapid Commun.* (2007) 875–881. https://doi.org/10.1002/marc.200600844.

[22] A.M. Rhoades, J.L. Williams, R. Androsch, Crystallization kinetics of polyamide 66 at processing-relevant cooling conditions and high supercooling, *Thermochim. Acta* 603 (2015) 103–109. https://doi.org/10.1016/j.tca.2014.10.020.

[23] A. Mollova, R. Androsch, D. Mileva, C. Schick, A. Benhamida, Effect of supercooling on crystallization of polyamide 11, *Macromolecules* 46 (2013) 828–835. https://doi.org/10.1021/ma302238r.

[24] J.E.K. Schawe, Influence of processing conditions on polymer crystallization measured by fast scanning DSC, *J. Therm. Anal. Calorim.* 116 (2014) 1165–1173. https://doi.org/10.1007/s10973-013-3563-8.

[25] M.I. Kohan, Nylon Plastics Handbook, Hanser/Gardner Publications, Inc., Cincinatti, OH, 1995.

[26] C.W. Bunn, E. V. Garner, The crystal structures of two polyamides ('nylons'), *Proc. R. Soc. London. Ser. A. Math. Phys. Sci.* 189 (1947) 39–68. https://doi.org/10.1098/rspa.1947.0028.

[27] G.F. Schmidt, H.A. Stuart, Gitterstrukturen mit räumlichen Wasserstoffbrückensystemen und Gitterumwandlungen bei Polyamiden, Zeitschrift fur Naturforsch. - *Sect. A J. Phys. Sci.* 13 (1958) 222–225. https://doi.org/10.1515/zna-1958-0308.

[28] Diffraction of small X-rays by fibres consisting to crystals: Application of theory to polyamides, *J. of Physics and Chemistry of Solids* 2 (1957) 301–311.

[29] M.L. Colclough, R. Baker, Polymorphism in nylon 66, *J. Mater. Sci.* 13 (1978) 2531–2540. https://doi.org/10.1007/PL00020144.

[30] H.W. Starkweather, G.A. Jones, Crystalline transitions in powders of nylon 66 crystallized from solution, *J. Polym. Sci. Part A-2, Polym. Phys.* 19 (1981) 467–477. https://doi.org/10.1002/pol.1981.180190307.

[31] S. Dasgupta, W.B. Hammond, W.A. Goddard, Crystal structures and properties of nylon polymers from theory, *J. Am. Chem. Soc.* 118 (1996) 12291–12301. https://doi.org/10.1021/ja944125d.

[32] N.A. Jones, E.D.T. Atkins, M.J. Hill, Investigation of solution-grown, chain-folded lamellar crystals of the even-even nylons: 6 6, 8 6, 8 8, 10 6, 10 8, 10 10, 12 6, 12 8, 12 10, and 12 12, *J. Polym. Sci. Part B Polym. Phys.* 38 (2000) 1209–1221. https://doi.org/10.1002/(SICI)1099-0488(20000501)38:9<1209::AID-POLB13>3.0.CO;2-9.

[33] F. Rybnikář, P.H. Geil, Melting and recrystallization of PA-6/PA-66 blends, *J. Appl. Polym. Sci.* 49 (1993) 1175–1188. https://doi.org/10.1002/app.1993.070490706.

[34] F. Khoury, The formation of negatively birefringent spherulites in polyhexamethylene adipamide (nylon 66), *J. Polym. Sci.* 33 (1958) 389–403. https://doi.org/10.1002/pol.1958.1203312637.

[35] J.H. Magill, Formation of spherulites in polyamide melts: Part III. Even-even polyamides, *J. Polym. Sci. Part A-2 Polym. Phys.* 4 (1966) 243–265.

https://doi.org/10.1002/pol.1966.160040207.

[36] B.B. Burnett, W.F. McDevit, Kinetics of spherulite growth in high polymers, *J. Appl. Phys.* 28 (1957) 1101–1105. https://doi.org/10.1063/1.1722586.

[37] R. Brill, Ober das verhalten von polyamiden beim erhitzen, *J. Prakt. Chem.* 3275 (1942) 49–64.

[38] V.R. Brill, Beziehungen zwischen wasserstoffbindung und einigen eigenschaften von polyamiden, *Die Makromol. Chemie.* 18 (1956) 294–309. https://doi.org/10.1002/macp.1956.020180125.

[39] R. Androsch, M. Stolp, H.J. Radusch, Crystallization of amorphous polyamides from the glassy state, *Acta Polym.* 47 (1996) 99–104. https://doi.org/10.1002/actp.1996.010470206.

[40] M. Van Drongelen, T. Meijer-Vissers, D. Cavallo, G. Portale, G. Vanden Poel, R. Androsch, Microfocus wide-angle X-ray scattering of polymers crystallized in a fast scanning chip calorimeter, *Thermochim. Acta* 563 (2013) 33–37. https://doi.org/10.1016/j.tca.2013.04.007.

[41] P. Venkatraman, A.M. Gohn, A.M. Rhoades, E.J. Foster, Developing high performance PA 11/cellulose nanocomposites for industrial-scale melt processing, *Compos. Part B Eng.* 174 (2019). https://doi.org/10.1016/j.compositesb.2019.106988.

[42] A.M. Gohn, J. Seo, T. Ferris, P. Venkatraman, E.J. Foster, A.M. Rhoades, Quiescent and flow-induced crystallization in polyamide 12/cellulose nanocrystal composites, *Thermochim. Acta* 677 (2019). https://doi.org/10.1016/j.tca.2019.03.034.

[43] M. Pyda, E. Nowak-Pyda, J. Heeg, H. Huth, A.A. Minakov, M.L. Di Lorenzo, C. Schick, B. Wunderlich, Melting and crystallization of poly(butylene terephthalate) by temperature-modulated and superfast calorimetry, *J. Polym. Sci. B Polym. Phys.* 44 (2006) 1364–1377.

[44] R. Hsissou, R. Seghiri, Z. Benzekri, M. Hilali, M. Rafik, A. Elharfi, Polymer composite materials: A comprehensive review, *Compos. Struct.* 262 (2021) 113640. https://doi.org/10.1016/j.compstruct.2021.113640.

[45] A.K. Kulshreshtha, C. Vasile, Handbook of Polymer Blends and Composites, Rapra Technology Ltd., Exter, UK, 2002.

[46] G. Mittal, V. Dhand, K.Y. Rhee, S.J. Park, W.R. Lee, A review on carbon nanotubes and graphene as fillers in reinforced polymer nanocomposites, *J. Ind. Eng. Chem.* 21 (2015) 11–25. https://doi.org/10.1016/j.jiec.2014.03.022.

[47] K.S. Ibrahim, Carbon nanotubes-properties and applications: a review, *Carbon Lett.* 14 (2013) 131–144. https://doi.org/10.5714/cl.2013.14.3.131.

[48] J.E.K. Schawe, P. Pötschke, I. Alig, Nucleation efficiency of fillers in polymer crystallization studied by fast scanning calorimetry: Carbon nanotubes in polypropylene, *Polymer* 116 (2017) 160–172. https://doi.org/10.1016/j.polymer.2017.03.072.

[49] Y. Cai, J. Petermann, H. Wittich, Transcrystallization in fiber-reinforced isotactic polypropylene composites in a temperature gradient, *J. Appl. Polym. Sci.* 65 (1997) 67–75. https://doi.org/10.1002/(sici)1097-4628(19970705)65:1<67::aid-app9>3.3.co;2-6.

[50] N. Klein, G. Marom, Transcrystallinity in nylon 66 composites and its influence on thermal expansivity, *Composites* 25 (1994) 706–710. https://doi.org/10.1016/0010-4361(94)90205-4.

[51] Y. Wang, B. Tong, S. Hou, M. Li, C. Shen, Transcrystallization behavior at the poly(lactic acid)/sisal fibre biocomposite interface, *Compos. Part A Appl. Sci. Manuf.* 42 (2011) 66–74. https://doi.org/10.1016/j.compositesa.2010.10.006.

[52] R. Nowacki, B. Monasse, E. Piorkowska, A. Galeski, J.M. Haudin, Spherulite nucleation in isotactic polypropylene based nanocomposites with montmorillonite under shear, *Polymer* 45 (2004) 4877–4892. https://doi.org/10.1016/j.polymer.2004.04.058.

[53] D.W. Chae, B.C. Kim, Physical properties of isotactic poly(propylene)/silver nanocomposites: Dynamic crystallization behavior and resultant morphology, *Macromol. Mater. Eng.* 290 (2005) 1149–1156. https://doi.org/10.1002/mame.200500277.

[54] J.E.K. Schawe, P.A. Vermeulen, M. van Drongelen, A new crystallization process in polypropylene highly filled with calcium carbonate, *Colloid Polym. Sci.* 293 (2015) 1607–1614. https://doi.org/10.1007/s00396-015-3571-2.

[55] L. Li, B. Li, M.A. Hood, C.Y. Li, Carbon nanotube induced polymer crystallization: The formation of nanohybrid shish-kebabs, *Polymer* 50 (2009) 953–965. https://doi.org/10.1016/j.polymer.2008.12.031.

[56] R. Sengupta, A. Ganguly, S. Sabharwal, T.K. Chaki, A.K. Bhowmick, MWCNT reinforced polyamide-6,6 films: Preparation, characterization and properties, *J. Mater. Sci.* 42 (2007) 923–934. https://doi.org/10.1007/s10853-006-0011-1.

[57] S.-Y. Lin, E.-C. Chen, K.-Y. Liu, T.-M. Wu, Isothermal crystallization behavior of polyamide 6,6/multiwalled carbon nanotube nanocomposites, *Polym. Eng. Sci.* (2009) 2447–2453.

[58] L. Li, C.Y. Li, C. Ni, L. Rong, B. Hsiao, Structure and crystallization behavior of Nylon 66/multi-walled carbon nanotube nanocomposites at low carbon nanotube contents, *Polymer* 48 (2007) 3452–3460. https://doi.org/10.1016/j.polymer.2007.04.030.

[59] J. V. McLaren, A kinetic study of the isothermal spherulitic crystallization of polyhexamethylene adipamide, *Polymer* 4 (1963) 175–189. https://doi.org/10.1016/0032-3861(63)90024-7.

[60] J.H. Magill, Melting behaviour and spherulitic crystallization of polycaproamide (nylon 6), *Polymer* 3 (1962) 43–51. https://doi.org/10.1016/0032-3861(62)90065-4.

[61] E. Turska, S. Gogolewski, Study on crystallization of nylon 6 (polycapramide). III. Effect of "crystalline memory" on crystallization kinetics, *J. Appl. Polym. Sci.* 19 (1975) 637–644. https://doi.org/10.1002/app.1975.070190301.

[62] P. Sciences, P.P. Edition, J. Wiley, Cumulative "memory" effect in Nylon-6, *J. Polym. Sci. Polym. Phys. Ed.* 22 (1984) 311–313.

[63] H. Li, R. Guo, Y. Liu, S. Liu, E. Proniewicz, L.M. Proniewicz, Y. Zhao, Y. Xu, J. Wu, Self-nucleation-induced nonisothermal crystallization of nylon 6 from the melt, *J. Appl. Polym. Sci.* 132 (2015) 4–11. https://doi.org/10.1002/app.42413.

[64] K. Jariyavidyanont, A. Janke, R. Androsch, Crystal self-nucleation in polyamide 11, *Thermochim. Acta* 677 (2019) 139–143. https://doi.org/10.1016/j.tca.2019.02.006.

[65] R.H. Somani, L. Yang, B.S. Hsiao, Effects of high molecular weight species on shear-induced orientation and crystallization of isotactic polypropylene, *Polymer* 47 (2006) 5657–5668. https://doi.org/10.1016/j.polymer.2004.12.066.

[66] A. Nogales, B.S. Hsiao, R.H. Somani, S. Srinivas, A.H. Tsou, F.J. Balta-Calleja, T.A. Ezquerra, Shear-induced crystallization of isotactic polypropylene with different molecular weight distributions: In situ small- and wide-angle X-ray scattering studies, *Polymer* 42 (2001) 5247–5256. https://doi.org/10.1016/S0032-3861(00)00919-8.

[67] J.W. Housmans, R.J.A. Steenbakkers, P.C. Roozemond, G.W.M. Peters, H.E.H. Meijer, Saturation of pointlike nuclei and the transition to oriented structures in flow-induced crystallization of isotactic polypropylene, *Macromolecules* 42 (2009) 5728–5740.

https://doi.org/10.1021/ma802479c.

[68] S. Acierno, B. Palomba, H.H. Winter, N. Grizzuti, Effect of molecular weight on the flow-induced crystallization of isotactic poly(1-butene), *Rheol. Acta* 42 (2003) 243–250. https://doi.org/10.1007/s00397-002-0280-9.

[69] F.G. Hamad, R.H. Colby, S.T. Milner, Onset of flow-induced crystallization kinetics of highly isotactic polypropylene, *Macromolecules* 48 (2015) 3725–3738. https://doi.org/10.1021/acs.macromol.5b00386.

[70] J. Seo, A.M. Gohn, O. Dubin, H. Takahashi, H. Hasegawa, R. Sato, A.M. Rhoades, R.P. Schaake, R.H. Colby, Isothermal crystallization of poly(ether ether ketone) with different molecular weights over a wide temperature range, *Polym. Cryst.* 2 (2019). https://doi.org/10.1002/pcr2.10055.

[71] J. Seo, H. Takahashi, B. Nazari, A.M. Rhoades, R.P. Schaake, R.H. Colby, Isothermal flow-induced crystallization of polyamide 66 melts, *Macromolecules* 51 (2018) 4269–4279. https://doi.org/10.1021/acs.macromol.8b00082.

[72] L. Balzano, S. Rastogi, G.W.M. Peters, Crystallization and precursors during fast short-term shear, *Macromolecules* 42 (2009) 2088–2092. https://doi.org/10.1021/ma802169t.

[73] T. Yan, B. Zhao, Y. Cong, Y. Fang, S. Cheng, L. Li, G. Pan, Z. Wang, X. Li, F. Bian, Critical strain for shish-kebab formation, *Macromolecules* 43 (2010) 602–605. https://doi.org/10.1021/ma9020642.

[74] O.O. Mykhaylyk, P. Chambon, R.S. Graham, J.P.A. Fairclough, P.D. Olmsted, A.J. Ryan, The specific work of flow as a universal parameter to control the formation of Shish-Kebab morphology in polymers, *AIP Conf. Proc.* 1027 (2008) 496–498. https://doi.org/10.1063/1.2964741.

[75] H. Janeschitz-Kriegl, E. Ratajski, M. Stadlbauer, Flow as an effective promotor of nucleation in polymer melts: A quantitative evaluation, *Rheol. Acta* 42 (2003) 355–364. https://doi.org/10.1007/s00397-002-0247-x.

[76] B. Nazari, A.M. Rhoades, R.P. Schaake, R.H. Colby, Flow-induced crystallization of PEEK: Isothermal crystallization kinetics and lifetime of flow-induced precursors during isothermal annealing, *ACS Macro Lett.* (2016). https://doi.org/10.1021/acsmacrolett.6b00326.

[77] B. Zhang, J. Chen, X. Zhang, C. Shen, Formation of β-cylindrites under supercooled extrusion of isotactic polypropylene at low shear stress, *Polymer* 52 (2011) 2075–2084. https://doi.org/10.1016/j.polymer.2011.03.001.

[78] B. Zhang, J. Chen, F. Ji, X. Zhang, G. Zheng, C. Shen, Effects of melt structure on shear-induced β-cylindrites of isotactic polypropylene, *Polymer* 53 (2012) 1791–1800. https://doi.org/10.1016/j.polymer.2012.02.023.

[79] C. Zhang, H. Hu, X. Wang, Y. Yao, X. Dong, D. Wang, Z. Wang, C.C. Han, Formation of cylindrite structures in shear-induced crystallization of isotactic polypropylene at low shear rate, *Polymer* 48 (2007) 1105–1115. https://doi.org/10.1016/j.polymer.2006.12.025.

[80] K. Zhang, Z. Liu, B. Yang, W. Yang, Y. Lu, L. Wang, N. Sun, M. Yang, Cylindritic structures of high-density polyethylene molded by multi-melt multi-injection molding, *Polymer* 52 (2011) 3871–3878. https://doi.org/10.1016/j.polymer.2011.06.004.

[81] R.J. Gaylord, D.J. Lohse, Morphological changes during oriented polymer crystallization, *Polym. Eng. Sci.* 16 (1976) 163–167.

[82] J.W. Housmans, G.W.M. Peters, H.E.H. Meijer, Flow-induced crystallization of propylene/ethylene random copolymers, *J. Therm. Anal. Calorim.* 98 (2009) 693–705.

https://doi.org/10.1007/s10973-009-0532-3.

[83] O.O. Mykhaylyk, P. Chambon, C. Impradice, J.P.A. Fairclough, N.J. Terrill, A.J. Ryan, Control of structural morphology in shear-induced crystallization of polymers, *Macromolecules* 43 (2010) 2389–2405. https://doi.org/10.1021/ma902495z.

[84] E. Koscher, R. Fulchiron, Influence of shear on polypropylene crystallization: morphology development and kinetics, *Polymer* 43 (2002) 6931–6942.

[85] T.B. Van Erp, P.C. Roozemond, G.W.M. Peters, Flow-enhanced crystallization kinetics of iPP during cooling at elevated pressure: Characterization, validation, and development, *Macromol. Theory Simulations* 22 (2013) 309–318. https://doi.org/10.1002/mats.201300004.

[86] J.F. Vega, D.G. Hristova, G.W.M. Peters, Flow-induced crystallization regimes and rheology of isotactic polypropylene: Effects of molecular architecture, *J. Therm. Anal. Calorim.* 98 (2009) 655–666. https://doi.org/10.1007/s10973-009-0516-3.

[87] R. Pantani, I. Coccorullo, V. Volpe, G. Titomanlio, Shear-induced nucleation and growth in isotactic polypropylene, *Macromolecules* 43 (2010) 9030–9038. https://doi.org/10.1021/ma101775h.

[88] S. Coppola, L. Balzano, E. Gioffredi, P.L. Maffettone, N. Grizzuti, Effects of the degree of undercooling on flow induced crystallization in polymer melts, *Polymer* 45 (2004) 3249–3256. https://doi.org/10.1016/j.polymer.2004.03.049.

[89] J. Wang, J. Bai, Y. Zhang, H. Fang, Z. Wang, Shear-induced enhancements of crystallization kinetics and morphological transformation for long chain branched polylactides with different branching degrees, *Sci. Rep.* 6 (2016) 1–13. https://doi.org/10.1038/srep26560.

[90] N. Iqbal, K. Jariyavidyanont, A.M. Rhoades, R. Androsch, Critical specific work of flow for shear-induced formation of crystal nuclei in poly(L-lactic acid), *Polym. Cryst.* 2 (2019) 1–7. https://doi.org/10.1002/pcr2.10073.

[91] K. Jariyavidyanont, S. Mallardo, P. Cerruti, M.L. Di Lorenzo, R. Boldt, A.M. Rhoades, R. Androsch, Shear - induced crystallization of polyamide 11, *Rheol. Acta* (2021). https://doi.org/10.1007/s00397-021-01264-6.

[92] J. Seo, A.M. Gohn, R.P. Schaake, D. Parisi, A.M. Rhoades, R.H. Colby, Shear Flow-Induced Crystallization of Poly(ether ether ketone), *Macromolecules* 53 (2020) 3472–3481. https://doi.org/10.1021/acs.macromol.9b02611.

[93] G.S.Y. Yeh, K.Z. Hong, Strain-Induced Crystallization, *Part III: Theory, Polym. Eng. Sci.* 19 (1967) 395–400.

[94] Z. Wang, Z. Ma, L. Li, Flow-Induced Crystallization of Polymers: Molecular and Thermodynamic Considerations, *Macromolecules* 49 (2016) 1505–1517. https://doi.org/10.1021/acs.macromol.5b02688.

[95] F. De Santis, R. Pantani, G. Titomanlio, Effect of shear flow on spherulitic growth and nucleation rates of polypropylene, *Polymer* 90 (2016) 102–110. https://doi.org/10.1016/j.polymer.2016.02.059.

[96] V. Volpe, F. Foglia, R. Pantani, Effect of the application of low shear rates on the crystallization kinetics of PLA, *Polym. Cryst.* 3 (2020) e10139. https://doi.org/10.1002/pcr2.10139.

[97] F. Zuo, J.K. Keum, L. Yang, R.H. Somani, B.S. Hsiao, Thermal stability of shear-induced shish-kebab precursor structure from high molecular weight polyethylene chains, *Macromolecules* 39 (2006) 2209–2218. https://doi.org/10.1021/ma052340g.

[98] F.G. Hamad, R.H. Colby, S.T. Milner, Lifetime of flow-induced precursors in isotactic polypropylene, *Macromolecules* 48 (2015) 7286–7299. https://doi.org/10.1021/acs.macromol.5b01408.

[99] B. Nazari, A.M. Rhoades, R.P. Schaake, R.H. Colby, Flow-induced crystallization of PEEK: Isothermal crystallization kinetics and lifetime of flow-induced precursors during isothermal annealing, *ACS Macro Lett.* 5 (2016) 849–853. https://doi.org/10.1021/acsmacrolett.6b00326.

[100] W.P. Cox, E.H. Merz, Correlation of dynamic and steady flow viscosities, *J. Polym. Sci.* 28 (1958) 619–622.

[101] E. Ivanov, Rheology of maleinated iPP / MWCNT composites, *Proceedings of a 12th International Conference MTCM* (2009).

[102] A.M. Rhoades, A.M. Gohn, J. Seo, R. Androsch, R.H. Colby, Crystallization behavior of sheared polyamide 66, *AIP Conf. Proc*. (2018). https://doi.org/10.1063/1.5045956.

[103] M.R. Mackley, A. Keller, Flow induced crystallization of polyethylene melts, *Polymer* 4 (1973) 16–20. https://doi.org/10.1016/0032-3861(73)90073-6.

[104] Z. Wang, J. Ju, J. Yang, Z. Ma, D. Liu, K. Cui, H. Yang, J. Chang, N. Huang, L. Li, The non-equilibrium phase diagrams of flow-induced crystallization and melting of polyethylene, *Sci. Rep.* 6 (2016) 1–8. https://doi.org/10.1038/srep32968.

[105] S.J. Lee, W.G. Hahm, T. Kikutani, B.C. Kim, Effects of clay and POSS nanoparticles on the quiescent and shear-induced crystallization behavior of high molecular weight poly(ethylene terephthalate), *Polym. Eng. Sci.* 49 (2009) 317–323.

[106] N.V. Pogodina, V.P. Lavrenko, S. Srinivas, H.H. Winter, Rheology and structure of iPP near gel point: quiescent and shear-induced crystallization, *Polymer* 42 (2001) 9031–9043.

[107] R. Pantani, V. Speranza, G. Titomanlio, Effect of flow-induced crystallization on the distribution of spherulite dimensions along cross section of injection molded parts, *Eur. Polym. J.* 97 (2017) 220–229. https://doi.org/10.1016/j.eurpolymj.2017.10.012.

[108] S. Liparoti, V. Speranza, R. Pantani, G. Titomanlio, Process induced morphology development of isotactic polypropylene on the basis of molecular stretch and mechanical work evolutions, *Materials* 12 (2019) 505. https://doi.org/10.3390/ma12030505.

[109] E.M. Troisi, H.J.M. Caelers, G.W.M. Peters, Full characterization of multiphase, multimorphological kinetics in flow-induced crystallization of iPP at elevated pressure, *Macromolecules* 50 (2017) 3868–3882. https://doi.org/10.1021/acs.macromol.7b00595.

[110] F.G. Hamad, R.H. Colby, S.T. Milner, Transition in crystal morphology for flow-induced crystallization of isotactic polypropylene, *Macromolecules* 49 (2016) 5561–5575. https://doi.org/10.1021/acs.macromol.6b00303.

[111] R.H. Somani, B.S. Hsiao, A. Nogales, S. Srinivas, A.H. Tsou, I. Sics, F.J. Balta-Calleja, T.A. Ezquerra, Structure development during shear flow-induced crystallization of i-PP: in-situ small-angle X-ray scattering study, *Macromolecules* 33 (2000) 9385–9394. https://doi.org/10.1021/ma001124z.

[112] Z. Ma, L. Balzano, G. Portale, G.W.M. Peters, Flow induced crystallization in isotactic polypropylene during and after flow, *Polymer* 55 (2014) 6140–6151. https://doi.org/10.1016/j.polymer.2014.09.039.

[113] J.Z. Xu, C. Chen, Y. Wang, H. Tang, Z.M. Li, B.S. Hsiao, Graphene nanosheets and shear flow induced crystallization in isotactic polypropylene nanocomposites, *Macromolecules* 44 (2011) 2808–2818. https://doi.org/10.1021/ma1028104.

[114] Z. Ma, L. Balzano, T. Van Erp, G. Portale, G.W.M. Peters, Short-term flow induced

crystallization in isotactic polypropylene: How short is short?, *Macromolecules* 46 (2013) 9249–9258. https://doi.org/10.1021/ma401833k.

[115] V. Speranza, S. Liparoti, V. Volpe, G. Titomanlio, R. Pantani, Modelling of morphology development towards spherulites and shish–kebabs: Application to isothermal flow-induced crystallization experiments on isotactic polypropylene, *Polymer* 196 (2020) 122459. https://doi.org/10.1016/j.polymer.2020.122459.

[116] K.L. Kearns, J. Scherzer, M. Chyasnavichyus, D. Monaenkova, J. Moore, R.L. Sammler, T. Fielitz, D.A. Nicholson, M. Andreev, G.C. Rutledge, Measuring flow-induced crystallization kinetics of polyethylene after processing, *Macromolecules* (2021) 2101–2112. https://doi.org/10.1021/acs.macromol.0c02477.

[117] H. Tang, J. Bin Chen, Y. Wang, J.Z. Xu, B.S. Hsiao, G.J. Zhong, Z.M. Li, Shear flow and carbon nanotubes synergistically induced nonisothermal crystallization of poly(lactic acid) and its application in injection molding, *Biomacromolecules* 13 (2012) 3858–3867. https://doi.org/10.1021/bm3013617.

[118] M. Du, K. Jariyavidyanont, I. Kühnert, R. Boldt, R. Androsch, Effect of molar mass on critical specific work of flow for shear-induced crystal nucleation in poly(L-lactic acid), *Polymers* 13 (2021) 1266. https://doi.org/10.3390/polym13081266.

[119] R.C. Zhang, Y. Xu, A. Lu, K. Cheng, Y. Huang, Z.M. Li, Shear-induced crystallization of poly(phenylene sulfide), *Polymer* 49 (2008) 2604–2613. https://doi.org/10.1016/j.polymer.2008.03.041.

[120] L. Balzano, N. Kukalyekar, S. Rastogi, G.W.M. Peters, J.C. Chadwick, Crystallization and dissolution of flow-induced precursors, *Phys. Rev. Lett.* 100 (2008) 1–4. https://doi.org/10.1103/PhysRevLett.100.048302.

[121] K. Wang, F. Chen, Q. Zhang, Q. Fu, Shish-kebab of polyolefin by "melt manipulation" strategy in injection-molding: A convenience pathway from fundament to application, *Polymer* 49 (2008) 4745–4755. https://doi.org/10.1016/j.polymer.2008.08.020.

[122] G. Kumaraswamy, A.M. Issaian, J.A. Kornfield, Shear-enhanced crystallization in isotactic polypropylene. 1. Correspondence between in situ rheo-optics and ex situ structure determination, *Macromolecules* 32 (1999) 7537–7547. https://doi.org/10.1021/ma990772j.

[123] R. Pantani, L. Balzano, G.W.M. Peters, Flow-induced morphology of iPP solidified in a shear device, *Macromol. Mater. Eng.* 297 (2012) 60–67. https://doi.org/10.1002/mame.201100158.

[124] D. Drummer, A. Seefried, S. Meister, Characterization of material stiffness on injection moulded microspecimens using different test methods, *Adv. Mater. Sci. Eng.* (2014) 8 pages. https://doi.org/10.1155/2014/769206.

[125] D. Drummer, S. Meister, Correlation of processing, inner structure, and part properties of injection moulded thin-wall parts on example of polyamide 66, *Int. J. Polym. Sci.* (2014) 8 pages. https://doi.org/10.1155/2014/718926.

[126] P.J. Bates, C.Y. Wang, The Effect of Sample Preparation on the Mechanical Properties of Nylon 66, *Polym. Eng. Sci.* 43 (2003) 759–773. https://doi.org/10.1002/pen.10063.

[127] P. Venkatraman, A.M. Gohn, A.M. Rhoades, E.J. Foster, Developing high performance PA 11 / cellulose nanocomposites for industrial-scale melt processing, *Compos. Part B* 174 (2019) 106988. https://doi.org/10.1016/j.compositesb.2019.106988.

[128] Y. Spoerer, R. Androsch, D. Jehnichen, I. Kuehnert, Process induced skin-core morphology in injection molded polyamide 66, *Polymers* 12 (2020) 1–9.

https://doi.org/10.3390/POLYM12040894.

[129] S. Meister, D. Drummer, Influence of manufacturing conditions on measurement of mechanical material properties on thermoplastic micro tensile bars, *Polym. Test.* 32 (2013) 432–437. https://doi.org/10.1016/j.polymertesting.2012.12.006.

[130] T.A. Osswald, L.S. Turng, P. Gramann, Injection Molding Handbook, Hanser Gardner Publications, Inc., Cincinatti, OH, 2008.

[131] R.J. Crowson, A.J. Scott, D.W. Saunders, Rheology of short glass fiber-reinforced thermoplastics and its application to injection molding. III use of a high shear rate capillary rheometer in the injection molding shear rate range, *Polym Eng Sci.* 21 (1981) 748-754.

[132] A.M. Gohn, A.M. Rhoades, D. Okonski, R. Androsch, Effect of Melt-memory on the crystal polymorphism in molded isotactic polypropylene, *Macromol. Mater. Eng.* 303 (2018) 1800148. https://doi.org/10.1002/mame.201800148.

[133] K. Jariyavidyanont, J.L. Williams, A.M. Rhoades, I. Kühnert, W. Focke, R. Androsch, Crystallization of polyamide 11 during injection molding, *Polym. Eng. Sci.* 58 (2018) 1053–1061. https://doi.org/10.1002/pen.24665.

[134] A. Toda, R. Androsch, C. Schick, Insights into polymer crystallization and melting from fast scanning chip calorimetry, *Polymer* 91 (2016) 239–263. https://doi.org/10.1016/j.polymer.2016.03.038.

[135] A.M. Rhoades, N. Wonderling, A. Gohn, J. Williams, D. Mileva, M. Gahleitner, R. Androsch, Effect of cooling rate on crystal polymorphism in beta-nucleated isotactic polypropylene as revealed by a combined WAXS/FSC analysis, *Polymer* 90 (2016) 67-75. https://doi.org/10.1016/j.polymer.2016.02.047.

[136] A. Gohn, R. Androsch, A. Rhoades, Improving accuracy of mold filling simulation with experimental data, *Soc. Plast. Eng. Annu. Tech. Conf.*, Orlando, FL, 2018.

[137] J.M. Fischer, Handbook of Molded Part Shrinkage and Warpage, 2nd ed., Elsevier, Waltham, 2013.

[138] F. De Santis, R. Pantani, V. Speranza, G. Titomanlio, Analysis of shrinkage development of a semicrystalline polymer during injection molding, *Ind. Eng. Chem. Res.* 49 (2010) 2469–2476. https://doi.org/10.1021/ie901316p.

[139] R. Pantani, V. Speranza, G. Titomanlio, Relevance of crystallisation kinetics in the simulation of the injection molding process, *Int. Polym. Process* 16 (2001) 61–71. https://doi.org/10.3139/217.1620.

[140] R. Pantani, V. Speranza, G. Titomanlio, Effect of flow-induced crystallization on the distribution of spherulite dimensions along cross section of injection molded parts, *Eur. Polym. J.* 97 (2017) 220–229. https://doi.org/10.1016/j.eurpolymj.2017.10.012.

[141] DuPont, Zytel Molding Guide, (1995) 44. plastics.dupont.com/plastics/pdflit/americas/zytel/198118E.pdf%5Cn.

[142] S. Inoue, N. Ichikuni, T. Suzuki, T. Uematsu, K. Kaneko, Capillary condensation of N_2 on multiwall carbon nanotubes, *J. Phys. Chem. B* 102 (2002) 4689–4692. https://doi.org/10.1021/jp973319n.

[143] Wacker, https://www.wacker.com/h/en-us/silicone-fluids-emulsions/linear-silicone-fluids/wacker-ak-60000/p/000023055 (accessed July 7, 2021).

[144] T.G. Mezger, The Rheology Handbook, 5th ed., Hanover, 2020.

[145] A.M. Rhoades, A.M. Gohn, J. Seo, R. Androsch, R.H. Colby, Sensitivity of polymer crystallization to shear at low and high supercooling of the melt, *Macromolecules* 51

(2018). https://doi.org/10.1021/acs.macromol.8b00195.

[146] T.H. Mourey, T.G. Bryan, Size-exclusion chromatography in 1,1,1,3,3,3-hexafluoro-2-propanol, *J. Chromatogr. A* 964 (2002) 169–178. https://doi.org/10.1016/S0021-9673(02)00510-1.

[147] J.L. Lee, S.-G. Lee, K.-Y. Choi, J. Liu, Crystallization and melting behavior of Nylon 66/poly(ether imide) blends, *Polym. J.* 30 (1998) 531–537.

[148] R. Androsch, C. Schick, Crystal nucleation of polymers at high supercooling of the melt, in: F. Auriemma, G.C. Alfonso, C. de Rosa (Eds.), Polym. Cryst. I From Chain Microstruct. to Process., Springer International Publishing, Cham, 2017: pp. 257–288. https://doi.org/10.1007/12_2015_325.

[149] A.M. Gohn, A.M. Rhoades, N. Wonderling, T. Tighe, R. Androsch, The effect of supercooling of the melt on the semicrystalline morphology of PA 66, *Thermochim. Acta* 655 (2017) 313-318. https://doi.org/10.1016/j.tca.2017.07.012.

[150] J. Faraj, N. Boyard, B. Pignon, J.L. Bailleul, D. Delaunay, G. Orange, Crystallization kinetics of new low viscosity polyamides 66 for thermoplastic composites processing, *Thermochim. Acta* 624 (2016) 27–34. https://doi.org/10.1016/j.tca.2015.11.025.

[151] D. Mileva, R. Androsch, E. Zhuravlev, C. Schick, Morphology of mesophase and crystals of polyamide 6 prepared in a fast scanning chip calorimeter, *Polymer* 53 (2012) 3994–4001. https://doi.org/10.1016/j.polymer.2012.06.045.

[152] D. Mileva, I. Kolesov, R. Androsch, Morphology of cold-crystallized polyamide 6, *Colloid Polym. Sci.* 290 (2012) 971–978. https://doi.org/10.1007/s00396-012-2657-3.

[153] C. Schick, Insights into polymer crystallization and melting from fast scanning chip calorimetry, *Polymer* 91 (2016) 239-263. https://doi.org/10.1016/j.polymer.2016.03.038.

[154] R. Androsch, A.M. Rhoades, I. Stolte, C. Schick, Density of heterogeneous and homogeneous crystal nuclei in poly (butylene terephthalate), *Europ. Polym. J.* 66 (2015) 180–189. https://doi.org/10.1016/j.eurpolymj.2015.02.013.

[155] H. Haberkorn, K.H. Illers, P. Simak, Molekülordnung und kristallinität in polyhexamethylenadipamid, *Colloid Polym. Sci.* Kolloid-Zeitschrift Zeitschrift Für Polym. 257 (1979) 820–840. https://doi.org/10.1007/BF01383353.

[156] M. Hirami, SAXD studies on bulk crystallization of nylon 6.I. Changes in crystal structure, heat of fusion, and surface free energy of lamellar crystals with crystallization temperature, *J. Macromol. Sci. Part B* 23 (1984) 397–414. https://doi.org/10.1080/00222348408219468.

[157] A.M. Gohn, X. Zhang, A. McHale, R. Androsch, A.M. Rhoades, Competition between heterogeneous nucleation and flow-induced crystallization of polyamide 66 and its carbon nanotube composites, *Macromol. Rapid Commun.* (2022) 2200418. https://doi.org/10.1002/marc.202200418.

[158] Z.-B. Wang, Y.-M. Mao, X.-K. Li, Y.-G. Li, C. Jarumaneeroj, B. Thitisak, P. Tiyapiboonchaiya, W. Rungswang, B.S. Hsiao, The influence of ethyl branch on formation of shish-kebab crystals in bimodal polyethylene under shear at low temperature, *Chinese J. Polym. Sci.* 30 (2021) 1050–1058. https://doi.org/10.1007/s10118-021-2568-1.

[159] A. Romo-Uribe, A.H. Windle, "Log-rolling" alignment in main-chain thermotropic liquid crystalline polymer melts under shear: An in-situ WAXS study, *Macromolecules* 29 (1996) 6246–6255. https://doi.org/10.1021/ma960211h.

[160] B. Nazari, H. Tran, B. Beauregard, M. Flynn-Hepford, D. Harrell, S.T. Milner, R.H. Colby, Two Distinct Morphologies for Semicrystalline Isotactic Polypropylene

Crystallized after Shear Flow, *Macromolecule* 51 (2018) 4750–4761. https://doi.org/10.1021/acs.macromol.8b00563.

[161] W.J. Zhou, J.A. Kornfield, V.M. Ugaz, W.R. Burghardt, D.R. Link, N.A. Clark, Dynamics and shear orientation behavior of a main-chain thermotropic liquid crystalline polymer, *Macromolecules* 32 (1999) 5581–5593. https://doi.org/10.1021/ma990399f.

[162] J.P. Fernández-Blázquez, A. Bello, E. Pérez, Parallel and perpendicular orientation in a thermotropic main-chain liquid-crystalline polymer, *Macromolecules* 40 (2007) 703–709. https://doi.org/10.1021/ma062312d.

[163] R.H. Somani, L. Yang, L. Zhu, B.S. Hsiao, Flow-induced shish-kebab precursor structures in entangled polymer melts, *Polymer* 46 (2005) 8587–8623. https://doi.org/10.1016/j.polymer.2005.06.034.

[164] B.S. Hsiao, L. Yang, R.H. Somani, C.A. Avila-Orta, L. Zhu, Unexpected shish-kebab structure in a sheared polyethylene melt, *Phys. Rev. Lett.* 94 (2005) 1–4. https://doi.org/10.1103/PhysRevLett.94.117802.

[165] J.D. Hoffman, J.J. Weeks, Melting process and the equilibrium melting temperature of polychlorotrifluoroethylene, *J. Res. Natl. Bur. Stand. Sect. A Phys. Chem. 66 A* (1962) 13. https://doi.org/10.6028/jres.066a.003.

[166] P. Venkatraman, A.M. Gohn, A. Rhoades, J. Foster, Developing Polyamide/Cellulose Nanocomposites for Industrial-Scale Processing, in: *Int. Conf. Nanotechnol. Renew. Mater.* 2019, 2019.

[167] E. Zhuravlev, A. Wurm, P. Pötschke, R. Androsch, J.W.P. Schmelzer, C. Schick, Kinetics of nucleation and crystallization of poly(ε-caprolactone) - Multiwalled carbon nanotube composites, *Eur. Polym. J.* 52 (2014) 1–11. https://doi.org/10.1016/j.eurpolymj.2013.12.015.

[168] Y. Geng, M.Y. Liu, J. Li, X.M. Shi, J.K. Kim, Effects of surfactant treatment on mechanical and electrical properties of CNT/epoxy nanocomposites, *Compos. Part A Appl. Sci. Manuf.* 39 (2008) 1876–1883. https://doi.org/10.1016/j.compositesa.2008.09.009.

[169] A. Wurm, A. Herrmann, M. Cornelius, E. Zhuravlev, D. Pospiech, R. Nicula, C. Schick, Temperature Dependency of Nucleation Efficiency of Carbon Nanotubes in PET and PBT, *Macro. Mol. Mat. and Eng.* (2015) 637–649. https://doi.org/10.1002/mame.201400405.

[170] A.M. Gohn, J. Seo, R.H. Colby, R.P. Schaake, R. Androsch, A.M. Rhoades, Crystal nucleation in poly(ether ether ketone)/carbon nanotube nanocomposites at high and low supercooling of the melt, *Polymer* 199 (2020) 1–8. https://doi.org/10.1016/j.polymer.2020.122548.

[171] R.T. Zeng, W. Hu, M. Wang, S.D. Zhang, J.B. Zeng, Morphology, rheological and crystallization behavior in non-covalently functionalized carbon nanotube reinforced poly(butylene succinate) nanocomposites with low percolation threshold, *Polym. Test.* 50 (2016) 182–190. https://doi.org/10.1016/j.polymertesting.2016.01.003.

[172] B. Krause, R. Boldt, L. Häußler, P. Pötschke, Ultralow percolation threshold in polyamide 6.6/MWCNT composites, *Compos. Sci. Technol.* 114 (2015) 119–125. https://doi.org/10.1016/j.compscitech.2015.03.014.

[173] L. Qiu, Y. Chen, Y. Yang, L. Xu, X. Liu, A study of surface modifications of carbon nanotubes on the properties of polyamide 66/multiwalled carbon nanotube composites, *J. Nanomater.* (2013) 8 pages. https://doi.org/10.1155/2013/252417.

[174] P. Pötschke, T.D. Fornes, D.R. Paul, Rheological behavior of multiwalled carbon nanotube/polycarbonate composites, *Polymer* 43 (2002) 3247–3255. https://doi.org/10.1016/S0032-3861(02)00151-9.

[175] S. Huang, M. Wang, T. Liu, W.-D. Zhang, W.C. Tjiu, C. He, X. Lu, Morphology, thermal, and rheological behavior of nylon 11/multi-walled carbon nanotube nanocomposites prepared by melt compounding, *Polym. Eng. Sci.* 49 (2009) 1063–1068. https://doi.org/https://doi.org/10.1002/pen.21349.

[176] G. Mago, F.T. Fisher, D.M. Kalyon, Effects of multiwalled carbon nanotubes on the shear-induced crystallization behavior of poly(butylene terephthalate), *Macromolecules* 41 (2008) 8103–8113. https://doi.org/10.1021/ma8008838.

Declaration

I hereby solemnly declare that the submitted dissertation is entirely written and composed by myself. All the sources of information have been identified and referenced. This dissertation has not been previously submitted by me or any other for examination.

Baden, Pennsylvania, USA   2 November 2022   _____

City, Date   Signature

Curriculum Vitae

Personal information

Name   *Anne M. Gohn*

Birth   *03.10.1991 in Sewickley, PA, USA*

Academic profile

1996-2010   *Elementary and secondary education*

2010 – 2013   *B.S. Plastics Engineering Technology*

                     Penn State Erie – The Behrend College

2014 – 2016   *Masters in Manufacturing Management (MMM)*

                     Penn State Erie – The Behrend College

2016 – 2021   *Ph.D. at the Center of Engineering Sciences/Faculty of Natural Sciences II*

                     Martin Luther University Halle-Wittenberg, Germany

                     Title: Crystal nucleation efficacy of flow-induced formed nuclei and carbon nanotubes in the engineering polymer polyamide 66

There are no previous convictions and no preliminary investigation has been initiated.

<u>Baden, Pennsylvania, USA   2 November 2022</u>   _____

City, Date   Signature